



Kent Academic Repository

Burton, Andrew James (2022) *Analysis of Maser Properties Associated with High-Mass Star Formation*. Master of Research (MRes) thesis, University of Kent,.

Downloaded from

<https://kar.kent.ac.uk/95877/> The University of Kent's Academic Repository KAR

The version of record is available from

<https://doi.org/10.22024/UniKent/01.02.95877>

This document version

UNSPECIFIED

DOI for this version

Licence for this version

CC BY (Attribution)

Additional information

Versions of research works

Versions of Record

If this version is the version of record, it is the same as the published version available on the publisher's web site. Cite as the published version.

Author Accepted Manuscripts

If this document is identified as the Author Accepted Manuscript it is the version after peer review but before type setting, copy editing or publisher branding. Cite as Surname, Initial. (Year) 'Title of article'. To be published in *Title of Journal*, Volume and issue numbers [peer-reviewed accepted version]. Available at: DOI or URL (Accessed: date).

Enquiries

If you have questions about this document contact ResearchSupport@kent.ac.uk. Please include the URL of the record in KAR. If you believe that your, or a third party's rights have been compromised through this document please see our [Take Down policy](https://www.kent.ac.uk/guides/kar-the-kent-academic-repository#policies) (available from <https://www.kent.ac.uk/guides/kar-the-kent-academic-repository#policies>).

**Analysis of Maser Properties
Associated with High-Mass Star
Formation**

A thesis presented for the degree of
MSc by Research

School of Physical Sciences
University of Kent

By Andrew Burton

2022

Abstract

The main aim of this thesis was to see if more insight could be drawn from the maser properties than just their association statistics. We explore the properties and distributions of the 6.7 GHz methanol masers from the Methanol MultiBeam (MMB) survey and the 22.235 GHz water masers from the H₂O Southern Galactic Plane Survey (HOPS) within the massive and dense clumps detected by the APEX Telescope Large Area Survey of the Galaxy (ATLASGAL), and what this tells us about the physical properties of the star forming regions that generate them. We find that clumps containing both water and methanol masers are significantly more luminous, more evolved and more massive than clumps only containing one of these maser species. This leads us to the conclusion that combinations of other maser species may also represent different star forming stages. We compare our results to the current “straw man” model (Ellingsen et al., 2007) and after finding some differences, we suggest some modifications. We investigate the nature of masers that are offset far from the centre of the clump, and find that these are generally a result of large HII regions or unresolved sub-structures contained in the ATLASGAL clump. We have identified a sample of positionally and kinematically associated masers located on the edge of their clumps that have no clear infrared (IR) or submillimetre counterpart. Further work is required to identify the driving source of these masers. We also look at clumps that contain a significantly high quantity of water masers, and find that the majority of these clumps contain HII regions that are shocking these water masers. These clumps also show significantly higher luminosities, masses and luminosity-to-mass ratios than clumps with both maser species, which suggests that these are some of the most intense and evolved star forming regions in the ATLASGAL database. Our results are useful, since we have proven that the properties of masers can tell us about the nature of their star forming environments, which opens up possibilities for targeted searches by using maser properties. This will improve our understanding of massive star formation going forward.

Contents

1	Introduction	5
1.1	Molecular Clouds	7
1.1.1	Formation of Molecular Clouds	7
1.1.2	Mechanisms of Support Against Collapse	8
1.1.3	Molecular Clouds to Pre-Protostellar Core	10
1.2	Star Formation	11
1.2.1	Low-Mass Star Formation	11
1.2.2	High-Mass Star Formation	15
1.3	Masers	18
1.3.1	Introduction to Masers	18
1.3.2	Maser Associations with Astrophysical Phenomena	18
1.3.3	Useful Masers for this Study	20
1.3.4	Aims of the Thesis	22
2	Energy Transitions	23
2.1	Rotational Transitions & Metastable States	23
2.2	Collisional Pumping	25
2.3	Radiative Pumping	26
2.4	Methanol Maser Transitions	26
2.5	Water Maser Transitions	28
2.6	Statistics	29
2.6.1	p -value	29
2.6.2	Kolmogorov–Smirnov Tests	29

2.6.3	Spearman’s Correlation	30
2.7	Computer Programming Used For Data Analysis	32
3	In-Depth Breakdown of the Surveys	34
3.1	Continuum surveys	35
3.2	Multi-Wavelength Image Examples	36
3.3	Clump / Maser Surveys	40
3.4	Overlapping Regions	45
4	Water Masers and Evolution	49
4.1	Outline	49
4.2	Physical Properties of Clumps	51
4.3	Maser properties	55
4.4	Discussion of Clump and Maser Properties	59
4.5	Comparison of Results with “Straw Man” Model	64
4.6	Summary	66
5	Identifying Interesting Sources - Offsets	69
5.1	Angular offsets	70
5.2	Velocity Checks	73
5.3	Grouping Masers into Clumps	75
5.4	Classification and Discussion	76
5.4.1	Edge	78
5.4.2	Photodissociation regions	79
5.4.3	Localised clumps	80
5.4.4	Unknown association	82
5.5	Discussion	82
5.6	Summary	86
6	Identifying Interesting Sources - Water Maser Spots / Groups	88
6.1	Introduction	88
6.2	Data Reduction	89
6.2.1	Total number of spots	89

6.2.2	Spots Per Group	91
6.2.3	Velocity Checks	93
6.3	Multi-Wavelength Images	95
6.4	Discussion	98
6.5	Summary	99
7	Summary and Conclusions	101
A	Multi-Wavelength Images - Large Offset Sample	105
A.1	WMO Clumps - 4.6,5.8,8.0	105
A.2	WMO Clumps - 8.0,22,70	107
A.3	MMO Clumps - 4.6,5.8,8.0	108
A.4	MMO Clumps - 8.0,22,70	110
A.5	BM Clumps - 4.6,5.8,8.0	112
A.6	BM Clumps - 8.0,22,70	114
B	Multi-Wavelength Images - Many Water Masers Sample	116
B.1	Clumps - 8.0,22,70 μm	116

Chapter 1

Introduction

The evolutionary processes of young high-mass stars are not well understood, at least not when compared to their low-mass counterparts, and it is not a simple case of high-mass star formation representing a scaled up version of low-mass star formation ([Zinnecker and Yorke, 2007](#)). The nebulae in which they form are surrounded by dense matter, which traps visible light via dust and gas extinction, and obscures our view on the local environment. In addition, these high-mass star forming regions are often located farther from the Earth than low-mass star forming sites, they evolve through their early stages quickly and above all they are simply much rarer. Attaining a better grasp on the inner workings and environments of early massive star evolution will allow us to better understand the structure of the molecular clouds in which they form, their stellar feedback process that acts upon the local star forming environments and their profound role in shaping their host Galaxies ([Kennicutt, 2005](#)).

Fortunately, our observational techniques and instruments have vastly improved over the last half a century with developments in infra-red, radio and sub-millimetre technologies and surveys ([Churchwell et al., 2009](#); [Lumsden et al., 2013](#); [Condon et al., 1998](#); [Molinari et al., 2016](#)) that allow us to peer into the heart of the stellar nurseries like never before. At these wavelengths radiation is not trapped by the dense agglomeration of gas and dust in and around star forming regions (SFRs).

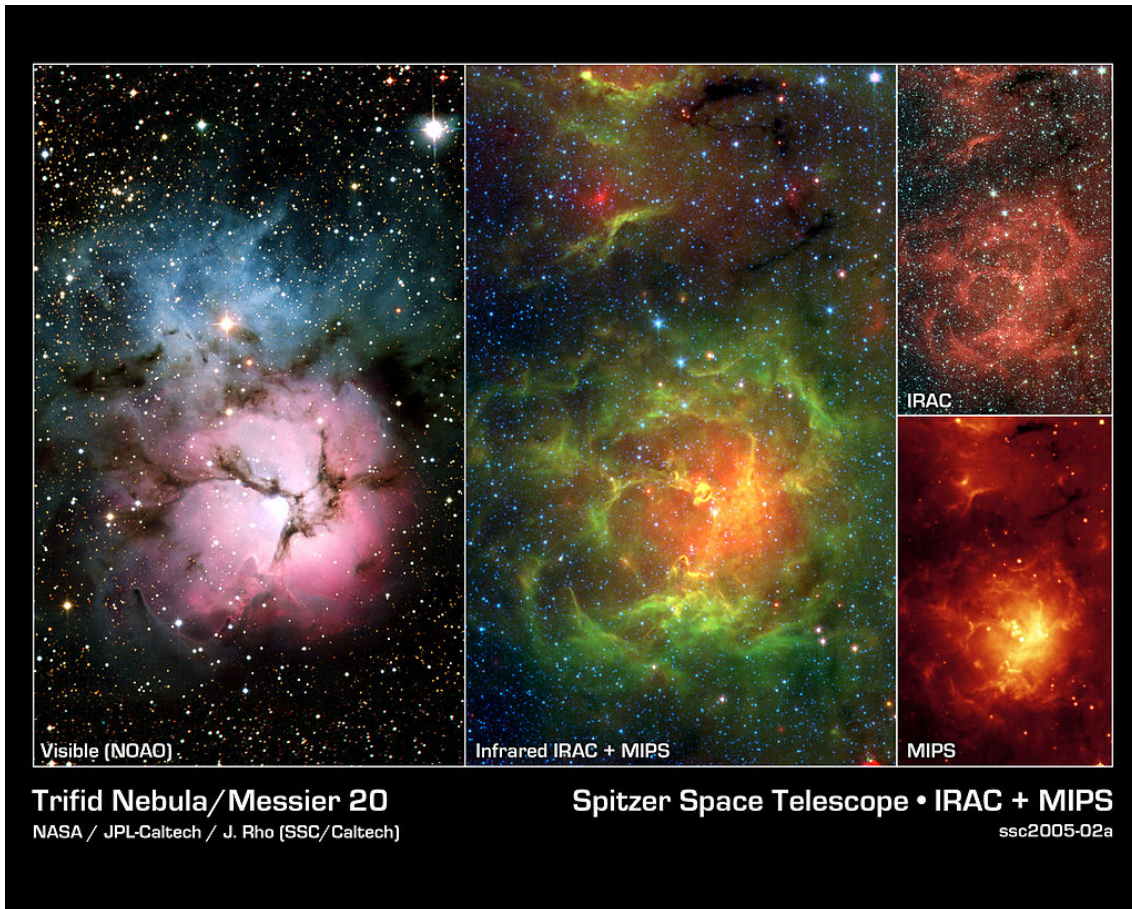


Figure 1.1: Comparison between a visible light image (left panel) of HII regions and infrared images of HII regions at 3.6 - 100 μm , 3.6 - 8 μm and 24 - 100 μm wavelengths for the middle, top-right and bottom-right panels respectively.

For example, HII regions are visible through these dense clouds since they also emit strongly in longer wavelengths. Figure 1.1 displays visible and infrared images of the same HII region, and the infrared can be seen to reveal much more detail about the structure of the HII region since it is not obscured by the thick cloud of gas and dust. HII regions are also tracers of high-mass stars, this is because HII regions are huge areas of interstellar hydrogen that have been ionised by these hot and massive young stars. Phenomena such as HII regions have given us a new way of shining light on the environments of these high-mass stars that were previously not visible at more traditional wavelengths.

1.1 Molecular Clouds

1.1.1 Formation of Molecular Clouds

Giant molecular clouds (GMCs) are the structures that forge stars in the cosmos. All stars are born within dense regions of these molecular clouds known as clumps/cloud cores, which makes them crucial in observing any star during its pre-stellar evolution. Along with low - intermediate mass stars they are also the hosts of massive young stellar objects (MYSOs), which are at the centre of discussions of high-mass star formation. For this reason, it is fundamental to examine how molecular clouds are formed and to give a general summary of the sequence of stages for early star formation.

Neutral hydrogen is ubiquitous within the Interstellar Medium (ISM) and it is a crucial element in the formation of any star, however most hydrogen within our Galaxy is diffuse and does not have the required density to produce the conditions under which a star may form. That being said, not all hydrogen is diffuse and given enough time, one theory is that gravity will slowly pull these denser regions into larger agglomerations forming huge molecular clouds. This theory is known as a “bottom up” formation mechanism, which is not particularly favoured due to insufficient raw material observed in these diffuse clouds ([Ostriker and Kim, 2004](#); [Heyer and Terebey, 1998](#)). The other, more favoured theory to molecular cloud formation follows a “top down” approach involving large-scale instabilities in the ISM governed by gravity, magnetic torque etc. ([Ostriker and Kim, 2004](#); [Ballesteros-Paredes et al., 2007](#)).

As well as hydrogen, approximately 1% of the mass of a GMC is composed of dust grains ([Alton et al., 1998](#); [Draine et al., 2007](#)). This is not a significant percentage, but these dust grains have a profound effect on the chemical makeup and structure of their respective clouds. They provide a collection site for hydrogen atoms to stick to and bond together to form molecular hydrogen (H_2). This halves the number of particles in the cloud, which will lead to a decrease in the pressure by a factor of 2, via $P = nkT$. The decrease in pressure also incurs a decrease in the volume

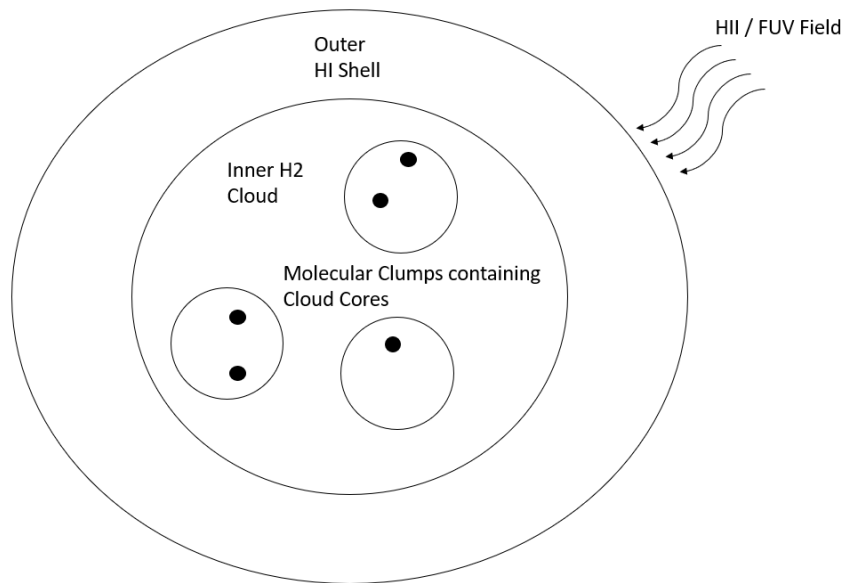


Figure 1.2: A sketch of the structure of a molecular cloud. This shows the protective HI shell, along with the clumps contained within the cloud and the cores contained within the clumps. The use of circles to indicate the different structures is not accurate, and is only used for illustrative purposes.

occupied by the particles, which enhances the density of particular regions within the molecular cloud. The clumps that are created from the accumulation of H_2 are the cornerstone of all star formation in the Universe and typically have masses ranging between $10\text{-}1000 M_\odot$ (Motte et al., 2007). Simultaneously, the molecular hydrogen shell that surrounds the molecular cloud is shielding the centralised H_2 from the far-ultraviolet (FUV) radiation cross-section that is ever-present in the ISM, which would otherwise dissociate the H_2 into atomic hydrogen. A diagram of the structure of a molecular cloud is illustrated in Figure 1.2. This perfect alignment of physical processes creates the ideal conditions for star forming sites.

1.1.2 Mechanisms of Support Against Collapse

Under normal conditions, these molecular clouds would inevitably collapse via their own self gravity and so must have an internal force acting globally throughout the cloud that supports them against collapse, whilst not being so strong as to stop dense cores from collapsing in to stars. This force is not thought to be from the thermal

pressure of the molecular gas, since the very low temperatures (~ 10 K) (Solomon et al., 1985) would not be enough to support against gravitational collapse. Instead it is thought to be largely down to turbulence and magnetic fields equally, which must support a pressure roughly 10 times that of the thermal pressure (Hennebelle and Falgarone, 2012). Both of these methods to support against collapse will now be briefly discussed.

Turbulence

Turbulence is a phenomenon thought to be driven by a combination of blast waves/-superbubbles from supernovae and magnetorotational instabilities within the ISM (Ballesteros-Paredes et al. 2007, and references therein). The outward pressure from turbulence is caused by supersonic shocks. These supersonic shocks are created by particles that are exceeding the speed of sound within their particular gas. The speed of sound in an ideal gas can be derived by equating the kinetic energy of that gas to its thermal energy:

$$\frac{3}{2}KT = \frac{1}{2}mv^2 \quad (1.1)$$

Where K is Boltzmann's constant ($1.38 \times 10^{-23} \text{ m}^2 \text{ kg s}^{-2} \text{ K}^{-1}$), T is the temperature of the gas, m is the mass of the gas and v is the sound speed. Typical sound speeds for molecular gas with a temperature of 10 K are $\sim 0.2 \text{ km s}^{-1}$, however, observed velocity dispersions in GMCs are much higher than this. In Stark (1984), the one-dimensional rms velocity dispersions of low-mass molecular clouds ($10^2 M_\odot \leq M_{\text{cloud}} \leq 10^4 M_\odot$) in the local neighbourhood ($r \leq 3 \text{ kpc}$) were estimated to be $\sim 9.0 \text{ km s}^{-1}$ and for moderate-mass molecular clouds ($10^4 M_\odot \leq M_{\text{cloud}} \leq 10^{5.5} M_\odot$) it was $\sim 6.6 \text{ km s}^{-1}$. Both of these are of course much greater than the sound speed of typical molecular gas and so will often create supersonic shocks, providing the outward pressure to combat gravitational collapse.

Turbulence not only combats gravitational collapse of the cloud but it also results in the clumping of dense regions from shocks, which creates the inhomogeneity of density of material needed for star-forming sites (McKee and Ostriker, 2007).

Turbulence is therefore crucial for the structure and longevity of GMCs on small and large scales.

Magnetic Fields

Magnetic fields can support against gravitational collapse, but only in the perpendicular direction, since the magnetic force only acts perpendicular to the field lines. This causes the clouds to collapse into discs, since there is no impediment of movement parallel to the field lines. Neutral particles can still collapse in the perpendicular direction, but they have to percolate between tightly compacted ions at a slow rate. The process by which collapse in the perpendicular direction occurs is called “ambipolar diffusion” (Mestel and Spitzer, 1956).

1.1.3 Molecular Clouds to Pre-Protostellar Core

The clumps hiding within molecular clouds are very cold and dense regions of gas and dust. It is important for the temperature to be cool (around 10-20 K) so that the atoms bind together creating molecular gas. It has already been mentioned that H_2 is a common feature within these dense regions but CO is also present, which is well known to be an excellent tracer of molecular gas (Dame et al., 1987) hence star forming regions. The reason for using CO is that it is the second most abundant molecule in the ISM and unlike H_2 , has a permanent dipole that allows first order electric dipole transitions, hence CO can be used to track cold regions whereas molecular hydrogen cannot. The cold temperatures also affect the density, since a lower temperature will result in a lower volume, by virtue of the equation $PV = kT$, therefore causing the cloud core to contract and increase densities. At lower temperatures, we also observe the formation of more complex molecules, since particles at cooler temperatures travel at lower velocities and so are more likely to stick to dust grains, which produces more complex molecules. The increased density of the cloud core will cause it to collapse faster than the outer cloud into many individual cloud fragments, these have radii ranging from 0.03 to 0.4 pc (Hocuk, S. and Spaans, M., 2010). The mass accumulation of matter into these small volumes will continue to contract and slowly convert gravitational potential energy into ther-

mal energy. The thermal energy will rise along with the temperature of the core given that there is efficient cooling (high CO optical depth), eventually forming an individual pre-protostellar object at its centre.

The critical point at which a clump will contract depends on its radius and its mass, which are defined as the Jeans length (R_J) and the Jeans mass (M_J). These can be represented mathematically as shown below:

$$R_J = \left(\frac{15k_B T}{G\mu m_H \rho} \right)^{\frac{1}{2}} \quad (1.2)$$

$$M_J = \left(\frac{5k_B T}{G\mu m_H} \right)^{\frac{3}{2}} \left(\frac{3}{4\pi\rho} \right)^{\frac{1}{2}} \quad (1.3)$$

where k_B is Boltzmann's constant ($1.38 \times 10^{-23} \text{ m}^2 \text{ kg s}^{-2} \text{ K}^{-1}$), T is the temperature, G is the universal gravitational constant ($\approx 6.67 \times 10^{-11} \text{ m}^3 \text{ kg}^{-1} \text{ s}^{-2}$), μ is the mean molecular weight, m_H is the atomic mass of hydrogen and ρ is the mean density of the gas. If $R_{\text{Clump}} > R_J$ or $M_{\text{Clump}} > M_J$ then the internal pressure will not be strong enough to withstand the force of the cloud's own gravity, and it will collapse into a protostar.

1.2 Star Formation

The next few sections will explain the formation process of low-mass and high-mass star formation in further detail, elaborating on how exactly these cloud fragments contract to form protostellar objects, as well as exploring some of the fundamental mechanisms involved in star formation.

1.2.1 Low-Mass Star Formation

Once the cloud fragments have contracted and heated, the pre-protostellar core of the cloud fragment begins to speed up its rotation as the core collapses due to gravity. At this point, the core is still surrounded by an enveloping cloud of gas and dust that also rotates, albeit at a slower rate. The surrounding material will continue to fall onto the central core, where accretion shocks will convert most of the kinetic energy of the material into thermal energy, producing huge luminosities.

As the core continues to heat up, the molecular gas within will eventually dissociate into atomic hydrogen at ~ 2000 K (Omukai and Nishi, 1998), which gives rise to a second collapse of the pre-protostellar core. As the core contracts it begins to accrete material on to its surface, which increases its angular momentum. This then causes the infall of material to orbit around the core in an accretion disk. This accretion disk is formed mostly from gas and partially from larger debris that follows an orbital motion around the young star and it is crucial for the accretion of mass in evolving stars. Because angular momentum must be conserved, the protostar transports this angular momentum away from itself. This is done via stellar winds that are ejected in strong collimated jets entraining the molecular gas at either end of the rotation axes of the protostar where large volumes of material are transported away at speeds in the range of 20 - 200 km/s. (Fujishiro et al., 2020; Meaburn et al., 2009), the material entrained by these jets are known as bipolar outflows. An example of a young protostar exhibiting bipolar outflows can be seen in Figure 1.3.

The core continues to slowly contract, where the star is now classed as a T-Tauri Star (Joy, 1945). These stars are powered by their gravitational energy as they contract. The T-Tauri Star continues to accrete matter until the core reaches temperatures of $\sim 10^6$ K, where nuclear fusion reactions begin. These nuclear reactions bring about radiative pressure that balances the gravitational pull of the core, which consequently puts the star in a state of hydrostatic equilibrium. The radiation emitted from nuclear reactions within the core will blow away its embryonic material so that no more material can fall onto the surface. This brings an end to the stellar evolution of a low-mass star where it will soon transition onto the main sequence stage and live out the rest of its life.



Figure 1.3: An infrared image of a bipolar outflow driven by an massive young star named DR 21. Image credit : Chris Davis, UKIRT/Joint Astronomy Centre.

Spectral Classes of Protostars

The different stages of star formation are classified using spectral classes as done by [Lada \(1987\)](#). In this paper, Lada constructed energy distributions from infra-red photometry observations in the 1-20 μm range. The excess infrared emission seen in [Figure 1.4](#) corresponds to the radiation from the circumstellar disk around the embedded object, the more radiation observed, the earlier the object was thought to be. Depending on the shape of these energy distributions Lada was able to classify protostellar objects into 3 classes; Class I, Class II and Class III protostars. Additionally, [Andre et al. \(1993\)](#) proposed an earlier class of protostar that they coined “Class 0”. It is important to briefly touch on the stage of a stars evolution that each spectral class refers to, the energy distribution shape for each class can be viewed in [Figure 1.4](#).

Class 0: These are the earliest examples of YSOs ($\leq 10^4$ yr) that are still deeply embedded within their shroud of embryonic material, it is thought that at least half of the star’s mass is still contained within its envelope of gas and dust. They are characterised by a strong, centralised sub-millimetre emission and even at such an early stage show signs of energetic bipolar outflows, suggesting their key importance

in the star forming process.

Class I: More evolved than the Class 0 protostar ($\sim 10^5$ yr), these stars have accreted most of their mass from their circumstellar envelope. They are however, still surrounded by this envelope that will emit excess infra-red radiation via internal heating from the core, primarily in the mid-infrared range.

Class II & Class III: The most evolved stages of a young stellar object ($\sim 10^6$ yr), these classes correspond roughly to classical T-Tauri stars (Class II) and weak-lined T-Tauri stars (Class III), since the majority of their envelopes have either accreted onto the star or been blown away by radiative pressure from bipolar outflows. Classical and weak lined T-Tauri stars correspond to the star's circumstellar disk being optically thick and optically thin respectively.

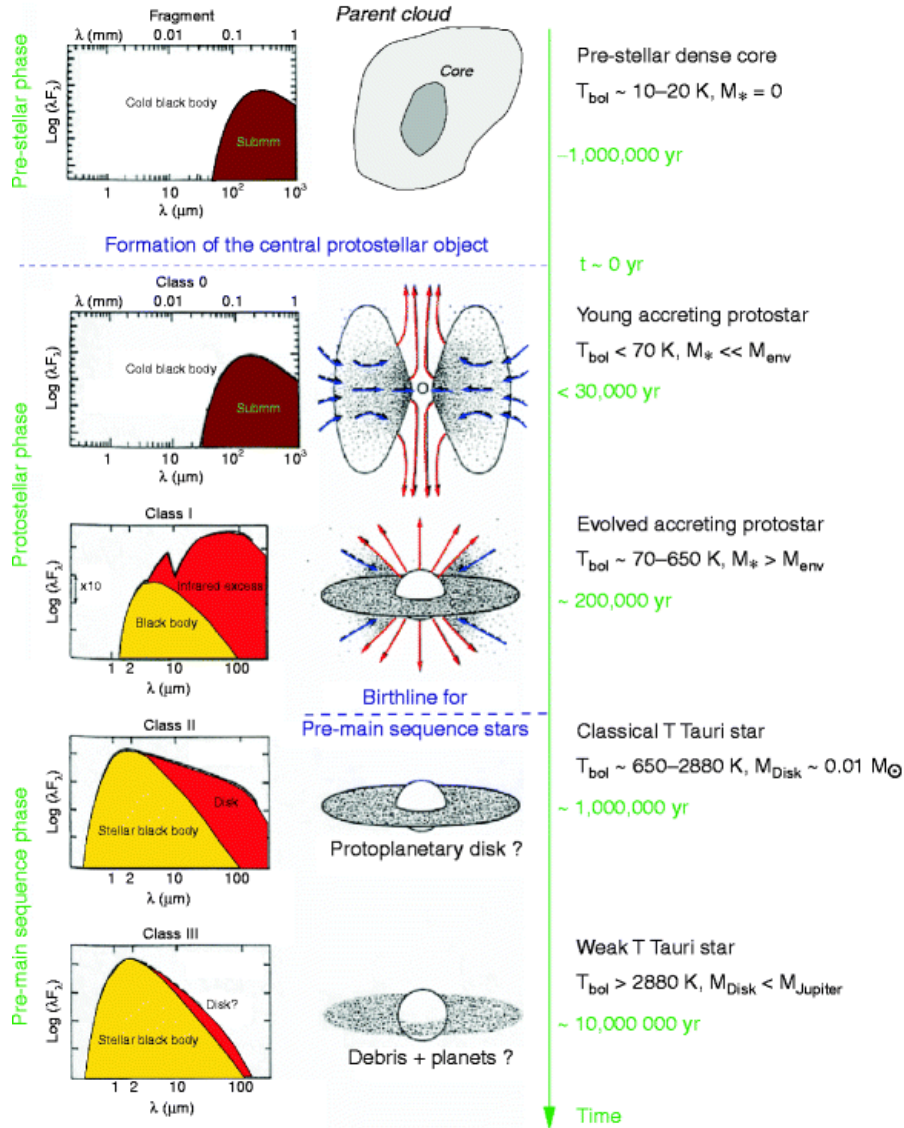


Figure 1.4: The evolution of the different classes of young protostellar objects, which shows their respective spectral energy distributions and an illustration of their structure / disk evolution. The top image shows a pre-stellar core, while the subsequent 4 images represent Classes 0, I, II and III, respectively. Image from [André \(2011\)](#).

1.2.2 High-Mass Star Formation

In comparison to low-intermediate mass star formation, the early stages of high-mass star formation are relatively poorly understood. This is because they are located at greater distances, they evolve more quickly through their early stages and so

are more rare than their low-mass counterparts, and they often form in very dense conditions with thick layers of gas and dust orbiting them, making them optically invisible (Zinnecker and Yorke, 2007).

The last point is compounded by the fact that they are still surrounded by their natal clouds even when they reach the main sequence due to their short Kelvin Helmholtz timescale. The K-H timescale defines the length of time it takes a protostar to radiate away its gravitational energy at its current luminosity. This is shown in equation 1.4:

$$t_{\text{KH}} = \frac{GM^2}{RL} \quad (1.4)$$

where G is the universal gravitational constant ($\approx 6.67 \times 10^{-11} \text{ m}^3 \text{ kg}^{-1} \text{ s}^{-2}$), M is the mass of the star, R is the radius of the star and L is the star's luminosity. At the end of the K-H timescale for a particular protostar, it will have to burn from a new source of energy in order to carry on to the main sequence, which we know to be the fusion of hydrogen into helium. Therefore, it can be said that the K-H timescale approximately calculates the time for a protostar to contract to the main-sequence stage as a result of the definition. The K-H timescale is much shorter for high-mass stars than for low-mass stars because they possess much larger luminosities and so radiate away energy at a quicker rate. As a result, high-mass stars will always reach the main sequence whilst surrounded by a thick envelope of gas and dust. This makes it extremely difficult to determine how high-mass stars are able to accumulate so much mass.

Most high-mass stars are between 10-40 M_{\odot} , however the Eddington luminosity calculates that purely by spherical accretion, the most mass a star could ever accumulate is limited to $\sim 7 M_{\odot}$ because past a certain luminosity the stars radiation pressure will be so great that the infalling material will simply be blown away from the celestial body rather than be pulled inwards by gravity. For this reason, most high-mass stars between 10-40 M_{\odot} are thought to be formed through an accretion disk, so that the internal energy can escape through bipolar outflows without radia-

tive pressure impeding infall rates. The bipolar outflows that occur in high-mass star formation are thought to be “scaled up” versions of their low-mass counterparts (Beuther et al., 2002).

Another possibility to explain the formation of high-mass stars is the process of competitive accretion. Competitive accretion occurs when stars in a cluster accrete from a shared reservoir of gas (Bonnell, 2005). It is known that the majority of stars form within a cluster (Lada and Lada, 2003) and so this process is thought to be a common occurrence within clumps. The infalling gas will rush towards the centre of the cluster and so stars located around this region will accrete more mass than others. The location of the star and the mass of the star are key parameters that determine the quantity of gas that they accrete. As well as high-mass stars, competitive accretion could also explain the origin of the initial mass function (IMF) (Bonnell, 2005), since a distribution of masses would be observed if the gas is not evenly spread throughout the cluster.

Core accretion is a model in which massive cores are assumed to be scaled up versions from the cores that are known to be formed in the low-mass counterparts, and it is also assumed that these are gravitationally bound (Tan et al., 2014). These cores condense with a range of masses from the surrounding fragmenting clump environment and then transition into collapse via a central disk to form a single massive star. However one of the main problems with this theory is that the cloud could fragment into a small star cluster with lower individual masses, preventing the birth of massive stars.

The idea of coalescence between low-intermediate mass stars merging into a single, higher mass entity has also been discussed by Bonnell et al. (1998). They claim that this method of high-mass star formation is completely viable in the centre of dense regions of large stellar clusters where the stellar density $\geq 10^4$ stars pc^{-3} . In their paper it was estimated that stars $\sim 50 M_{\odot}$ could be explained by coalescence, at which point “the collisions are most probably halted by the ejection of the gas contained in the core”.

Unfortunately coalescence nor accretion disks can explain the formation of the most

massive stars that have $100 M_{\odot}$ or greater since simulations of these environments become very unstable past these masses, and so even despite significant progress in recent years there still remains a mystery over the topic of high-mass star formation.

1.3 Masers

1.3.1 Introduction to Masers

A workaround to view into the heart of these stellar nurseries is to use astrophysical masers. Masers are similar to lasers, in the sense that they are a source of stimulated emission that focuses photons to travel in the same direction at a particular frequency. Masers describe a type of laser that emits these photons in the microwave frequency range.

Masers are excellent tracers of SFRs and particular environmental features, such as HII regions. For this reason, they can help us understand much about the composition of the clump and what astrophysical processes might be driving star forming activity.

Natural astrophysical masers in space are only possible to produce when there are a multitude of factors in the environment combining together to provide pumping mechanisms, population inversions for stimulated emission, gain mediums to amplify the signal that makes them detectable and a high column density of material. This is discussed in detail in Chapter 2.

1.3.2 Maser Associations with Astrophysical Phenomena

The first naturally occurring astrophysical masers were discovered by [Weaver et al. \(1965\)](#) when they observed strong 1665 MHz emission lines coming from an unknown source, which we now know to be a type of OH maser. Masers have led to many spectacular findings, one such example includes a distance calculation to the Galaxy NGC4258 via maser orbits in the central black hole disk ([Herrnstein et al., 1999](#)), which is an example of a maser parallax measurement. However their main and most advantageous property is that they act as excellent signposts for particular

types of astrophysical phenomena or astronomical bodies such as comets (Colom et al., 2002), planetary atmospheres (Gray, 1999), supernova remnants (Wardle and McDonnell, 2012) and high-mass star forming regions (Walsh et al., 2014; Breen et al., 2013). Various maser species and their associations can be seen in Table 1.1.

Table 1.1: A few examples of some maser species and what they are commonly associated with.

Maser Species	Astrophysical Association
Water 22.235 GHz	Evolved stars, Massive YSO's
Methanol 6.7 GHz Class II	Exclusively Massive YSO's
Formaldehyde 6cm	Massive YSO's
Hydroxyl	Evolved stars, YSO's
Silicon Monoxide	Evolved stars, YSO's

Natural masers require a very particular set of conditions that are only caused by certain natural phenomena, which makes them excellent tracers for specific conditions.

Masers are usually differentiated by their species (the type of molecule) and their frequency, however in the case of methanol masers, they are also separated into “class I” and “class II” classifications. The difference in classification boils down to how they are pumped, it is known that class I methanol masers are collisionally pumped (Cragg et al., 1992) whereas class II are radiatively pumped (Cragg et al., 2005; Fontani et al., 2010; Sobolev et al., 2007). These different pumping mechanisms have a significant impact on where we detect the two classes of masers. For example, we expect to find class I methanol masers on the boundaries of ambient regions that are being shock excited by an external source such as outflows and jets, this means they are often associated with star formation (SF) and occasionally massive star formation (MSF). In contrast, class II methanol masers are commonly associated with MSF, hot molecular cores, ultracompact (UC) HII regions, OH masers and near-IR sources (Fontani et al., 2010).

Masers are also excellent signposts for indicating the evolution of a SFR, which led [Ellingsen et al. \(2007\)](#) to create the “straw man” model (see [Figure 1.5](#)). This shows the various evolutionary stages at which masers are observable, along with some indication of the lifetime of these masers.

The types of maser and where they are found in relation to the SFR are critical to learn about these early stages of high-mass stars. For example, H_2O masers found at the edges of a clump suggests that these masers are being shock pumped by an external environment (supernovae, cloud collision etc.) that could have a significant impact on the local environment of high-mass YSOs.

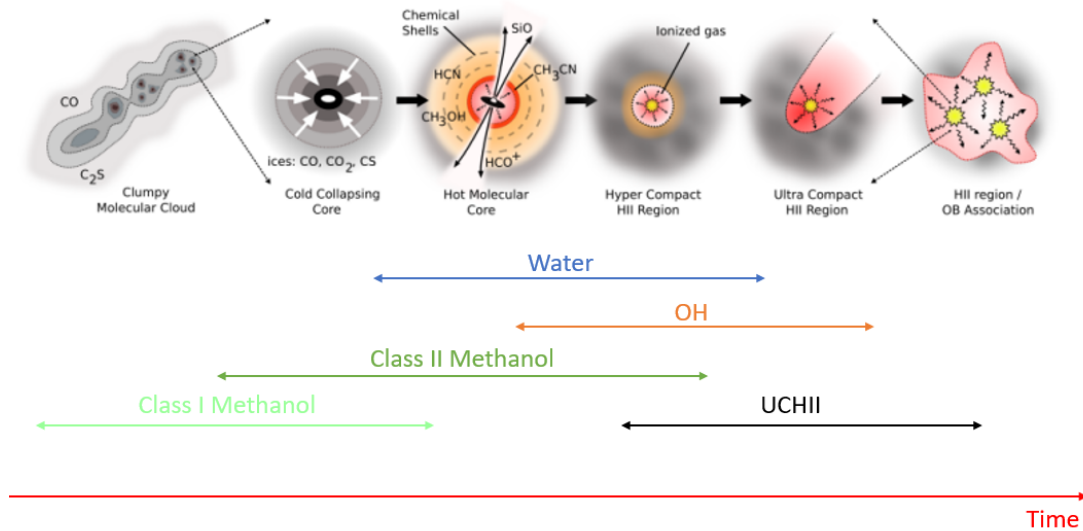


Figure 1.5: A brief outline of the evolutionary sequence of high-mass stars, along with the “straw man” model ([Ellingsen et al., 2007](#)) that shows the lifetimes of various maser species. Image Credit : Cormac Purcell

1.3.3 Useful Masers for this Study

We are going to focus on recent surveys of 22.235 GHz H_2O masers and Class II 6.7 GHz methanol masers in order to investigate MSF regions. These types of masers were focused on since they are the most commonly associated with high-mass star formation sites. The specific associations and purposes of these two maser transitions will now be explained in the following paragraphs.

Class II 6.7 GHz methanol masers are known to be exclusively associated with high-mass star forming regions (Breen et al., 2013) and are thought to be a precursor to HII regions, which trace the early stages of high-mass star formation. It is therefore true to say that this species of maser is exclusively associated with high-mass star formation. The importance of this association is immediately obvious, since it allows for identification of molecular clumps that contain MSF and where these MSF regions are located within molecular clumps. As well as this important link to MSF, they are also the most widespread and brightest transition of all the Class II methanol masers we know of, which makes them excellent tracers for the purposes of this thesis.

In Walsh et al. (2014), the 22.235 GHz H₂O masers that were detected via single-dish observations in the HOPS survey (Walsh et al., 2011) were found to be associated primarily with star formation (69%) but also with evolved stars (19%). They are detected in the shock regions from the bipolar outflows of high-mass stars (Titmarsh et al., 2014) where molecular outflows meet the ambient material enveloping the star, but they can also be detected in the circumstellar disk of the star (Billington et al., 2020). They are also not exclusive to just high-mass stars, as they are often found in the proximity of low-mass stars (Claussen et al., 1996). Additionally, they are also brighter than any other maser species and so could detect star forming sites which may otherwise be missed. Finally, these masers are widespread as opposed to rarer maser species linked with embedded star formation, which may only happen in incredibly brief phases of early star formation. An example of this is formaldehyde (H₂CO), which is a very rare maser species that is thought to arise from shocked gas (Hoffman et al., 2007).

We find both of these H₂O and methanol masers to be associated with high-mass star forming regions, since high-mass star forming sites have an abundance of readily available methanol and water molecules from chemical reactions on icy dust grains (Menten, 1997). They are also able to provide a pumping mechanism for atoms to be raised to a higher energy state, which induces the population inversion required to generate masers.

1.3.4 Aims of the Thesis

The objectives of this thesis look to investigate the association of masers with molecular clumps. This has been done before by [Billington et al. \(2020\)](#), but in this thesis we look at how the distribution of various maser species will trace star forming clumps with particular physical properties. The distribution of masers are also used to investigate external environments of the clump that may be driving massive star forming regions (MSFRs) toward the centre.

A brief description for each of the following chapters of this thesis are outlined below:

In Chapter 2, we look at different energy transitions and pumping mechanism of masers, how they are produced and what physical phenomena they are associated with. We also discuss the various statistical tools used throughout this thesis.

In Chapter 3, we discuss and analyse the surveys that will be used for the production of multi-wavelength images, as well as the surveys containing the physical and maser properties of the sources. These surveys include ATLASGAL, MMB, HOPS, GLIMPSE, Hi-Gal and WISE.

In Chapter 4 we look at the how different maser species may also act as signposts for the evolution of a clump. We look at clumps with water and methanol maser emission to compare the evolutionary stage, luminosity, mass, quantity of masers and the offsets of masers with clumps only showing signs of one type of maser emission.

In Chapter 5 we identify sources from ATLASGAL that have either water or methanol masers at large offsets from the centre of their clump in order to detect external environments affecting the central SFRs. This is done by presenting three-colour images in infra-red wavelengths.

In Chapter 6, we identify sources from ATLASGAL that have an unusually high quantity of water masers. This will help identify clumps that are more evolved and have powerful centres. We will again present three-colour images of these clumps and identify common themes that persist to develop an understanding of what physical phenomena are needed to produce these powerful SFRs.

Chapter 2

Energy Transitions

This chapter focuses on some important theory that will help build a foundation for understanding for the research chapters that will follow. We look to discuss rotational transitions, which is how masers emit their frequencies and become observable to us. We will then draw attention to the processes of collisional and radiative pumping, their differences and what astrophysical phenomena they are likely to be associated with. After this, we will then review some of the statistical tools that will be used extensively in Chapters 4-6.

2.1 Rotational Transitions & Metastable States

Astrophysical masers emit radiation from rotational transitions. This means that the molecules will increase or decrease by discrete, angular momentum values that will release the microwave radiation that we observe. We previously discussed that masers require a population inversion i.e more of the electrons must be in a higher energy rotational state than the number of electrons in the ground rotational state. The electrons in these molecules must also undergo stimulated emission, which is where an incident photon will interact with an electron in a higher energy state, causing it to drop to the ground state and a photon of the same energy as the incident photon. In order for this to occur, a molecule must have an intermediate, metastable state.

Metastable states are excited states of an atom that have a longer lifetime than ordinary excited states (about 10^{-3} s compared to 10^{-8} s). The electrons in this state have a different spin to those in the ground state and so in order to drop down to the ground state, the angular momentum must also be conserved. Since a photon with the correct angular momentum has to be absorbed by the electron for it to have the same spin as the ground state and hence transition to the ground state, the electron will spend longer in this metastable state than other excited states.

The existence of a metastable state is absolutely crucial for masing, since its longer lifetimes allow electrons to stay in the metastable state for a longer period of time before de-exciting to the ground state. In normal excited states, the electrons would almost immediately de-excite, which would not allow for a population inversion for a maser to form. The metastable states hold these electrons for longer and therefore provides the population inversion and stimulated emission needed for these masers to produce strong, coherent beams.

Metastable states are not present in all molecules, therefore we do not observe maser emission for all molecules in space. The observed frequency from a maser species is determined by the energy difference between the rotational metastable state and the rotational ground state because this is the transition that electrons undergo during stimulated emission. It is not uncommon for molecules to have multiple metastable states, which is why we also observe many different frequencies of a single molecule maser. Figure 2.1 shows this phenomenon.

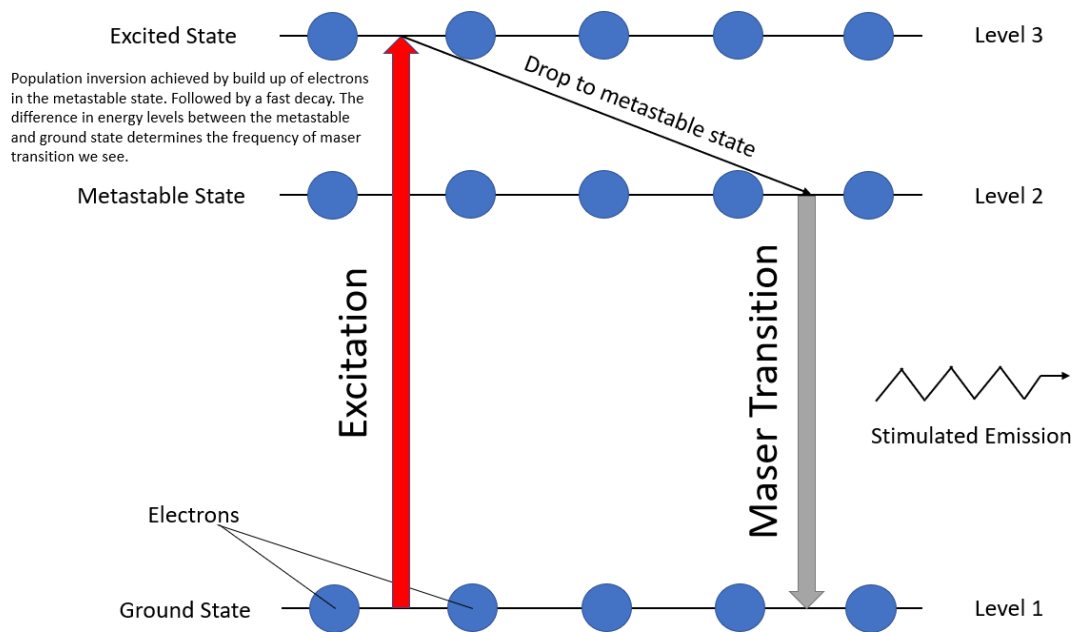


Figure 2.1: A diagram showing the excitation and de-excitation for an electron transitioning to and from the rotational metastable state in a three-level system population inversion. Image Credit : Recreation of a figure by Britannica School.

2.2 Collisional Pumping

Collisional pumping is the process by which class I masers are formed. This process involves particles within the gas, colliding with the electrons in the rotational ground state, which excites the electron to a higher angular momentum. This can, of course, occur in the exact opposite manner, whereby particles collide with electrons in higher rotational energy levels and cause the de-excitation of the rotational states in the molecule. These are aptly named collisional excitation and de-excitation. If the probability of collisional excitation is greater than de-excitation, this will cause a population inversion that is crucial for masing.

Class I masers that are collisionally pumped are often found in regions of space where molecules are shocked by energetic gas. This usually occurs in the bipolar outflows of stars, circumstellar disks and on the boundary of HII regions (Titmarsh et al., 2014; Billington et al., 2020). In relation to this study, the 22.235 GHz H₂O

masers are driven by collisional pumping, and so we would expect to find them in these regions.

2.3 Radiative Pumping

Radiative pumping is the process by which class II masers are produced. This process is a common occurrence in regions with a constant and energetic radiation being absorbed by electrons in the rotational ground state, which then get excited to a higher angular momentum. If the radiation is at the right energy and at a high enough intensity, this will be sufficient to maintain a population inversion in the molecule. The rotational states are then de-excited to an intermediate, metastable state, before decaying down to the rotational ground state through the stimulated emission process.

Class II masers are often found in proximity to hot cores, in HII regions, OH masers and near-IR sources (Fontani et al., 2010). This agrees with the definition above, which states that radiative pumping must coincide with an energetic emission of radiation, which all of these astronomical objects possess or are indicators of. The Class II 6.7 GHz methanol maser however is exclusively associated with MSF (Breen et al., 2013), and so is especially powerful at identifying these regions.

2.4 Methanol Maser Transitions

This thesis focuses on the Class II 6.7 GHz transition for methanol masers, however there are many metastable states and therefore many other transitions that can occur within methanol. Table 2.1 shows other Class II methanol maser transitions, followed by a short discussion on where they are typically located.

Transition	Frequency / MHz
$2_0 - 3_{-1}$	12179
$2_1 - 3_0$	19968
$9_2 - 10_1$	23121
$7_{-2} - 8_{-1}$	37706
$7_{-2} - 8_{-1}$	38293
$6_2 - 5_3$	38453

Table 2.1: A short list displaying a few of the other Class II methanol maser transitions.

We know that all Class II methanol masers are suspected to be associated with young high-mass star forming regions (Breen et al., 2013). However, the precise physical conditions and evolutions of SF regions that produce particular frequencies of methanol masers rather than others are not fully understood. Some of the conditions required in order to produce these masers are very precise and probably only occur within an incredibly brief evolutionary phase, resulting in some not being as widespread as others.

All of the maser transitions in Table 2.1 with the exception of the 12.2 GHz are expected to be associated with a brief evolutionary phase. The 12.2 GHz methanol transition is one of the strongest and most widespread methanol transition in the Class II bracket, just behind the 6.7 GHz transition. They are known to trace an early evolutionary stage of high-mass star formation and are therefore seen towards areas of 6.7 GHz methanol maser emission (co-spatial within a few milliarcseconds) (Ellingsen, 2006; Breen et al., 2012). While there seems to be a large overlap between these two transitions in terms of the physical conditions they form in (Cragg et al., 2005), there are observed differences in where they appear. For example, there has been no detected 12.2 GHz methanol maser that has not been associated with a 6.7 GHz maser, whereas there are plenty examples of 6.7 GHz masers with no 12.2 counterpart (Breen et al., 2012).

2.5 Water Maser Transitions

We choose to implement the use of the 22.235 GHz water maser transition in the thesis because it is by far the brightest and most widespread of the water masers. Also, this frequency has been searched for by the HOPS survey (Walsh et al., 2011, 2014), so we have much more information on the properties of the masers themselves.

There are other water maser transitions, which are listed in Table 2.2. These frequencies are opaque to our atmosphere, making it very difficult to observe them in any detail. Generally, we know from other studies that these water maser transitions are associated with SFRs and evolved stars, as is the case with the 22 GHz line (Cernicharo et al., 1990; Menten and Melnick, 1991; Menten et al., 1990; Menten, K. M. et al., 2008).

Transition	Frequency / GHz
$6_{16} - 5_{23}$	22.2
$3_{13} - 2_{20}$	183
$10_{29} - 9_{36}$	321
$5_{15} - 4_{22}$	325
$5_{33} - 4_{40}$	475

Table 2.2: A short list displaying a few of the other water maser transitions.

2.6 Statistics

This thesis uses a variety of statistical methods, and so to avoid repetition, the methods used will be discussed and explain in the following section.

2.6.1 p -value

The p -value, which stands for probability value, is the probability of obtaining at least the observed difference between two samples given that they are from the same population. The p -value can take any value between 0 and 1, since it is a probability measurement. Assuming that the two samples are from the same population is known as the null hypothesis, which is assumed to be true when calculating the p -value.

Therefore, a high p -value would indicate that it is very likely that any set of results obtained would result in a higher difference between two samples, and a low p -value indicates that it is very unlikely. Hence, a low p -value is often sought after in statistics, since it can reject the null hypothesis.

2.6.2 Kolmogorov–Smirnov Tests

The Kolmogorov-Smirnov test, also known as a KS test is a non parametric test that calculates the equality of a sample of a parameter with a known probability distribution, or with another sample. The former is known as the one-sample KS test and the latter is known as the two-sample KS test. In this thesis, the two-sample KS test is utilised extensively when comparing two parameters from different samples (such as different types of clumps) and is vital to the statistical analysis.

The KS test operates by taking the cumulative distribution functions (CDF) of both parameters and then taking the maximum distance between the two CDFs (see Figure 2.2), this is the KS statistic. The null hypothesis for the KS test is that the samples are drawn from the same population, which would mean that the parameter being measured from two populations are not significantly different from each other.

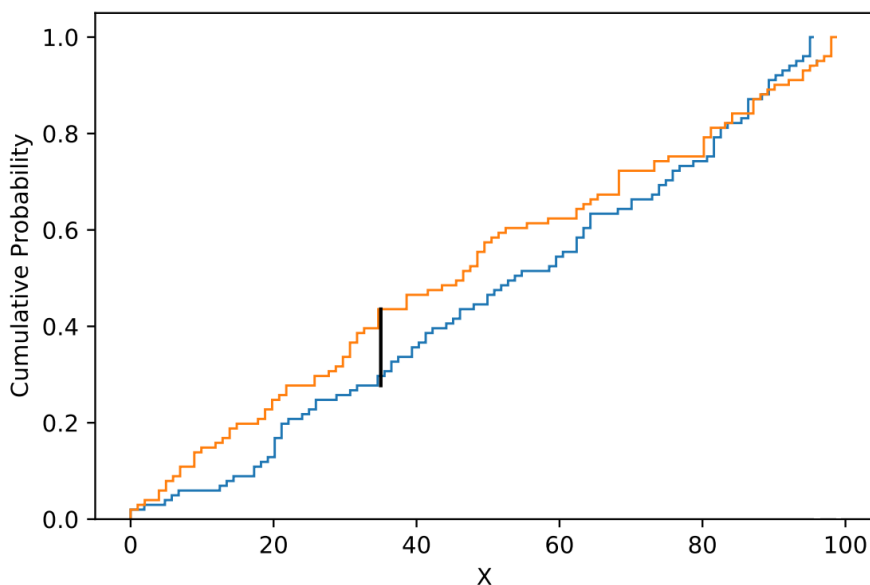


Figure 2.2: A graph showing the CDFs of two samples. The black line represents the maximum difference between the two CDFs and is equivalent to the KS statistic.

The KS statistic is also accompanied by a confidence value, known as the p-value. If the p-value is low enough, then it would be sufficient to reject the null hypothesis and determine that the two samples must be drawn from different populations. The generally accepted limit for the p-value to be low enough is taken as $p < 0.0013$, equivalent to a 3σ difference.

2.6.3 Spearman's Correlation

Spearman's Correlation is a statistical method to quantify how dependent two variables are on each other, and if this correlation happens to be negative or positive. The values can be anywhere between -1 and 1. The nature of the correlation is dependent on the sign of the value, so a negative value would suggest a negative correlation, and positive values would suggest a positive correlation. The strength of this correlation is then determined by the magnitude of the value, where -1 indicates a perfectly negative correlation, 1 indicates a perfectly positive correlation and 0 indicates no correlation between the two variables at all.

It should be noted that Spearman's correlation only works for monotonic associations. Monotonic associations are relationships where either; as one variable in-

creases so does the other, or as one variable increases, the other decreases. Examples of monotonic and non-monotonic associations can be seen in Figure 2.3.

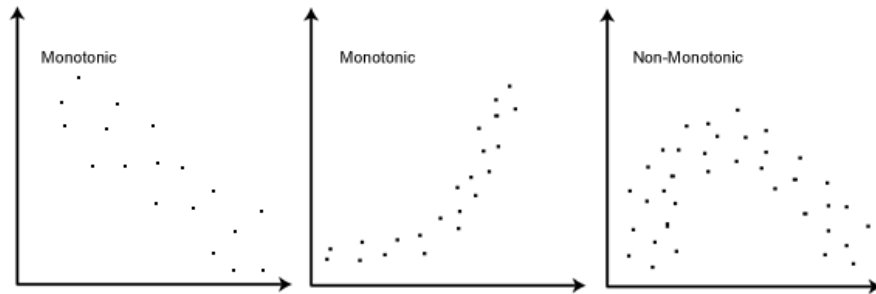


Figure 2.3: A series of graphs displaying monotonic and non-monotonic associations between two variables. Image credit: Laerd Statistics - <https://statistics.laerd.com/statistical-guides/spearmans-rank-order-correlation-statistical-guide.php>

Spearman’s correlation works by assigning ranks to each value in the list of the two variables. The variables are ranked 1 to N, where N is the sample size and the lowest value in the list, and 1 is the highest value in the list. It then takes these ranked values and performs the following calculation displayed in equation 2.1.

$$r_s = \frac{cov(R(X), R(Y))}{\sigma_{R(X)}\sigma_{R(Y)}} \quad (2.1)$$

Where r_s is the Spearman’s correlation score, $R(X)$ is the ranked values of variable X, $R(Y)$ is the ranked values of variable Y, $cov(R(X), R(Y))$ is the covariance matrix of the two ranked variables and $\sigma_{R(X)}$ and $\sigma_{R(Y)}$ are the standard deviations of the two ranked variables.

Much like the KS tests, the Spearman’s rank correlation tests also have p-values associated with the correlation score. This acts as a confidence score and determines how correct the correlation score is. Again, if the p-value is lower than 0.0013, then the null hypothesis that the two variables show no correlation between each other may be rejected.

2.7 Computer Programming Used For Data Analysis

In order to provide the analysis of the data presented in this paper, the use of Python and SQL programming languages were used in conjunction with each other.

SQL was mainly used to format the tables of data from the various surveys used in this study. It was also used to mass reduce the sample of data that was available in order to further analyse clumps / maser groups / maser spots with specific properties. This further analysis was then usually conducted with Python programming in order to find standard deviations, averages, p-values, KS tests and produce a variety of graphs for the reduced samples of data.

The SQL database was linked to the Python code using the following lines of Python code.

```
from sqlalchemy import create_engine
conn = create_engine('mysql+pymysql://root:root@localhost/
    world')

import pandas as pd
data = pd.read_sql_query('SQLQUERY', con=conn)
```

This method utilises the pandas module and the sqlalchemy module. The database can be linked by creating a connection through the “create engine” module, followed by using the pandas module to read a piece of SQL code in that database. The variable labelled “data” now represents the table that would have been created in SQL from the SQL code, which is labelled here as “SQLQUERY”. The table from SQL the SQL database is now in Python format, where it can be analysed further with Python coding.

As previously mentioned, Python was also used to produce all of the multi-wavelength images used in this thesis via the aplpy module. This is an example of the code to produce a standard three colour image.

```

import aplpy

csc_outliers = [#Can enter desired clump names here and turn
    this into a loop]

red_filter = #Fits file of longest wavelength.
green_filter = #Fits file of middle wavelength.
blue_filter = #Fits file of shortest wavelength.

rgb_cube_filename = #Generic filename
output_filename = #Generic filename

aplpy.make_rgb_cube([red_filter , green_filter , blue_filter] ,
    f"{rgb_cube_filename}.fits" , "galactic")
aplpy.make_rgb_image(f"{rgb_cube_filename}.fits" , f"{
    output_filename}.png")

```

The `csc_outliers` list would normally be filled with clumps that we wish to produce multi-wavelength images of. The red, green and blue filter represent fits files for three wavelengths of the clump we wish to make the image from. The `aplpy` module is used to make an rgb cube with these filters and store it as the variable “`rgb_cube_filename`”. The `aplpy` module also has a built in feature to convert to galactic coordinates, which is important here, since the fits files being used work on this coordinate type. The three colour image can be made from the rgb cube and saved as the variable labelled, “`output_filename`”.

Chapter 3

In-Depth Breakdown of the Surveys

We will now discuss a variety of the surveys to be used throughout this study. There are six surveys that we discuss overall, three of these are used to produce multi-wavelength images for the visual inspection of sources. The other three contain useful data about the physical parameters of star forming clumps, the maser properties of water and methanol species and which clumps are associated with particular maser species.

It is therefore important to discuss all six surveys in detail. We will start with the multi-wavelength surveys, where we talk about their goals, the wavelengths they have mapped and at what resolution and the equipment they use. We will then move on to the discussion of the clumps and maser surveys, which includes a basic outline of their goals, the detections of sources and their various papers.

The final part of this chapter will also look to discuss the overlapping region of the HOPS, ATLASGAL and MMB surveys, which will outline the region where data from all surveys is available to us.

3.1 Continuum surveys

GLIMPSE

GLIMPSE (Galactic Legacy Infrared Mid-Plane Survey Extraordinaire) is a survey of the sky at infrared wavelengths from the Spitzer Space Telescope (Werner et al., 2004). The main objectives of the GLIMPSE survey were to contribute to a deeper understanding of the physics of interstellar dust, star formation, and the large-scale structure of the Milky Way as traced by stars (Churchwell et al., 2009). The wavelengths observed are 3.6, 4.5, 5.8, and 8.0 μm all at a spatial resolution of < 2 arcseconds, which were all taken by the IRAC (Infrared Array Camera) (Fazio et al., 2004) on the Spitzer Space Telescope.

WISE

WISE (Wide-Field Infrared Survey Explorer) (Wright et al., 2010) is a mission that launched the WISE space telescope into orbit around the Earth to observe the whole sky at infrared wavelengths. Its main objectives were to find the closest stars to the Sun, detect most asteroids in the main belt larger than 3 km, find the most luminous Galaxies in the Universe and enable a wide variety of studies to come about such as star formation in Galaxies. They have mapped out 3.4, 4.6, 12.0 and 22 μm at spatial resolutions of 6.1", 6.4", 6.5" and 12.0" respectively. Since similar wavelengths to 3.4 and 4.6 μm have already been mapped out by the IRAC, the 12.0 and 22.0 μm wavelengths are particularly important for this thesis.

Hi-Gal

Hi-Gal (Herschel infrared Galactic Plane Survey) (Molinari et al., 2016) is another crucial multi-wavelength survey that traces five wavelengths in the sky; 70, 160, 250, 350 and 500 μm . The observations are made at the Herschel Space Observatory (Pilbratt et al., 2010), which was built and launched by the European Space Agency. This observatory had two cameras on-board, the SPIRE (Spectral and Photometric Imaging Receiver) and PACS (Photodetecting Array Camera and Spectrometer). The PACS camera images photometry in the 60 - 210 μm range (Poglitsch et al.,

2008) whereas the SPIRE camera images in three wavebands; 250, 350 and 500 μm (Griffin et al., 2010).

3.2 Multi-Wavelength Image Examples

Using the GLIMPSE, WISE and Hi-Gal surveys, we can now create multi-wavelength images for most clumps in the ATLASGAL database. This is a vital step in the analysis of the clumps, since it allows us to identify astrophysical features that are driving maser emission and provide context for the physical parameters of the clump by visual inspection.

The first thing we must understand is why it is important to view these stellar clumps in various wavelengths. This is because different wavelengths trace different astrophysical processes based on the temperature of the source of the radiation. The longer the wavelengths, the cooler the object, and vice versa.

In this thesis, we choose to use two sets of wavelengths to create two three-colour images for each clump. They are 4.6, 5.8 and 8.0 μm (spatial resolutions $< 2''$) images taken from GLIMPSE as well as 8.0, 22 (12'') and 70 μm (5'') emission, which are taken from the GLIMPSE, WISE and Hi-Gal surveys, respectively. All of these wavelengths reside in the infra-red region of the EM spectrum. Infra-red emission is helpful because it shows the location of important features in the clump. Shorter wavelengths of mid-infrared (3-8 μm) can show hot objects such as evolved stars and HII regions. At the longer wavelengths of the mid-infrared range (22 μm) we can see hot cavities of dust left behind by HII regions as well as dust heated by YSOs and at the far-infrared (70 μm) we can see sites of young, cool protostellar objects, which indicate the location of star forming regions.

We also plot the contours of the 870 μm emission from the ATLASGAL database over these three-colour images. This is important because the 870 μm emission traces the cold dust of the molecular clumps, therefore it provides a rough outline of the shape of the clump. These contours are produced by using a dynamic power law, which starts at the 3σ peak image intensity and spaced by 3σ (see Thompson

[et al. \(2006\)](#) for more information).

Additionally, we can plot the locations of the Class II 6.7 GHz methanol masers and 22.235 GHz H₂O masers from the MMB and HOPS surveys onto the images. This will allow us to determine if the masers are associated with a particular emission, which will then allow us to determine their origin.

When combining all of this information into a single image, the result can be seen in [Figure 3.1](#).

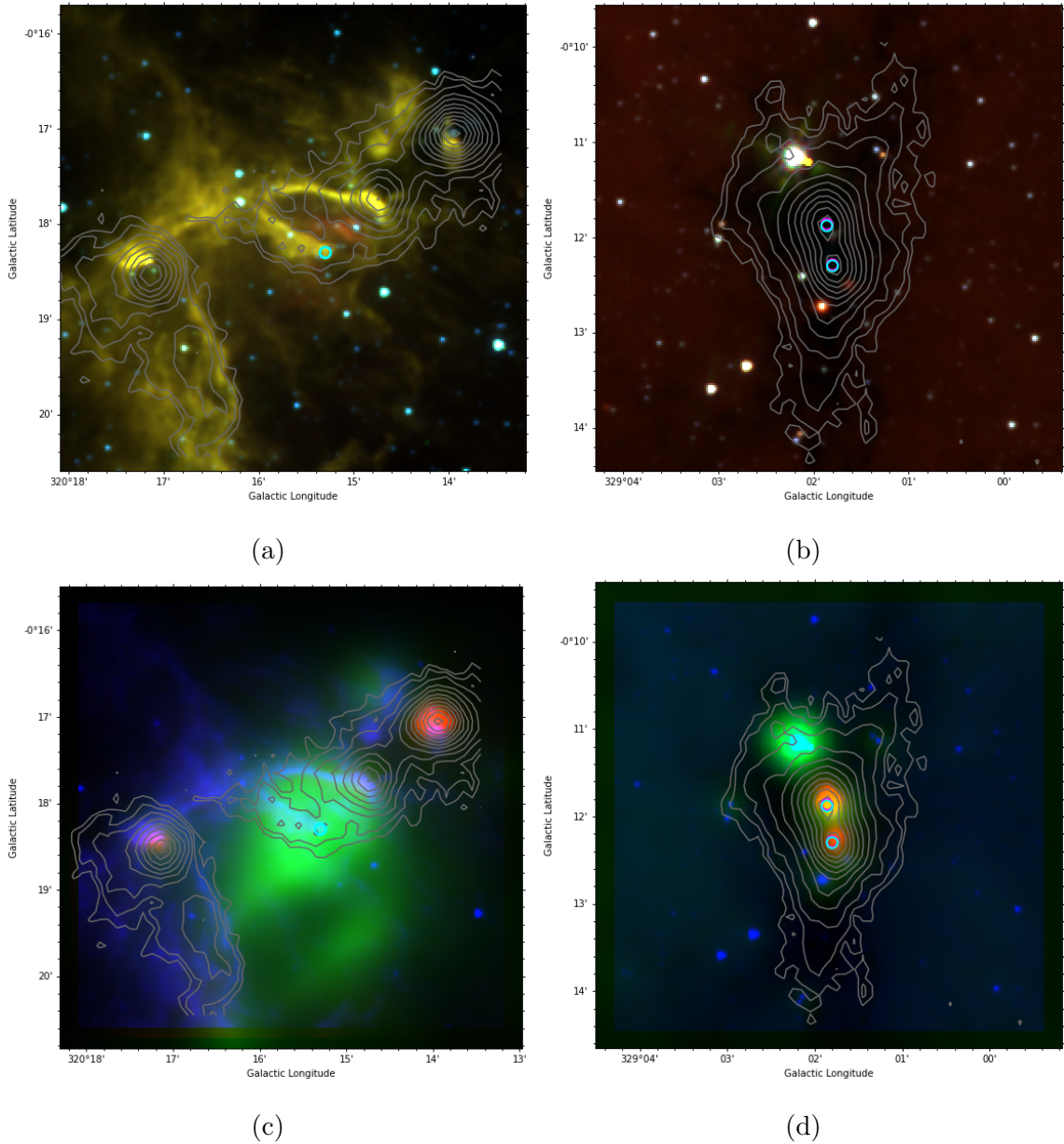


Figure 3.1: Two clumps represented with two types of multi-wavelength images created using the IRAC band filters. The left panels show AGAL320.264-00.301, whereas the right panels show AGAL329.029-00.206. The top panel shows 4.6, 5.8 and 8.0 μm wavelengths in blue, green and red respectively. The bottom panel represents 8.0, 22 and 70 μm wavelengths as blue, green and red colours respectively. The grey contours represent the sub millimetre emission from ATLASGAL. Methanol masers are represented by the purple circles, whereas water masers are represented with the cyan circles. As a side note, in some of these images the purple circles are hidden behind the cyan circles.

In Figure 3.1, we can see a variety of the astrophysical features that will be observed in Chapters 5 and 6. Figure 3.1a shows an example of a HII region, which is represented by the yellow emission (5.8 - 8.0 μm) spread throughout the clump. HII regions are a precursor to MSF and can trigger star formation along their HII fronts via photoionisation shocks (Elmegreen and Lada, 1977). This makes them some of the most important features that we will observe, considering the focus of this thesis is the study of star forming regions. We can also see that a water maser is located on the edge of this HII region, so there is a very high probability that this water maser is being shock excited where the boundary of the HII region meets the ambient material in the clump.

Not all of the features that we wish to observe are available in 4.6, 5.8 and 8.0 micron emission. The main feature that we will not be able to see in these wavelengths are young, protostellar objects that are deeply embedded in their natal cloud. This is because these younger objects are also cooler, and so will emit at longer wavelengths. AGAL329.029-00.206 is a perfect example of why we need to utilise the 8.0, 22 and 70 μm bands when observing these clumps. In Figure 3.1b, there is no visible emission towards the centre of the clump, however the 70 μm emission in Figure 3.1d reveals the YSOs that were hidden by the shorter wavelengths. We also see that AGAL320.264-00.301 benefits from these longer wavelengths as well, since the green, 22 μm emission in Figure 3.1c reveals a hot pocket of dust left behind by the HII region. This feature was also previously invisible when only imaging mid-IR wavelengths.

This section should have prepared the reader for the multi-wavelength images of the clumps that we will become familiar with in Chapters 5 and 6, as well as provide context for why we use particular wavelengths to image these clumps.

3.3 Clump / Maser Surveys

MMB

The MMB survey searched the southern and northern hemisphere in search for Class II 6.7 GHz methanol masers. The survey covered $186^\circ \leq l \leq 60^\circ$ (through the Galactic centre) with $|b| \leq 2^\circ$. The purpose of the survey was to find these specific maser lines since they are unique to high-mass star formation and can trace systematic velocities. These, in conjunction with other methanol maser species, can explore the evolution of the associated high-mass star (Breen et al., 2015).

The observations were initially taken with Parke’s 64m telescope that raster scanned the Galactic plane in survey cubes of 20° longitude by the 4° latitude that the survey covers. These cubes were then searched for any methanol maser emission. However the Parke’s telescope has a low spatial resolution at 3.2 arcmins, so follow-up observations were then carried out by either ATCA (Australia Telescope Compact Array) or MERLIN (Multi-Element Radio Linked Interferometer Network), which are both arrays of antennas that are able to provide more precise observations. These obtained arcsecond precision for the sources and have higher spatial resolutions so that sources were not blended (ATCA with a few arcsec and MERLIN with 43 mas).

A varying number of sources were discovered in each longitude range, some more than others. Table 3.1 provides a detailed breakdown of how many masers, how many new masers and the percentage of new masers that were found in each longitude range, as well as a reference to the paper they are reported in. As a side note, the methanol masers were published in this series of papers as the high-resolution positions became available.

Table 3.1: Breakdown of maser detections in the MMB survey within the 5 different longitude ranges.

Longitude Range	Methanol Maser Detections	New Maser Detections	Reference
$186^\circ \leq l \leq 330^\circ$	207	89	Green et al. (2012)
$330^\circ \leq l \leq 345^\circ$	198	86	Caswell et al. (2011)
$345^\circ \leq l \leq 6^\circ$	183	58	Caswell et al. (2010)
$6^\circ \leq l \leq 20^\circ$	119	42	Green et al. (2010)
$20^\circ \leq l \leq 60^\circ$	265	64	Breen et al. (2015)

A total of 972 Class II 6.7 GHz methanol masers were identified within the MMB survey including a total of 339 new detections, which result in 34.9% of masers being new detections. The lowest percentage of new detections occurred in the $20^\circ \leq l \leq 60^\circ$ range with only 24.2% of detections being new. This was to be expected because this was probed by two other methanol maser surveys that operated in longitudes within this range ([Pandian et al., 2007](#); [Szymczak et al., 2002](#)).

The MMB survey includes many important parameters for each methanol maser such as distance, velocity, flux density and angular offset. These are all crucial to the survey as it allows interesting objects to be found and helps to build up an idea of the local environments that are driving the masers. More on the statistics of the MMB survey were presented in [Green et al. \(2017\)](#) which investigates distributions in flux density and the variability of source velocities, as well as new distance calculations to 202 sources in the survey.

HOPS

The HOPS survey aimed to search the skies for H₂O masers, specifically the 22.235 GHz line. It is an unbiased survey and searched between $290^\circ \leq l \leq 30^\circ$ with $|b| \leq 0.5^\circ$. The main motivation for the survey is that previous searches for these H₂O masers had been targeted toward regions that were expected to find such masers ([Walsh et al., 2014](#)), hence the full population is unknown. The survey also wanted to determine the proportions of astrophysical phenomena that these masers are associated with, since this was not fully understood at the time.

Observations were carried out with the Mopra telescope (Figure 3.3a) with a detection limit of 1-2 Jy and a spatial resolution of 2 arcmin. This spatial resolution was too low to resolve individual water masers. For this reason, a group of water masers in close proximity to each other were classified as water maser sites (referred to as water maser groups in this thesis), while the individual water masers within that site were labelled as water maser spots. These spots were identified via the peaks of emission in the maser velocity spectrum using VLBI methods to resolve them (See Figure 3.2). Follow-up observations were made with ATCA (Figure 3.3b), which has much higher resolution (0.55×0.35 arcsec beam) than the Mopra telescope and was able to study these maser sites more closely.

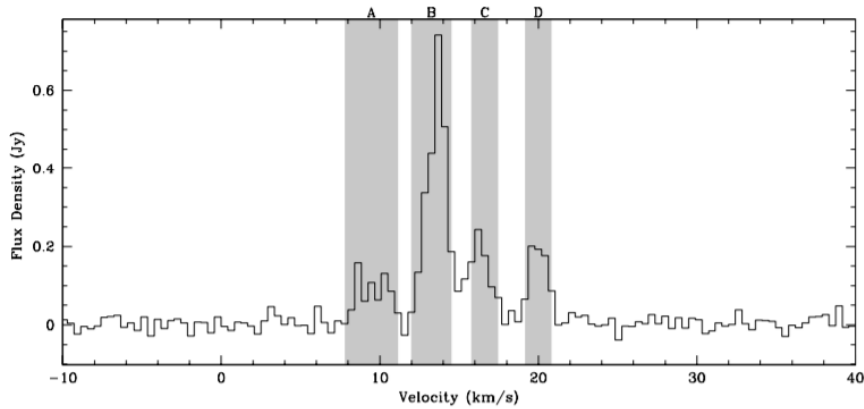


Figure 3.2: Velocity channel of a water maser group, which reveals individual peaks of flux (the grey shaded regions) corresponding to water maser spots. Image Credit: [Walsh et al. \(2014\)](#)

In the first paper ([Walsh et al., 2011](#)) there were confirmed to be 540 maser sites with detected emission, 334 of these were new to the HOPS survey. However, in the follow up paper ([Walsh et al., 2014](#)) it was noted that there were multiple detections of maser sites within some of these fields due to improved resolution, and so the number of water maser sites rose to 631. This corresponded to 2790 individual water maser spots.

Many of the maser sites in HOPS survey have been associated with an astrophysical object, which was the main goal of the survey. This was done by comparing the

maser groups to the literature. The breakdown of the distribution of water maser groups and their astrophysical association can be seen in Table 3.2.



(a) A photograph of the MOPRA telescope in Australia.

Credit : www.kickstarter.com/projects/astrocate/teammopra-save-a-telescope-and-map-the-milky-way



(b) A photograph of the Australia Telescope Compact Array.

Credit : CSIRO

Table 3.2: Distribution of water maser groups with astrophysical phenomena.

Astrophysical Object	No. of Water Maser Groups	Percentage	Average Number of Spots
Star formation	433	69	3.76
Evolved stars	121	19	4.58
Unknown	77	12	3.19

From Table 3.2, it can be seen that H₂O masers were found to be primarily associated with star formation at $\sim 70\%$, followed by evolved stars and then unknown associations.

It was also found in Walsh et al. (2014) that there were 31 non-detections towards pointing centres that were identified in Walsh et al. (2011). It was concluded that this was likely due to the intrinsic variability of these masers, which means they were emitting weakly at the time of these follow-up observations.

ATLASGAL

ATLASGAL is an unbiased 870 μm sub-millimetre survey of the inner Galactic Plane. It covers the $300^\circ \leq l \leq 60^\circ$ with $|b| \leq 1.5^\circ$ range and was later extended to $280^\circ \leq l \leq 300^\circ$ with $-2^\circ \leq b \leq 1^\circ$. The main aim of the survey was to create a complete sample of all massive, dense clumps ($\geq 1000 M_\odot$) in the Galaxy up to a heliocentric distance of 20 kpc. This was achieved by measuring the dust continuum emission at 870 μm , which is useful for mapping out abundance of material and density. This would encompass every stage of early massive star formation, which could then be studied further, since current knowledge of massive star formation is still a relatively unknown phenomenon in astronomy. Another purpose of this survey was to take note of the distribution of these dust clumps throughout the Galaxy and whether they are more likely to be located in specific regions e.g higher density regions such as spiral arms.

The first paper (Schuller et al., 2009) for ATLASGAL outlined the project and presented the first results for the survey. It surveyed ~ 95 square degrees of the inner Galactic plane and detected ~ 6000 compact sources above 0.25 Jy, which was the 5σ detection limit of the telescope used by the Atacama Pathfinder Experiment telescope (APEX). The detector on the APEX telescope is the Large APEX Bolometer Camera (LABOCA), which is a 295 element bolometer array. The LABOCA detector was used for observations in every paper for the ATLASGAL survey.

The second paper (Contreras et al., 2013) presented the compact source catalogue (CSC) that provided a total of 6639 clumps in the range $330^\circ \leq l \leq 21^\circ$ with

$|b| \leq 1.5^\circ$. This identified clumps and their parameters with the help of the source extraction algorithm, SExtractor (Bertin and Arnouts, 1996).

The third paper (Urquhart et al., 2014a) identifies 3523 more compact sources, bringing the total number of clumps to 10,163. This was observed between $280^\circ \leq l \leq 330^\circ$ and $21^\circ \leq b \leq 60^\circ$ with a survey sensitivity of $0.3 - 0.5 \text{ Jy beam}^{-1}$. These sources were also identified using the SExtractor.

The follow-up paper (Urquhart et al., 2018) presented the properties (luminosity, distance, mass) to a complete sample of ~ 8000 dense clumps within the ATLASGAL survey. This was within a range of $5^\circ \leq |l| \leq 60^\circ$, the inner 5 degrees were not included due to problems with source confusion. The distance calculations are arguably the most important aspect for this thesis since all of the physical parameters can be calculated as a result of knowing the physical distance to the clumps.

3.4 Overlapping Regions

The combination of these 3 surveys are powerful, since they provide a large region where the high-mass star forming regions can be investigated in a uniform way and the statistical properties and correlations will be reliable.

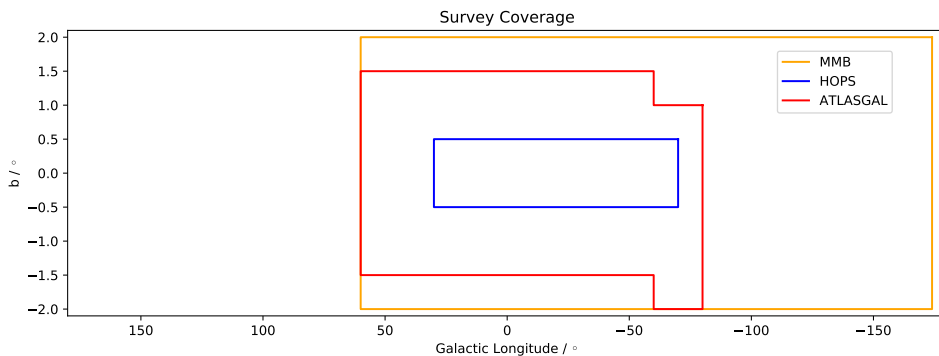


Figure 3.4: A plot showing the coverage of all surveys including longitude and latitude.

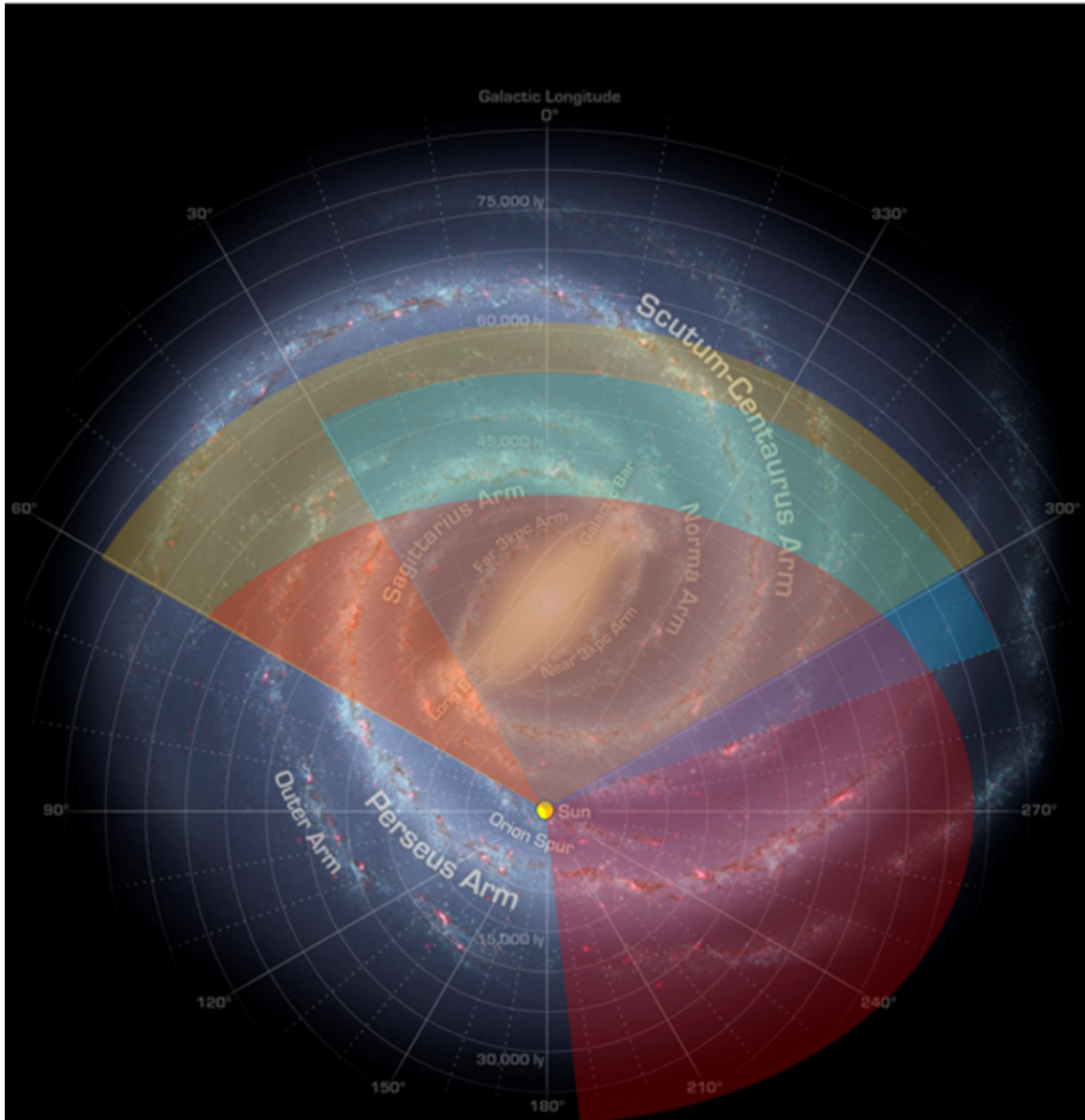


Figure 3.5: An image of three survey coverages that are all overlaid onto a top-down view of the Milky Way. The yellow, blue and red sectors represent the ATLASGAL, HOPS and MMB surveys respectively. The yellow dot is the position of the Sun in our Galaxy. It should be noted that the different heliocentric distances of the sectors are not accurate, they were only made different so that the sectors did not completely overlap each other and obscure certain surveys. Image Credit : NASA/JPL-Caltech/R. Hurt (SSC/Caltech).

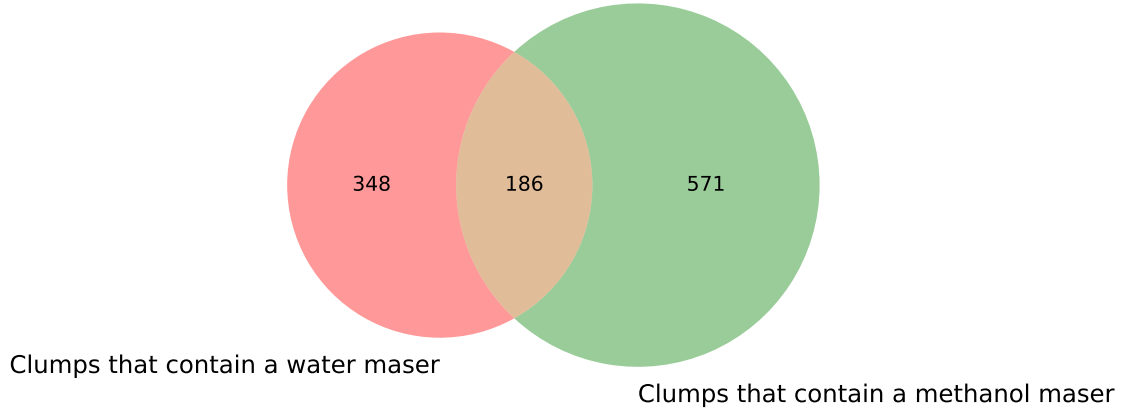


Figure 3.6: This Venn diagram illustrates the breakdown of clumps that contain methanol and water masers in the tri-survey coverage range.

Figure 3.4 shows the coverages of all three surveys discussed, and allows for a clearer understanding of how they overlap. Since the HOPS survey fits completely inside both the MMB and ATLASGAL surveys, this is the region in which all 3 surveys are fully mapped. Specifically, this happens at $290^\circ \leq l \leq 30^\circ$ with $|b| \leq 0.5^\circ$, which will now be referred to as the “tri-survey coverage range”. We also present Figure 3.5, which gives a more visual aid of how these surveys overlap with respect to the Milky Way Galaxy.

Within the tri-survey coverage range, there are a total of 6775 dense and massive clumps identified by ATLASGAL. Of these clumps, 5458 of them had further parameters calculated by [Urquhart et al. \(2018\)](#). The remaining clumps that did not have their parameters calculated were either located in the inner 6 degrees of the Galactic plane or were located between $290^\circ \leq l \leq 300^\circ$, both of these sub-regions within the tri-survey coverage were not targeted by [Urquhart et al. \(2018\)](#).

The tri-survey coverage range also contains 633 6.7 GHz class II methanol masers and all of the 22.235 GHz H₂O masers from the HOPS survey (631 water masers) since the HOPS coverage and the tri-survey coverage are equivalent. The methanol masers were all contained within 571 unique clumps whereas the water masers were all contained within 348 unique clumps. Overall, there are a total of 688 distinct

clumps within the tri-survey coverage range that contain at least one maser and 186 distinct clumps in the tri-survey coverage range that contain at least one example of both species of maser. These statistics can be viewed in Figure 3.6.

Now that we have discussed all three of the surveys that contain the majority of the data to be used in this thesis, we can start using this data to begin our analysis. The next chapter will look to investigate the physical parameters of the massive and dense clumps, along with their 22 GHz water and 6.7 GHz methanol maser associations. The dependency of the quantity / offset of masers on the physical conditions such as luminosity and mass, could give us a significant insight into these MSF regions.

Chapter 4

Water Masers and Evolution

4.1 Outline

Before exploring the relationship between 22.235 GHz H₂O masers and a clump's evolution, it should be noted that a similar study was already conducted in [Billington et al. \(2020\)](#), where they investigated clumps associated with 7 different maser transitions. These were the 6.7 & 12.2 GHz methanol masers, 22.2 GHz water masers, and the masers emitting in the four ground-state hyperfine structure transitions of hydroxyl.

It was found that the associated clumps have similar physical properties including the luminosity-to-mass ratio, which indicated that they were at very similar evolutionary stages.

However, [Billington et al. \(2020\)](#) only looked at the properties of the maser associated clumps in isolation and did not investigate clumps with multiple masers in detail, which is what we will focus to do in this chapter. We do this by categorising three groups of clumps, these are clumps that contain only 22.235 GHz H₂O masers, clumps that contain only Class II 6.7 GHz methanol masers and clumps that contain both of the aforementioned masers. These clumps will be labelled as Water Maser Only (hereafter WMO clumps), Methanol Maser Only (hereafter MMO clumps) and Both Masers (hereafter BM clumps), respectively. We also compare these samples

to the ATLASGAL sample, which represents all clumps in the ATLASGAL survey, including those with no maser sources.

It should be noted that in [Billington et al. \(2020\)](#) and this thesis, the evolution of a clump is measured by its luminosity-to-mass ratio (hereafter L/M ratio). This is because we expect clumps that have higher luminosities to contain young protostars that are more luminous. These more luminous stars are most often found late into their accretion phase, and since stars accrete their mass over a long time period, they are more evolved. The mass of the natal clumps of more evolved stars will also decrease as they blow away their natal cloud of gas and dust, thus the conclusion is that more evolved stars have increased luminosities and decreased masses, therefore the clumps in which they reside will have a higher L/M ratio. Conversely, clumps that are less evolved are therefore expected to have lower L/M ratios. [Figure 4.1](#), displays an L/M plot from [Molinari et al. \(2008\)](#) where several sources (both low and high-mass stars) are shown to exhibit the process described here.

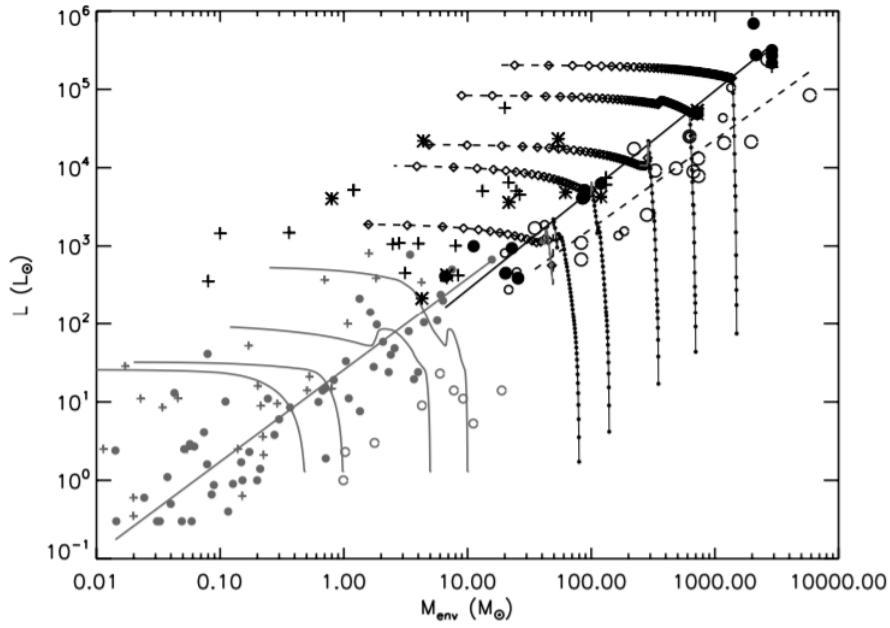


Figure 4.1: A Luminosity - Mass plot of several low and high-mass stars. The mass is first shown to stay the same while the luminosity increases rapidly, then the second stage shows that the mass rapidly decreases as the envelope is blown away from the star. The circles show actual measurements of these stars, whereas the curves are predictions from models. Image credit : [Molinari et al. \(2008\)](#)

In this chapter, we will first look at the luminosity and mass parameters between the three types of maser associated clumps defined earlier before comparing the L/M ratio. We will then look at the maser properties of these types of clumps and investigate if there is a link between the properties of these masers and the physical conditions of the clump.

4.2 Physical Properties of Clumps

The first set of data that we will investigate is the physical parameters of WMO, BM and MMO clumps. The physical parameters to be investigated in further detail are the luminosity, mass and L/M ratio. In order to compare and contrast the physical parameters for these maser associated clumps, we will implement the use of various statistical analysis tools.

We will first utilise the KS tests that were briefly discussed in Section 2.6. This will provide a p-value, that will specify if the two samples can be considered significantly different from each other. As seen in Section 2.6, if the p-value < 0.0013 we will be able to say that the two samples are not drawn from the same population. The cumulative distribution functions (CDFs) for these parameters are shown in Figure 4.2. Tables 4.1 and 4.2 provide the results of the KS tests between all the different combinations of samples and parameters from the CDF plots.

We also provide the mean values of the physical parameters of these samples in Table 4.3. These exist to simply describe the physical parameters of the samples, and provide additional data for comparisons between samples along with the KS tests.

The uncertainties for the averages in Table 4.3 and subsequent tables in this study are calculated from the standard error, which is just the standard deviation divided by the square root of the sample size. Additionally, any uncertainties for the sample sizes are calculated from Poisson counting error, which is simply equal to the square root of the sample size. Both of these are discussed in Section 2.6.

We use a distance limited sample between 2-4 kpc, this ensures that parameters that are heavily skewed by distance will not affect our results. Our distance limited sample size is approximately 3200 clumps.

The luminosity and mass measurements for clumps are taken from the list of bolometric luminosity values and the full width half maximum (FWHM) values of the mass determined by the ATLASGAL survey (Urquhart et al., 2022). The FWHM values are determined from taking the source size to be the pixels above the half power level, which removes biases whereby more evolved clumps would appear to have larger volumes and less density (Billington et al., 2019).

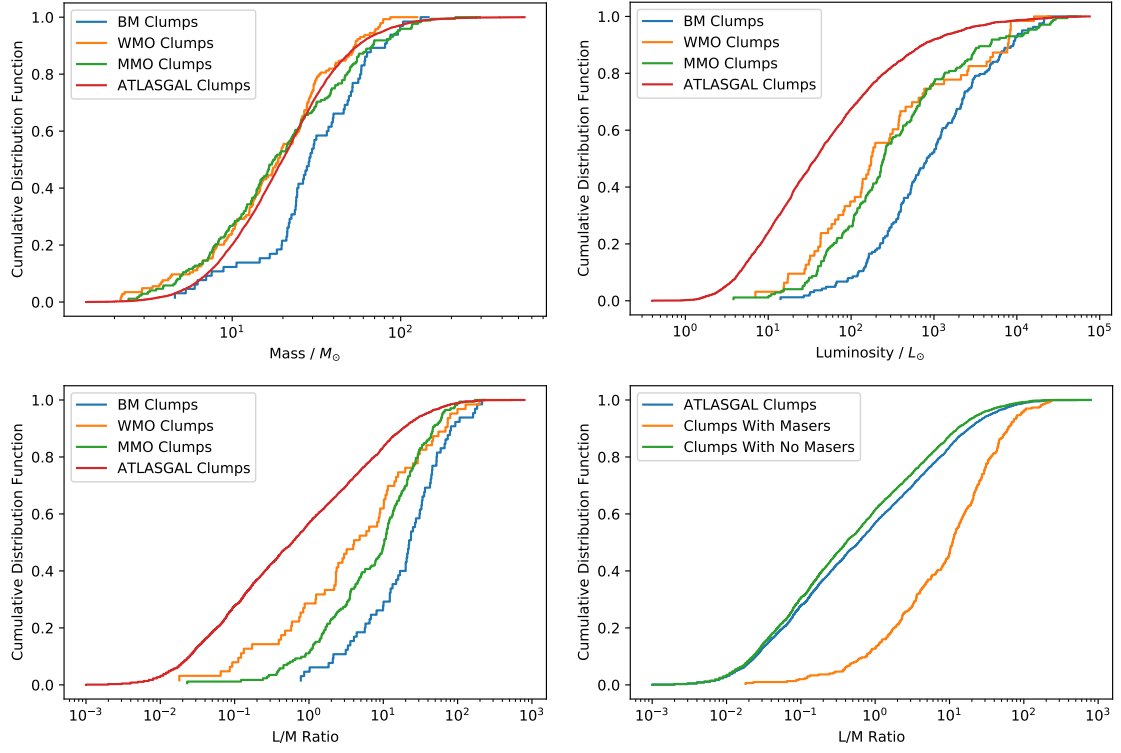


Figure 4.2: CDF plots for the physical parameters of stellar clumps with various maser associations.

Table 4.1: A breakdown of the KS test results for different combinations of maser associations. The results of this KS test for the three physical parameters are then listed, which includes the KS statistic and the p-value. Significant p-values ($\ll 0.0013$) are highlighted in yellow.

Samples Compared	Mass		Luminosity		L/M Ratio	
	KS Stat	p-value	KS Stat	p-value	KS Stat	p-value
BM / WMO	0.359	1.19×10^{-5}	0.368	5.21×10^{-6}	0.406	3.15×10^{-5}
BM / MMO	0.354	8.83×10^{-6}	0.32	4.23×10^{-8}	0.307	0.00019
BM / All	0.324	1.58×10^{-6}	0.63	2.22×10^{-16}	0.604	6.71×10^{-23}
WMO / MMO	0.101	0.37	0.13	0.35	0.187	0.0679
WMO / All	0.0642	0.582	0.36	7.21×10^{-8}	0.339	7.51×10^{-7}
MMO / All	0.0864	0.152	0.42	3.53×10^{-27}	0.464	2.22×10^{-16}

Table 4.2: KS Tests between the samples shown in the bottom-right panel of Figure 4.2 regarding the L/M ratio. Significant p-values ($\ll 0.0013$) are highlighted in yellow.

Samples Compared	L/M Ratio	
	KS Stat	p-value
Clumps With Masers / Clumps With No Masers	0.50	2.44×10^{-62}
Clumps With Masers / ATLASGAL Clumps	0.45	2.0×10^{-15}
Clumps With No Masers / ATLASGAL Clumps	0.047	0.0025

Table 4.3: The average values of the physical parameters for various maser associated clumps, accompanied by the sample size of which each average was taken from.

Type	Sample Size	L/M Ratio	Luminosity / L_{\odot}	Mass / M_{\odot}
WMO	63	27.8 ± 9	2080 ± 552	31 ± 2.6
MMO	172	20 ± 2.2	2497.5 ± 550	32 ± 2.9
BM	65	41 ± 6.2	4650 ± 1044	40 ± 3.7
ATLASGAL	(~ 3200)	7.6 ± 0.5	646 ± 62	29 ± 0.5

Key Observations

- The plots shown in Figure 4.2 and the results of the KS tests in Table 4.1 reveal that the mass, luminosity and L/M ratios of BM clumps are found to be significantly larger from the WMO, MMO and ATLASGAL clumps (see Table 4.3 for specific values).
- We find no difference between the physical parameters of WMO and MMO clumps, which is in line with results from Billington et al. (2020).
- We find that the four samples appear to fit into three categories of luminosity, with the ATLASGAL sample having the lowest luminosities, BM clumps exhibiting the highest luminosities and WMO and MMO clumps showing luminosities that range somewhere between the other two (see Table 4.3). At

luminosities of the order $10^4 L_{\odot}$ the MMO clumps do seem to approximate the BM clumps, however this is only for a very limited part of the CDF and the KS test still confirms them as significantly different.

- ATLASGAL clumps show significantly lower luminosities and L/M ratios than any other sample of clumps. The vast majority of clumps in the ATLASGAL sample have no maser emission, indicating that clumps with no masers have significantly lower luminosities than clumps that do, perhaps suggesting they are less evolved.

4.3 Maser properties

Now that we have investigated the differences in the physical parameters of the maser associated clumps, it is a good idea to look more closely at the masers themselves.

We will first search for differences in maser properties between the WMO and BM clump samples by using KS tests (Table 4.4) and CDF plots (Figure 4.3). The maser properties we will investigate are; the maser offsets (positional offset of the maser from $870\mu\text{m}$ peak of the clump), the quantity of water maser spots and the flux of water maser groups. This will indicate whether certain parameters for masers can be used to trace more evolved clumps. The maser offset may be potentially interesting, since clumps with higher maser offsets may require the clump to be more evolved so that various phenomena capable of triggering these masers are more likely to be further from the centre.

We will then detect if there is any correlation between any of the aforementioned maser properties and the physical parameters of the clump by using Spearman's correlation tests (Table 4.4). These correlations will not be targeted towards the clump properties of BM or WMO samples specifically, but rather both samples to give a more general sense of the correlation between masers and the physical parameters of the clump. We present scatter plots showing the number of water maser spots and the clump properties in Figure 4.4.

We do not investigate the quantity of methanol masers per clump, since there is

only a maximum of 3 methanol masers in any clump, and this will not be enough to determine if MMO clumps display more or less methanol masers than BM clumps.

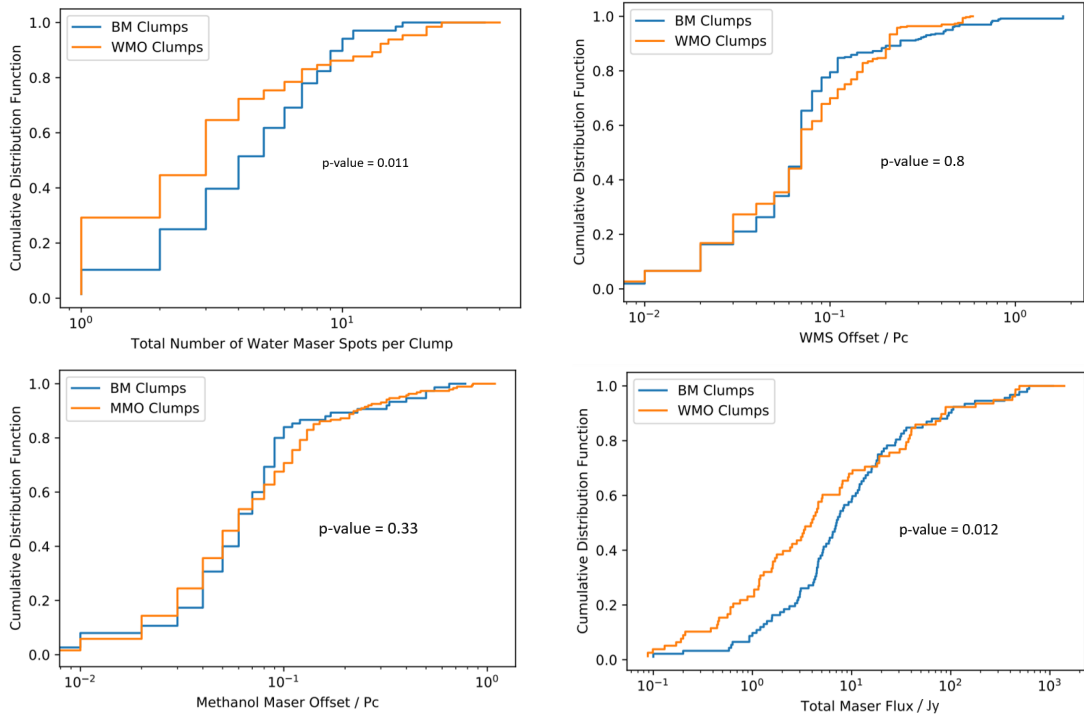


Figure 4.3: The top-left panel shows the CDFs of BM and WMO clumps for the total number of WMS per clump. The top-right panel shows the CDFs for the WMS offset. The bottom-left panel shows the methanol maser offset. The bottom-right panel shows the total maser flux.

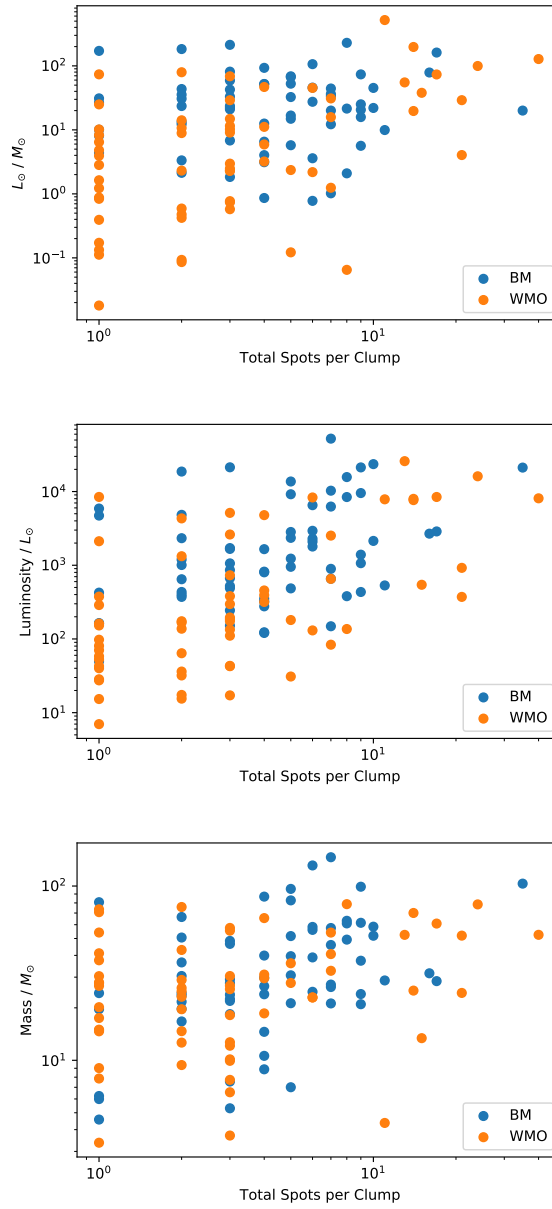


Figure 4.4: Scatter plots between the total number of WMSs per clump and the L/M ratio, Luminosity and Mass of the clump shown in the top, middle and bottom panel, respectively.

Table 4.4: The results of the Spearman correlation tests performed between the maser and clump properties. Significant p-values ($\ll 0.0013$) are highlighted in yellow.

	Luminosity		L/M Ratio		Mass	
	Correlation	p-value	Correlation	p-value	Correlation	p-value
Offset of WMSs	-0.0596	-0.0326	-0.172	0.391	0.0314	0.409
Quantity of WMSs	0.526	10^{-10}	0.375	10^{-5}	0.371	10^{-5}
Flux of WMG	0.393	10^{-7}	0.375	10^{-6}	0.132	0.0982

Key Maser Observations

- There is no significant difference in the water maser flux, total number of WMSs or water maser offset when looking between BM and WMO clump samples. This is confirmed by the KS tests performed in Figure 4.3. The water maser flux does seem to be significantly higher in BM clumps for lower values. However, the water maser flux for BM clumps approximates the WMO sample for fluxes > 20 Jy.
- The total number of WMSs per clump has a positive correlation with the L/M ratio (Correlation = 0.375, p-value = 1.39×10^{-5}), the Luminosity (Correlation = 0.526, p-value = 2.09×10^{-10}) and the Mass of a clump (Correlation = 0.371, p-value = 1.77×10^{-5}) as seen in Table 4.4 and Figure 4.4. These results suggest that the quantity of WMSs act as a good indicator of star forming activity, intensity and evolution. However, this correlation is only considered when taking into account all clumps, and is not as strong when considering BM and WMO clumps individually.
- The flux of individual WMGs is found to be positively correlated with the Luminosity and L/M ratio of a clump (see Table 4.4). We therefore expect that more luminous masers tend to be associated with more luminous and evolved YSOs, however this correlation is not present for BM clumps or WMO clumps specifically.

- It was initially thought that more evolved clumps would have the potential to produce star forming regions further away from their centre than normal clumps. This is because they would have more time to agglomerate their ambient material at multiple locations, which might be at a great distance from the main centre of the clump. It turns out that there are no correlations between the water maser offsets (see Table 4.4) or the physical parameters of the clump, suggesting that they are not helpful at indicating clumps or SFRs with certain properties.

4.4 Discussion of Clump and Maser Properties

We will first recap our main findings from the analysis of the clump and maser properties. One of our main findings is that clumps with both water and methanol maser transitions have significantly higher luminosities, masses and L/M ratios than clumps showing only one of these transitions (see Figure 4.2). We do also find that the quantity of WMSs per clump generally holds a weak but positive correlation with the luminosity, L/M ratio and mass of a clump. However, this correlation is for the whole ATLASGAL sample and not specific to maser associated samples (MMO, BM and WMO).

We first consider why BM clumps would show higher luminosities and masses than WMO clumps. This could be because BM clumps host larger clusters, containing more YSOs and therefore would naturally have more natal mass. This increased abundance of material in the natal clouds would then have the potential to form more protostars, which in turn leads to increased luminosities of the cluster and the clump. The increase in protostars may also encourage competitive accretion, which forms MYSOs (Bonnell, 2005). These MYSOs would then also increase the luminosity of the cluster. Ultimately, the increased luminosity and mass suggest that BM clumps either contain younger but very luminous high-mass stars, or clusters of more numerous but more evolved stars.

We now introduce the result that shows the L/M ratios are significantly higher in

BM clumps than WMO / MMO clumps, since this parameter can be used as an indicator for how evolved a clump is (Molinari et al., 2008). The higher L/M ratios that we have observed would tend to suggest that we have more evolved YSOs rather than very luminous and younger MYSOs.

We can also test this by looking at the classifications provided in Urquhart et al. (2018) for these clumps, which should give us an idea about the specific evolutionary stages that we observe for BM and WMO clumps. Table 4.5 provides a list of these classifications and the percentages for BM and WMO clumps.

Table 4.5: The percentages of all classifications from ATLASGAL for BM and WMO clumps respectively. E.g $28.1 \pm 4.1\%$ of all BM clumps are classified as YSO-8micron bright. The errors are calculated using the poisson uncertainty.

Classification	BM / %	WMO / %
YSO-8micron bright	28.1 ± 4.1	28.7 ± 4.4
YSO-8micron dark	2.4 ± 1.2	9.3 ± 2.5
HII region (Radio)	25.1 ± 3.9	16.7 ± 3.3
HII region	16.2 ± 3.1	14.7 ± 3.1
Protostellar	7.8 ± 2.2	4.0 ± 1.6

Table 4.5 tells us that we generally observe more HII regions in BM clumps ($41.3 \pm 5\%$) than WMO clumps ($31.4 \pm 4.6\%$) when taking into account both the “HII region” and “HII region (Radio)” classifications. HII regions generally represent more evolved clumps, which provides evidence that BM clumps host more evolved protostellar objects than their WMO counterparts.

Further evidence for this is gathered when observing the differences between the “YSO” classifications. When taking into account the “YSO-8micron bright” and “YSO-8micron dark”, 30.5 ± 4.3 of BM clumps contain YSOs whereas $38 \pm 5\%$ of WMO clumps have YSOs. This suggests that BM clumps generally contain fewer YSOs than WMO clumps, however, the large uncertainties in our values mean this is not definitive. Since YSOs are younger and less evolved stars by definition, we

expect that BM clumps are likely to host more evolved objects. The larger L/M ratios and HII regions previously found in BM clumps supports this narrative.

The question is then, why do we observe more flavours of maser with more evolved YSOs?

It is well known that more evolved YSOs are generally more luminous, and more luminous stars radiate more power. We speculate that this increased energy output is more likely to shock a greater quantity of surrounding water molecules, which would then form masers. This hypothesis is supported by the fact that we observe a general positive correlation between the quantity of WMSs and the luminosity of the source.

We know that Class II 6.7 GHz methanol masers are exclusively associated with early high-mass star formation (Breen et al., 2013), which would then suggest that more evolved SFRs would be more likely to generate MYSOs. This could be the case, since a more evolved SFR would be more likely to form tight clusters of stars over time, which would encourage MSF. However, it could also be the case that BM clumps contain more intense star formation / embedded objects, which would also suggest a higher abundance of natal material to form tight clusters.

In order to test if we have more embedded objects, we conduct a visual inspection of all BM clumps and WMO clumps in the ATLASGAL survey that were classified as “HII region” or “HII region (Radio)” by creating multi-wavelength images. These are made using 4.6, 5.8 and 8.0 μm wavebands.

We choose one classification in order to compare the clumps fairly. HII regions allow us to look at active clumps, which will reveal the level of intensity of SF in BM clumps compared to WMO. Examples of these multi-wavelength images for four BM and WMO clumps are shown in Figures 4.5 and 4.6 respectively. These clumps were chosen to represent the typical BM / WMO clump with a HII region.

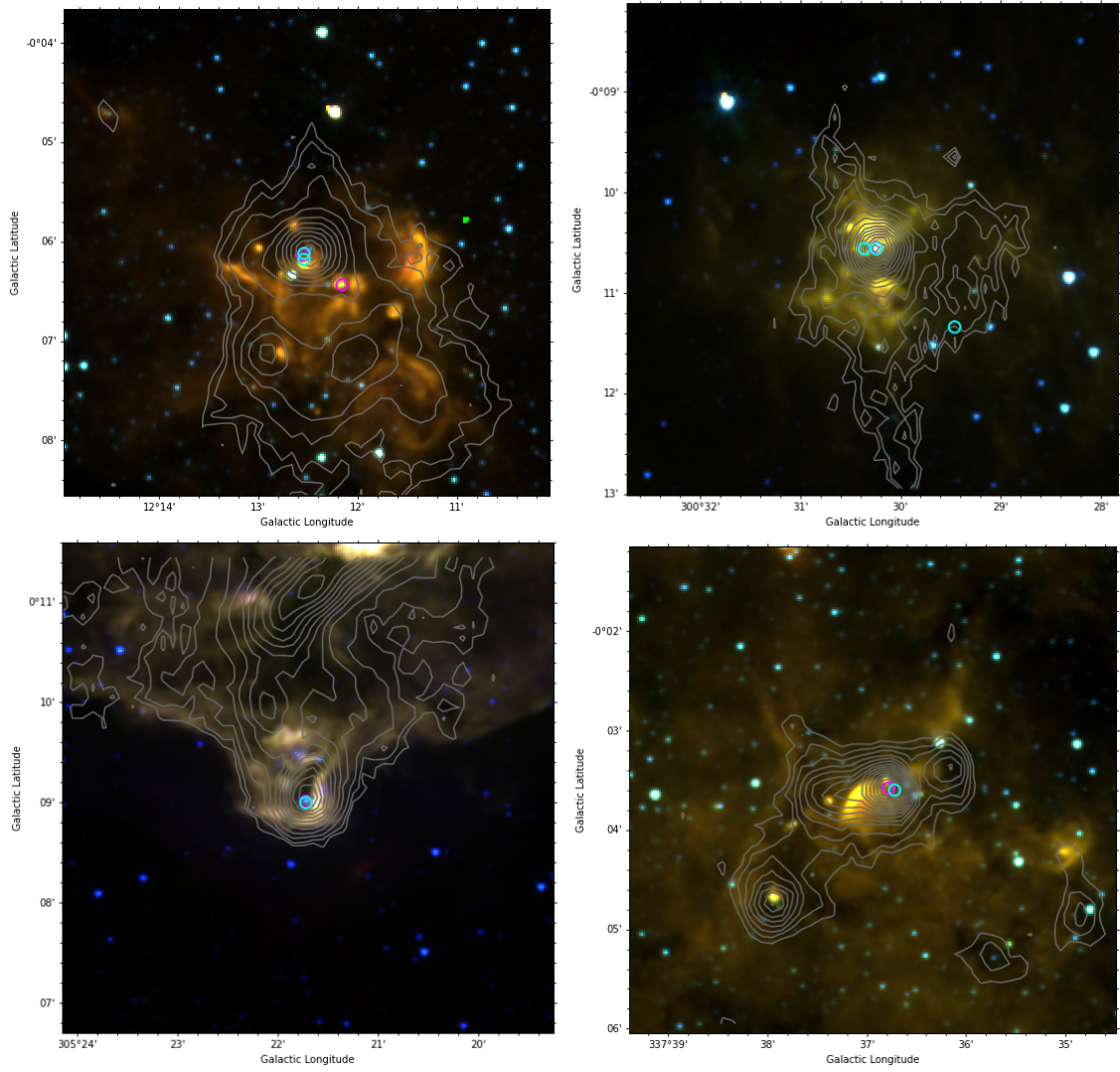


Figure 4.5: Four BM clumps represented with 4.6, 5.8 and 8.0 μm wavelengths in blue, green and red respectively. The clumps shown are AGAL012.208-00.102 (Top-Left), AGAL300.504-00.176 (Top-Right), AGAL305.362+00.151 (Bottom-Left), AGAL337.612-00.059 (Bottom-Right). The grey contours represent the sub millimetre emission from ATLASGAL. Methanol masers are represented by the purple circles, whereas water masers are represented with the cyan circles.

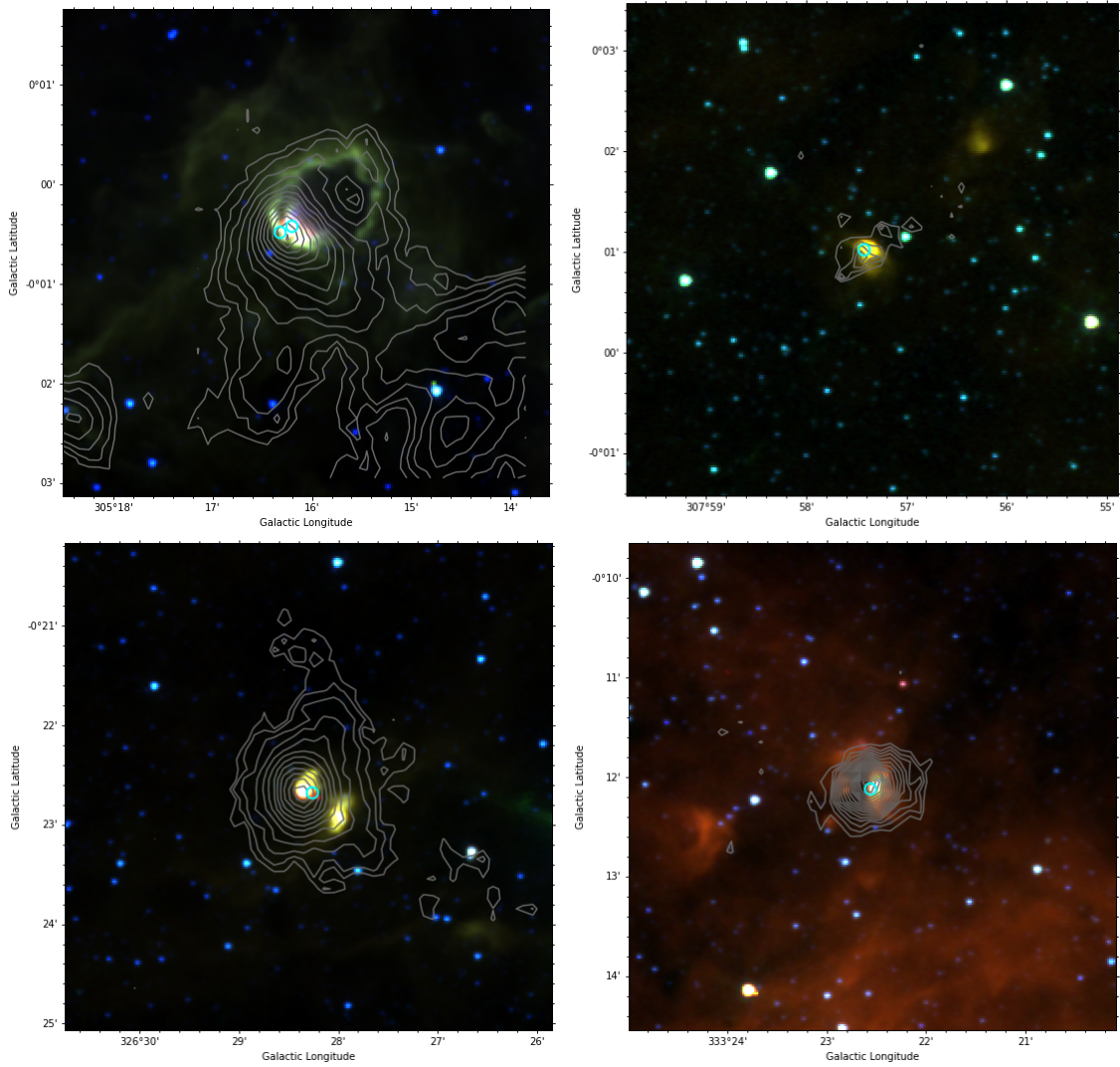


Figure 4.6: Four WMO clumps represented with 4.6, 5.8 and 8.0 μm wavelengths in blue, green and red respectively. The clumps shown are AGAL305.271-00.009 (Top-Left), AGAL307.957+00.016 (Top-Right), AGAL326.472-00.377 (Bottom-Left), AGAL333.376-00.201 (Bottom-Right). The grey contours represent the sub millimetre emission from ATLASGAL. Methanol masers are represented by the purple circles, whereas water masers are represented with the cyan circles.

We generally see that BM clumps have larger and more extended HII regions than their WMO counterparts, which is illustrated when comparing the clumps in Figures 4.5 and 4.6. We suggest that HII regions with more extended emission are also more evolved since they have had more time to expand and form a complex structure, which also makes them more likely to have triggered clusters in SFRs that generate

the water and methanol masers we observe. This provides evidence that BM clumps contain more evolved objects than WMO clumps.

We also find that BM clumps seem to show more intense SF by observing the abundance of $8\ \mu\text{m}$ emission in Figure 4.5 compared to Figure 4.6. This suggests they contain more embedded objects than WMO clumps. These embedded objects would then go on to form clusters of stars and MSF, which increases the likelihood of these clumps generating methanol masers.

Clumps with both CH_3OH and OH masers have also previously been found to host higher masses and luminosities (Olmi et al., 2014), which suggests that these results may hold true for other combinations of masers. If this is true, then using a combination of masers for targeted searches of more luminous and evolved clumps would be extremely useful, however this remains unproven.

Overall, we summarise that the differences found in the physical parameters between BM and WMO clumps is primarily down to the former hosting more evolved YSOs and embedded sources. These evolved YSOs and higher SF activity then both contribute to generating more flavours of masers.

4.5 Comparison of Results with “Straw Man” Model

The “straw man” model was developed by Ellingsen et al. (2007), in order to determine the evolutionary sequences for some of the most common astrophysical masers (22.2 GHz H_2O , 1.6 GHz OH , 95.1 GHz class I methanol and 6.7 GHz class II methanol). This was achieved by studying ongoing regions of SF that were surveyed for the previously mentioned masers and studying their associations.

The analysis of the studies for 22.2 GHz H_2O (Breen et al., 2007) 1.6 GHz OH (Caswell et al., 1980) and 6.7 GHz class II methanol masers (Ellingsen et al., 1996) led to the conclusion that the water masers seemed to trace an earlier evolutionary stage of SF than methanol masers. However, it was found by Billington et al. (2020) that water and methanol masers seemed to trace very similar evolutionary phases, which adds a layer of uncertainty to this model. Both of these models can be seen

in Figure 4.7.

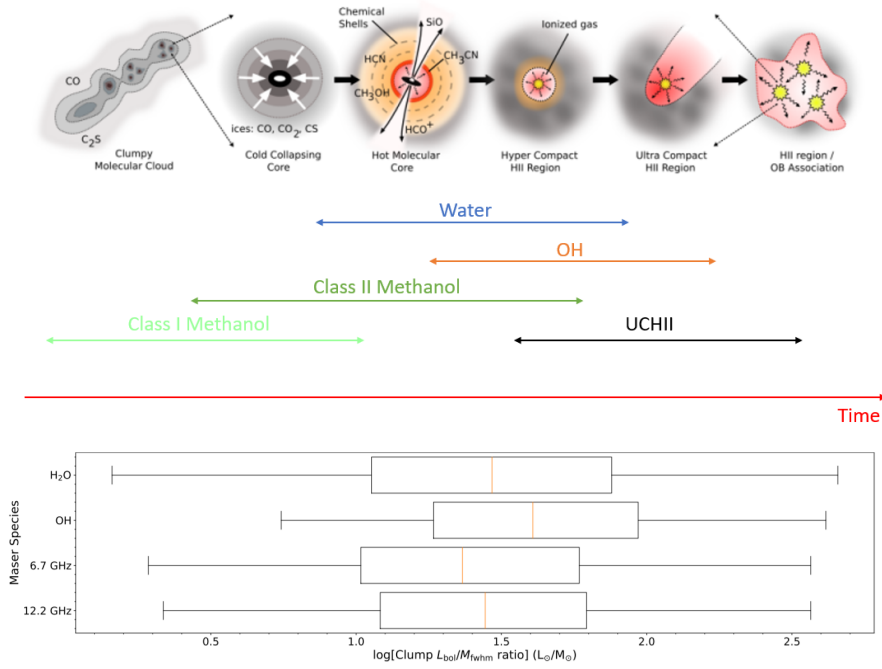


Figure 4.7: The top panel shows a brief outline of the evolutionary sequence of high-mass stars, along with the “straw man” model (Ellingsen et al., 2007) that shows the lifetimes of various maser species. Image Credit : Cormac Purcell. The bottom panel shows box plots of the L/M ratios for different maser species from (Billington et al., 2020)

Furthermore, our conclusions in this chapter also do not agree with the “straw man” model presented in Ellingsen et al. (2007), since we show that a clump containing a combination of maser lines are significantly more evolved than those with only one. This suggests that the evolutionary stages presented for different transitions of masers may not be entirely accurate, but we do not find the concrete solutions to this problem.

A basic diagram of what an updated “straw man” model may look like is presented in Figure 4.8. Methanol and water masers are shown to have similar evolutionary stages by our results and Billington et al. (2020). They are also found to exhibit similar statistical lifetimes, which is a measure of how long these maser species are active for. OH masers are shown to represent a slightly later evolutionary stage from

methanol and water masers, but it is not significant (Billington et al., 2020; Ellingsen et al., 2007). When these masers are combined, we have shown that they represent a significantly later stage of evolution. This is because they are more probable to be active at the same time when there are more evolved YSOs and embedded sources. Therefore, they represent a more evolved star forming environment than any other maser association in the current “straw man” model.

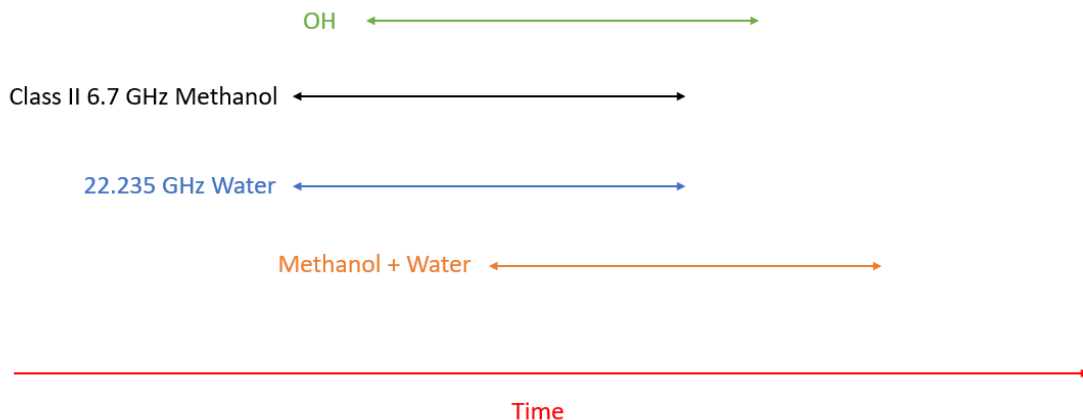


Figure 4.8: A basic model of the evolutionary sequence of OH masers, 22.235 GHz H₂O masers, Class II 6.7 GHz methanol masers, as well as a combination of both water and methanol masers.

4.6 Summary

The initial goal of this chapter was to build on the results found in Billington et al. (2020) by comparing the maser and clump properties of clumps containing a combination of maser lines with those that are only associated with single maser lines. These clumps were classified as BM, WMO and MMO clumps, which were based on what species of masers they contained.

We do find that WMO and MMO clumps exhibit similar physical parameters, which is in agreement with Billington et al. (2020). However, we were also able to conclude that clumps with 22.235 GHz H₂O masers and Class II 6.7 GHz methanol masers are more evolved, more massive and more luminous than clumps showing emission of only one of these maser species. We find that these differences in the physical

parameters of BM and WMO clumps are primarily due to BM clumps hosting more evolved YSO's, embedded sources and more active SF. The existence of more evolved YSOs will increase the luminosity and the L/M ratio, since they are further through their accretion process and will radiate much more power (Molinari et al., 2008). More embedded sources suggests that there is a higher abundance of natal material for clusters to form, which encourage MSF through competitive accretion.

We then sought out to investigate why more evolved YSOs and embedded sources would be more likely to show both water and methanol masers. We know that these more luminous and evolved protostellar objects emit stronger radiation, so we speculate that they are more likely to provide a pumping mechanism to surrounding water molecules, hence more likely to generate more water masers. This hypothesis is also supported by the fact that we observe a general positive correlation between the number of WMSs and the luminosity of the source. Additionally, more embedded sources would be more likely to lead to MSF because they suggest that a higher abundance of natal material is present in these SF regions. The increased volume of material would then be more likely to form clusters of stars, which would also be likely to form MYSOs. Since Class II 6.7 GHz methanol masers are exclusively associated with MSF (Breen et al., 2013), we would expect their numbers to rise as well.

We also suggest that the “straw man” model developed by Ellingsen et al. (2007) may not describe the evolutionary sequence of masers accurately, since we demonstrate that including a combination of just two maser species will drastically change the L/M ratio (hence evolution) of the SF region associated with those masers. This is however, a complex problem, and we do not provide any concrete improvements to the model in this work other than a basic sketch of what a more accurate model may look like (see Figure 4.8).

Overall, our conclusions provide evidence that a combination of just two maser species could be used to target more massive, luminous and evolved clumps. These clumps will also yield observations of more evolved YSOs that can help us better understand the internal environments of these regions and the early stages of

MYSOs.

Chapter 5

Identifying Interesting Sources - Offsets

The aim of this chapter is to identify sources that are not similar to the general population of sources that we observe. This is achieved by investigating the offsets of water and methanol masers.

One of the first tasks of this chapter will be to identify all 22.235 GHz H₂O masers and Class II 6.7 GHz methanol masers that are significantly offset from the centre of their clump, as defined by the peak submillimetre emission from ATLASGAL. Both water and methanol masers tend to be located close to the centre of the clump since this is where the majority of the material and star formation is situated ([Urquhart et al., 2014b](#)). Therefore, searching for clumps that host masers with unusually high offsets from the centre of clumps will provide a method of discovering interesting clumps, external environments affecting star formation and possibly new phenomena previously unknown to be linked with masers that are able to generate them at such large offsets.

We will again investigate clumps with both types of masers. This is because we want to pinpoint the location of MSF in the clump with the use of the methanol maser emission, as well as to investigate the water maser emission since it can be associated with a variety of astrophysical processes/objects ([Walsh et al., 2014](#)).

We again use MIR images to investigate the nature of interesting sources identified, this will help with identifying external environments and structures associated with high-mass star formation such as HII regions. These images can then be used to classify clumps based on the morphology of masers and the structures we see in the infrared emission.

By the end of this chapter, we will determine if there is any significant advantage by searching for clumps in this manner. The usefulness of this method will be measured depending on whether it returns a common classification of clumps or a few interesting sources where the large offset of masers are not so easily explained.

5.1 Angular offsets

One of the goals of this project is to identify whether external environments on the edges of clumps are having a profound effect on high-mass star forming regions. As discussed in the introduction, masers act as signposts for various astronomical activities, many of which would be classified as external factors that could affect high-mass star forming regions. These include, but are not limited to; cloud collisions (Tarter and Welch, 1986), supernovae remnants (Woodall and Gray, 2007), HII regions (Fontani et al., 2010) and molecular outflows (Titmarsh et al., 2014). The HOPS survey was used to retrieve the positions of the 22.235 GHz H₂O masers that are associated with these activities. The MMB survey gives the positions of the class II 6.7 GHz methanol masers that pinpoint where high-mass stars are being formed.

Using the ATLASGAL catalogue (Urquhart et al., 2018), it is possible to identify the centre of these clumps using the peak intensity of the 870 μ m wavelength data. Therefore, the angular separation from the centre of the clump can be derived for every methanol and water maser within the MMB and HOPS survey respectively, this is commonly referred to as the angular offset (measured in arcseconds).

We first identified water masers that are significantly offset from the centre of the associated clump. This can be determined by using the previously mentioned angular offset parameter. We also need to define what a “significant offset” constitutes

as with respect to the rest of the data. We know that the angular offset data should follow a Gaussian-like distribution because we expect to see the majority of masers at an angular offset of zero, and we expect the number of masers that we observe to decrease rapidly at higher angular offsets. As one looks further away from the centre of the clump there will be less abundance of material and as a result less observed masers, whereas the centre of the clump contains the highest abundance of gas and star formation activity, which are conditions that are more likely to produce masers. For this reason, we will introduce a 3σ limit for both water and methanol masers separately in order to determine which masers are classified as significantly offset in each case. A property of a Gaussian distribution is that 99.7% of the data is contained within a range of 3σ from the mean, masers with larger offsets are therefore unusual and flagged for further investigation.

The top panel of Figure 5.1 is the result of plotting all angular offsets for water masers and methanol masers, however this is not quite in the format of a Gaussian distribution. Therefore, we use a surface density plot to account for the area of the annulus that the masers are located in. This results in the 2-D Gaussian Distribution observed in the bottom panel of Figure 5.1.

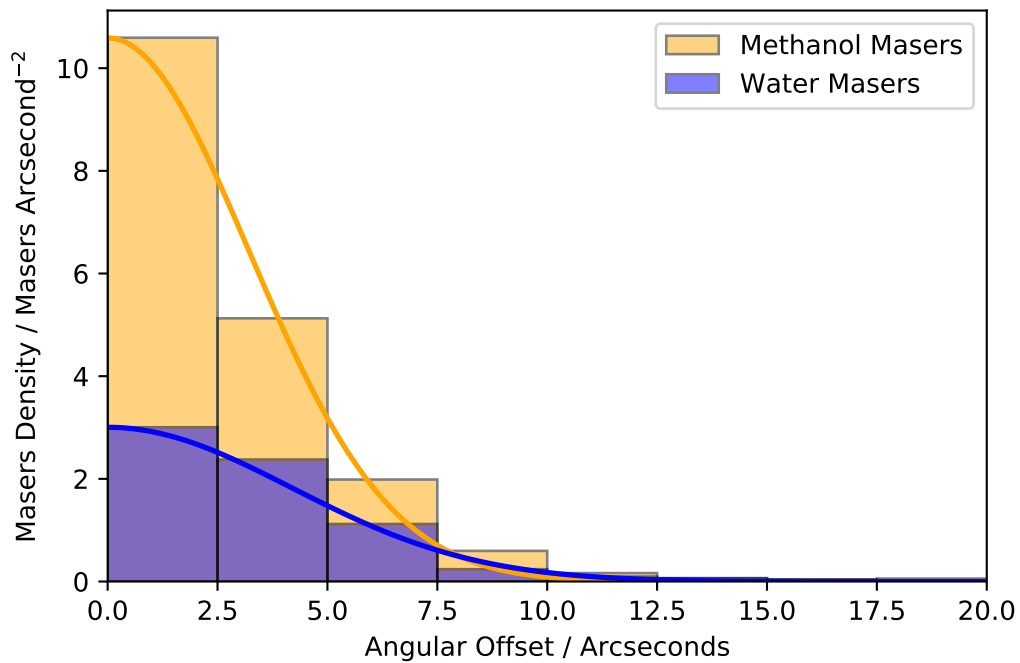
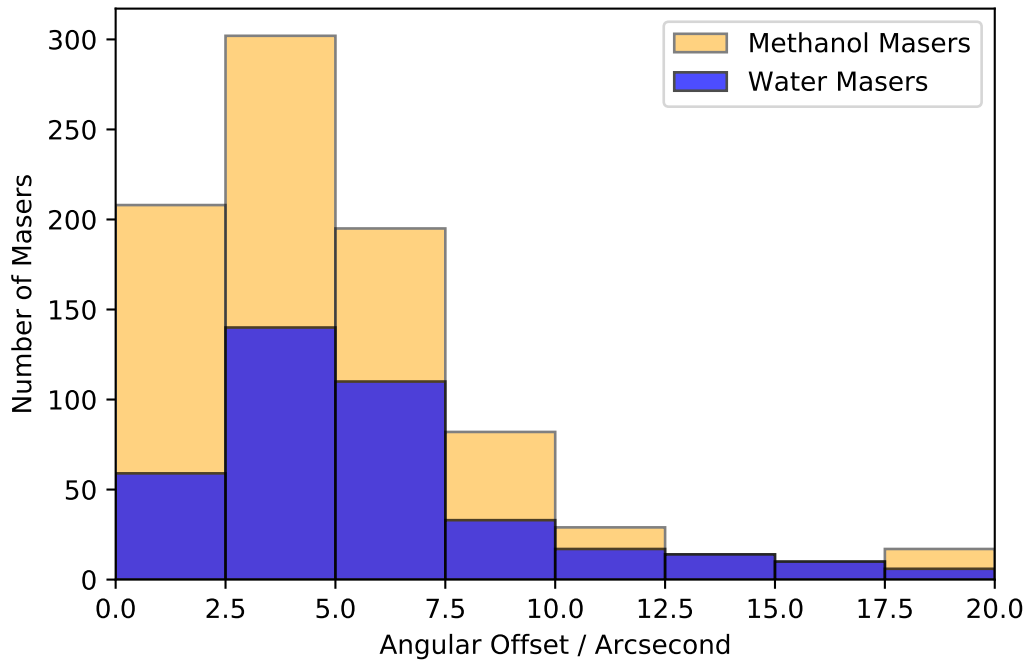


Figure 5.1: The top panel shows all angular offsets for every maser associated with a clump. The bottom panel shows the maser density for ring regions at varying distances from the centre of a clump. The methanol and water maser density have been plotted separately, along with a fitted normal distribution curve. Both graphs show angular offsets between 0 and 20'' and have a bin width of 2.5''.

The 3σ limit for the methanol and water masers are calculated to be $24.2''$ and $31.5''$ respectively. If a clump contains at least one flagged maser, then that clump will be considered unusual and be investigated further.

This initial search results in a list of 64 methanol masers and 30 water masers considered to be significantly offset from the centre of their respective clumps. However, we also want to remove any distance bias from our sample. We achieve this by using a distance limited sample, where we only include masers situated in clumps that are between a distance of 2-4 kpc. This leaves us with 12 22.235 GHz H₂O masers and 19 Class II 6.7 GHz methanol masers for further investigation.

5.2 Velocity Checks

Velocity checks are used in conjunction with the multi-wavelength images to decide if particular masers are actually associated with their clump. This is important because some masers may have been detected in line with ATLASGAL clumps in the 2D plane but might be in the foreground instead of in the clump itself, which would lead to an incorrect association. The purpose of this section is to discover these incorrect associations and rule them out of our analysis.

It is reasonable to assume that if a maser is associated with a molecular clump, then it should have a similar velocity when moving through space. Since the velocities for the majority of masers and clumps are given from the HOPS, MMB and ATLASGAL surveys, it allows for a side-by-side comparison of the clump velocity and maser velocity. We can then take the “velocity offset” of a maser to be the difference between the maser velocity and clump velocity.

By taking the 3σ limits of the velocity offsets for all water and methanol masers, we can then define an “unassociated maser” as one whose velocity offset is above their respective 3σ limit. These limits are calculated to be 17.1 and 12.3 km/s for water and methanol masers, respectively, from the Gaussian distribution functions plotted in Figure 5.2. A clump will be eliminated from the search if all significantly offset masers are identified to be unassociated with the host clump.

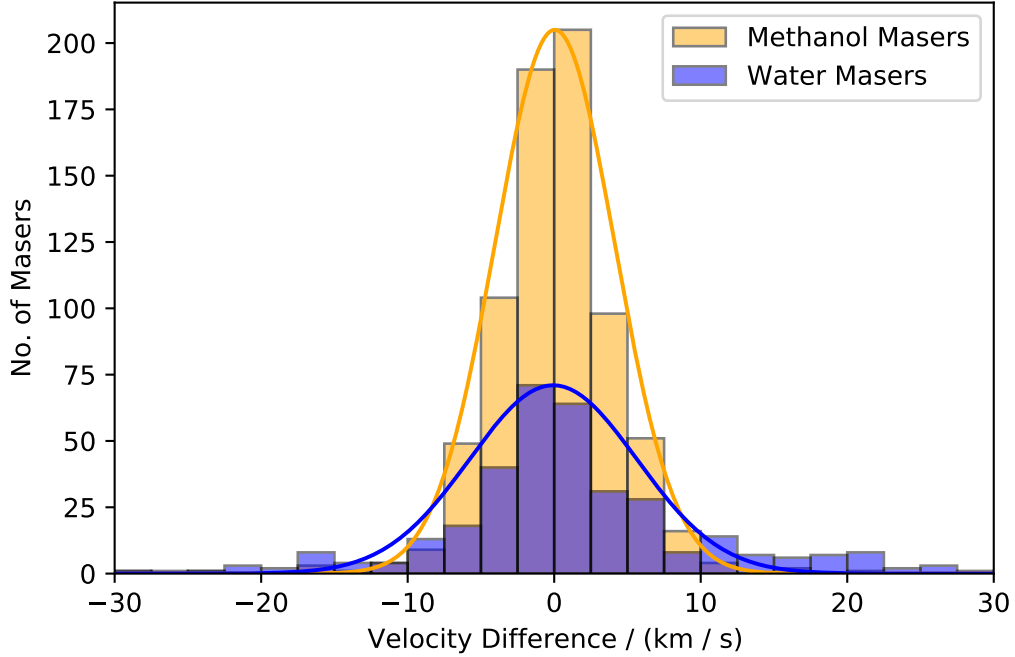


Figure 5.2: The distribution of velocity offsets for water and methanol masers respectively. A Gaussian curve has been fitted for each distribution to calculate the 3σ limit. The limits are 17.1 and 12.3 km/s for water and methanol masers, respectively.

As a side note, there could be some incorrect assumptions here, since 22.235 GHz H_2O masers are commonly generated by bipolar outflows, which affect the velocity of the maser. This means that some water masers in very high velocity outflows may be incorrectly assumed to not be associated with their clump. However, since this 3σ limit is relative to the whole population of water masers, the ones that are affected by bipolar outflows should be mostly accounted for.

These velocity checks are carried out in conjunction with observations of the multi-wavelength images, in order to ensure that the masers are definitely unassociated from the clump via visual inspection. For example, a maser that lies within 5 km/s outside of the 3σ velocity offset limits might be in the molecular cloud, but moving unusually fast due to outflows from stars or some other phenomena.

Table 5.1 shows all of the unassociated water masers.

Table 5.1: Water masers with a velocity difference more than 17.1 km/s different than their respective clump. The distance offsets of the masers (measured in pc) are shown in the brackets next to the angular offsets.

Clump Name	WMG Angular Offset (")	Clump Velocity (km/s)	WMG Velocity (km/s)
AGAL025.351-00.191	49.8 (0.64)	61.50	20.80
AGAL332.352-00.116	119.3 (1.79)	-49.80	-103.48
AGAL335.061-00.427	36.8 (0.52)	-38.40	-90.60
AGAL339.623-00.122	36.5 (0.47)	-34.20	-70.80

Table 5.1 provides an overview of all the masers in our initial list of 29 that have a velocity difference of more than the 3σ limit compared to its respective clump.

Overall, 4 water masers are dropped by using velocity checks whereas all the methanol masers passed, which is why they have not been discussed. The only methanol masers that are uncertain with velocity checks are those where the velocity of the clump is unknown. In these cases there is no reason to doubt their associations are genuine and so they will remain included.

Additionally, we find one methanol maser that is not associated with its host clump via visual inspection. This is because it lies outside of the 870 μm contours from ATLASGAL. Therefore, we are now left with 24 masers in a distance limited sample (16 methanol and 8 water), where we can be sure that all of their associations to their respective clumps are genuine.

5.3 Grouping Masers into Clumps

Now that we have our list of 16 methanol and 8 water masers, we can start to categorise these masers by the type of maser associated clump they appear in. We will group these masers into clumps containing 22.235 GHz H₂O masers and Class II 6.7 GHz methanol masers (BM clumps), clumps containing water masers only (WMO clumps) and clumps containing methanol masers only (MMO clumps), as

we did in the previous chapter.

We group these into BM clumps, since we obtain information about the location of possible external environments from the water masers and the location of high-mass star formation from the methanol masers, as a result of Class II 6.7 GHz methanol masers being exclusively associated with MYSOs (Walsh et al., 2014).

There is also no reason why WMO clumps should not be checked, especially because water masers are more likely to be offset from the centre of the clump than methanol masers. Therefore WMO clumps are included in the search in the same manner as the BM clumps.

Methanol masers are more likely to be situated close to the centre of the clump than water masers. This is because they are exclusively associated with MYSOs (Breen et al., 2013), and MYSOs are much more likely to form in the centre of the clump where there is a higher abundance of material and column density (Urquhart et al., 2014b). This means that methanol masers with large offsets are very unusual, so we also group by MMO clumps for this reason.

We find that the 24 significantly offset masers can be distributed into 8 unique BM clumps, 3 WMO clumps and 9 MMO clumps. This results in a total sample of 20 clumps that contain at least one significantly offset methanol or water maser. We will name this group of clumps the “Large offset” sample (LO sample).

5.4 Classification and Discussion

We now want to ascertain the nature of these masers as they may be linked to secondary star formation within the clump, external environments or stellar feedback from young, evolved stars. For this reason, we will apply a basic classification scheme to the list of 20 interesting clumps that we have attained so far (see Table 5.2).

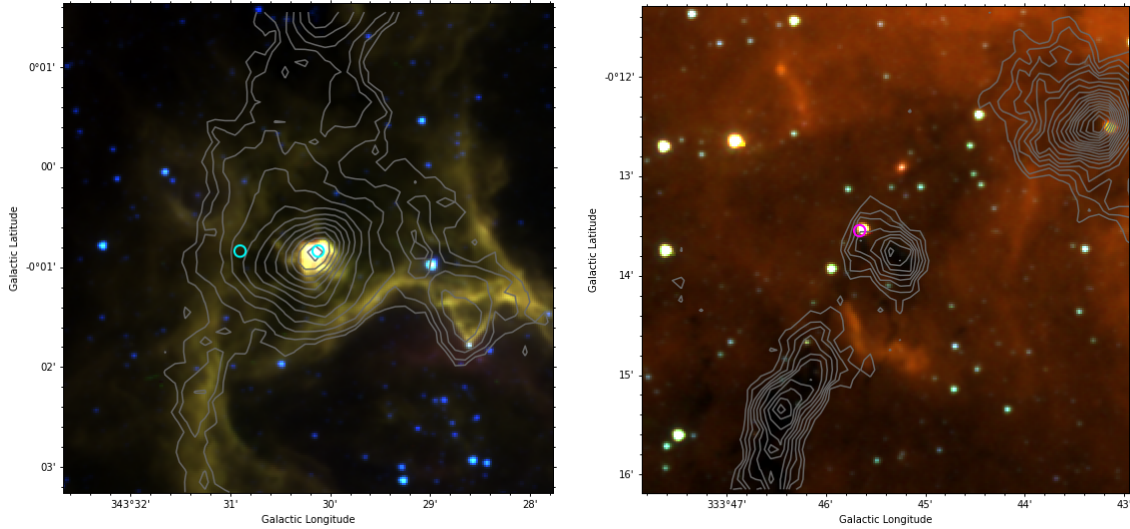
After this we will provide some examples of the multi-wavelength images of the LO sample, which will allow for a visual inspection of the clump and the features of each classification.

Table 5.2: The classification of all clumps that are considered interesting. All WMO clumps are represented by *, all MMO clumps are represented by **, the rest are BM clumps that do not have a * next to their names.

Clump Name	Classification
AGAL005.509-00.246*	Edge
AGAL332.317+00.177*	Unknown Association / Edge
AGAL343.502-00.014*	PDR
AGAL004.384+00.079**	PDR
AGAL004.887-00.171**	Localised Clump
AGAL006.551-00.097**	PDR
AGAL015.029-00.669**	PDR
AGAL016.662-00.342**	Localised Clump
AGAL025.412-00.174**	Unknown Association / Edge
AGAL332.647-00.609**	PDR
AGAL333.754-00.229**	Edge
AGAL340.536-00.152**	Unknown Association / Edge
AGAL305.209+00.206	PDR
AGAL329.029-00.206	Localised Clump
AGAL333.121-00.432	Localised Clump / PDR
AGAL333.134-00.431	Localised Clump / PDR
AGAL338.391+00.172	Localised Clump
AGAL341.126-00.347	Unknown Association
AGAL345.443+00.212	Localised Clump / PDR
AGAL345.504+00.347	Localised Clump / PDR

The next few paragraphs will aim to explain the several classifications used in Table 5.2 and how this relates to the features of a clump.

5.4.1 Edge



(a) AGAL343.502-00.014

(b) AGAL016.662-00.342

Figure 5.3: Three colour images for two edge clumps where both images are made with 4.6, 5.8 and 8.0 μm emission represented by blue, green and red respectively. It should be noted that every multi-wavelength image for the rest of the thesis will have the following in common; 1) The cyan circles will represent 22.235 GHz H_2O masers and the purple circles will represent Class II 6.7 GHz methanol masers 2) The grey contours will always show the 870 μm emission from ATLASGAL.

“Edge” type clumps refer to clumps that have masers residing near the edge of the contour lines of a source. From the LO sample, we observe that both water and methanol masers are just as likely as each other to appear on the edges of a clump. The astrophysical features that lead to masers being generated on the edge of clumps vary. Figure 5.3a shows an example of an edge clump where the water maser appears to be on a boundary of the HII front. Figure 5.3b represents an edge clump where the cause of the methanol maser appears to be a strong peak of MIR emission, most likely an evolved star.

5.4.2 Photodissociation regions

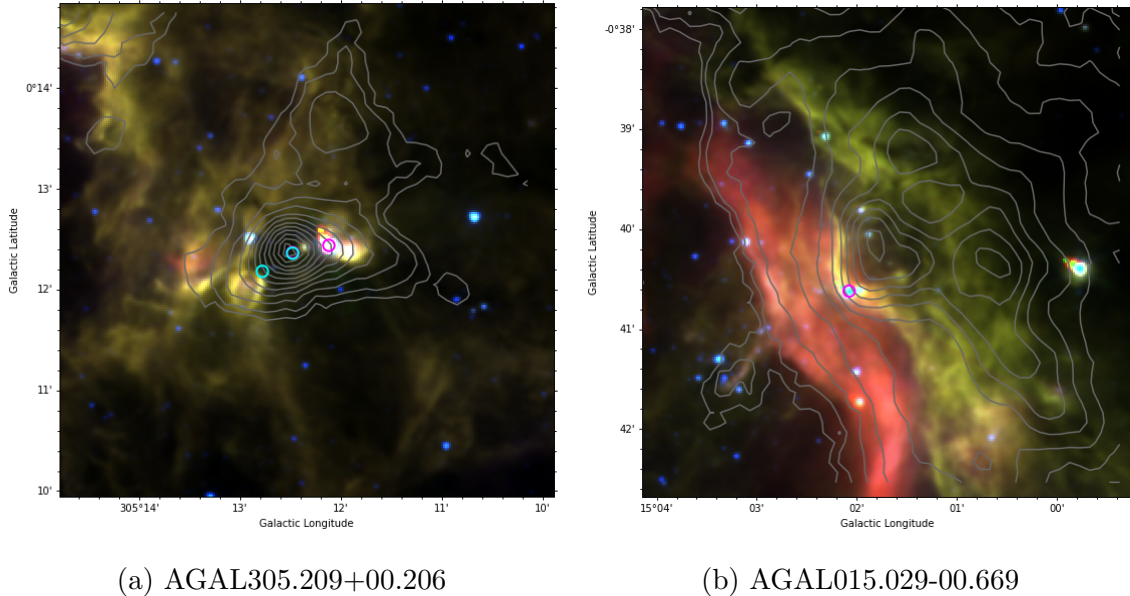


Figure 5.4: Three colour images for two clumps showing examples of a PDR being associated with a maser.. These images show 4.6, 5.8 and 8.0 μm emission represented by blue, green and red, respectively. (See Figure 5.3 for more details).

Photodissociation regions (PDRs) are regions of space in which the heating of the gas of the neutral ISM is controlled by far-ultraviolet photons (6 eV - 13.6 eV) (Hollenbach and Tielens, 1999). This can be seen at the boundary of the HII regions and the ISM, these are particularly bright regions and usually show stronger emission than the rest of the HII regions. We classify a clump as “PDR” when a maser is incident on its boundary, likely being shock excited. Methanol masers are exclusively associated with SF (Breen et al., 2013), so when we see them on a HII boundary it is highly suggestive that the PDR is triggering SF in that region.

Figure 5.4a provides an example of a clump containing two PDRs. The edge of the western HII region (at the location of the water maser) is brighter than the rest of the structure, which is indicative of a PDR. The other PDR is a bright HII region on the eastern side of the clump’s centre, which is driving a methanol maser. Figure 5.4b provides an example of a PDR driving a methanol maser, which is evidence of triggered SF.

5.4.3 Localised clumps

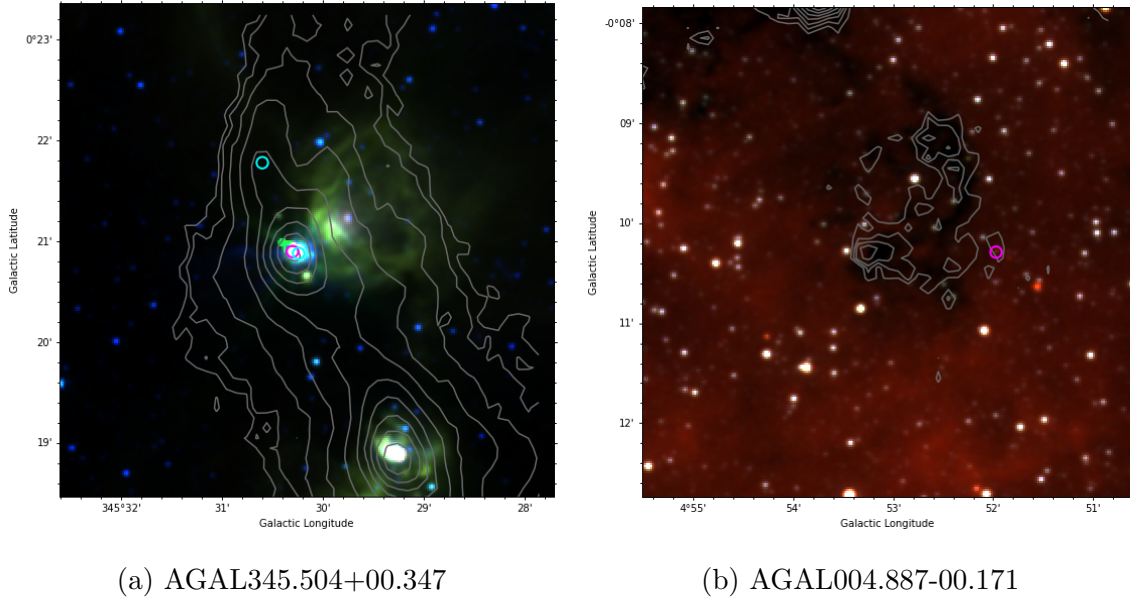


Figure 5.5: Three colour images for two clumps showing examples of localised clumps. These images show 4.6, 5.8 and 8.0 μm emission represented by blue, green and red, respectively. (See Figure 5.3 for more details).

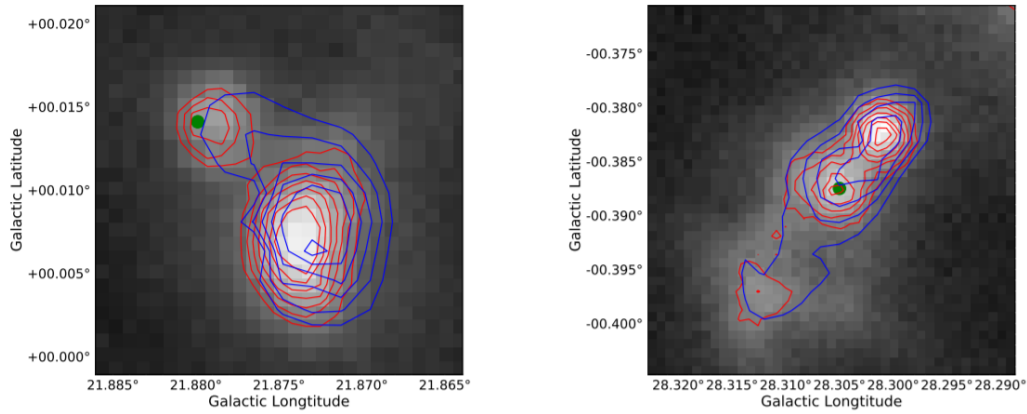


Figure 5.6: Two images showing JPS 850 μm emission from AGAL021.873+00.007 and AGAL028.301-00.382 in the left and right panels, respectively. The red and blue contours represent the JPS and ATLASGAL tracing, respectively. It can be seen that the JPS contours more accurately trace the structure of the clump to include the smaller, localised peaks. (Billington et al., 2019).

Localised clumps are smaller, less powerful clumps that usually surround the primary centre of the source that have not been detected by ATLASGAL (Urquhart et al., 2018). These localised peaks of 870 μm emission were studied by Billington et al. (2019), where it was found that some ATLASGAL clumps could be split into multiple separate clumps by using the higher resolution of the 850 μm emission from the JPS survey (Moore et al., 2015) (see Figure 5.6).

Localised clumps can be located at a relatively large distance from the main centre of the clump detected by ATLASGAL, and they can also be powerful and active enough to host masers. Localised clumps can have very weak 870 μm emission, and so they might not be able to form concentric rings of contours. Instead, there may only be a slight curve in the contour lines combined with the presence of a maser that can be used to identify them. This effect is seen in Figure 5.5a, where the contours can be seen to bend sharply around the northernmost water maser, but not forming a ring. We also see an example of a methanol maser being generated by a localised clump in Figure 5.5b, where the substructure has accumulated enough mass to start forming MYSOs.

5.4.4 Unknown association

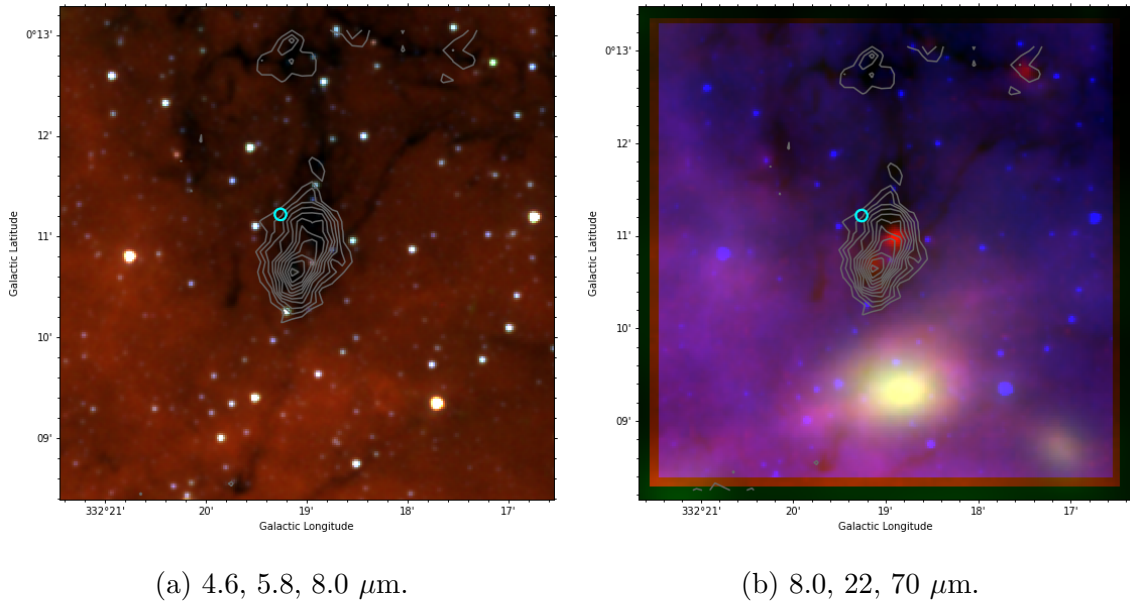


Figure 5.7: Three colour images for AGAL012.208-00.102. The left panel shows 4.6, 5.8 and 8.0 μm emission represented by blue, green and red respectively. The right panel shows 8.0, 22 and 70 μm emission represented by blue, green and red, respectively. See Figure 5.3 for more details.

Unknown association is a label given to clumps that contain one or more masers that have no clear association with any wavelength emission or structures. Figure 5.7 provides such an example, where it can clearly be seen that the water maser in this clump has no near, mid or far-infrared association. This makes it very difficult to determine the nature of these masers.

We also identify some methanol masers as an unknown association, even though we know they are exclusively associated with young high-mass stars (Breen et al., 2013). This is because in some cases, it is unclear as to what is driving the MSF.

5.5 Discussion

So far, we have found and classified 20 clumps that host at least one significantly offset maser from the centre of the clump. Our initial goal of this chapter was to

Breakdown of Classifications

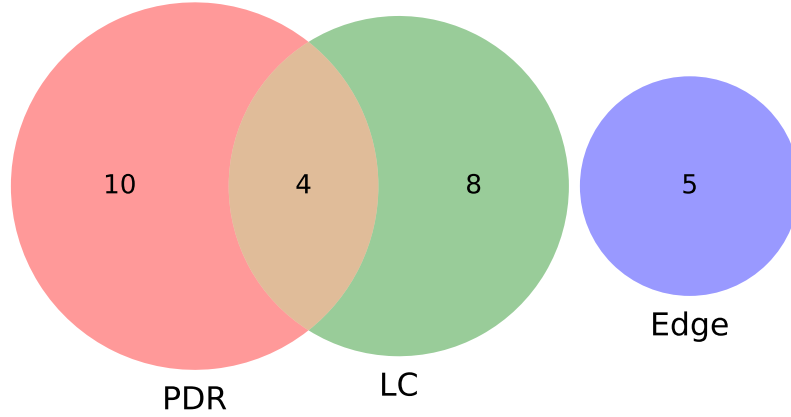


Figure 5.8: A breakdown of how many clumps fit into the classifications of PDR, LC (Localised Clump) and Edge, as well as their overlaps.

determine if this method of searching for clumps returned any common astrophysical features, external environments affecting SF or any interesting sources in general. If our investigation yields any of the aforementioned results, we will confirm the validity of using this method to search for clumps in the future.

We will first look at the most common classifications of the LO sample from Table 5.2. We find that PDR clumps are the most common classification at 50%, followed by localised clumps at 40% , “edge” clumps at 25% and masers with an unknown association at 20% (see Figure 5.8). Additionally, we find that localised clumps are more heavily associated with BM clumps in our sample (75% of BM clumps contain localised clumps) and very few BM clumps have examples of masers lying close to the edge of their 870 μm contours.

The most common astrophysical feature that we observe in the LO sample is the PDR at 50%. We find that only 1 out of the 10 PDR clumps (AGAL305.209+00.206) show signs of the HII region acting as an external factor that sweeps through the

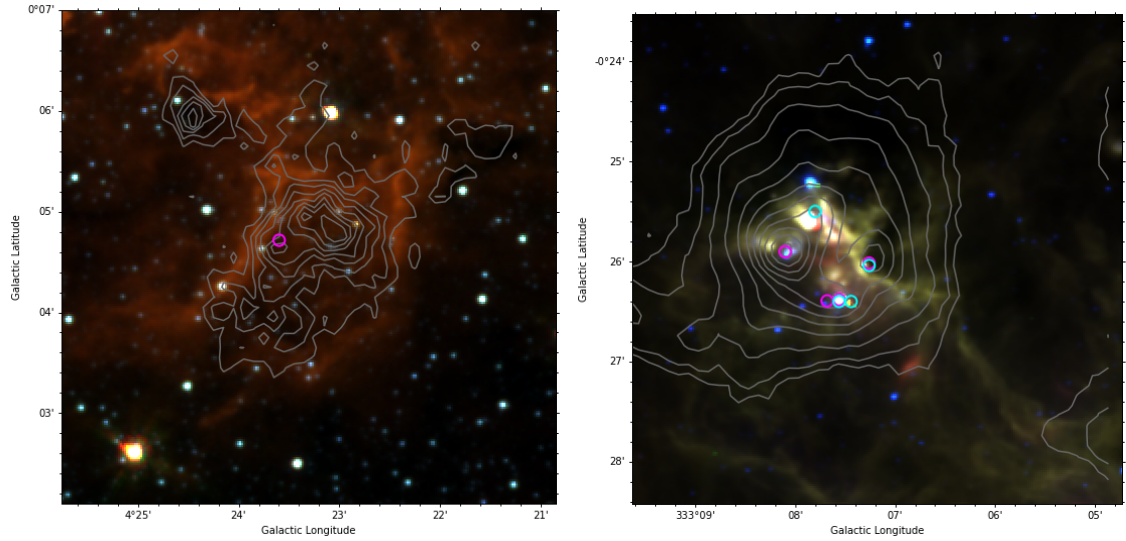


Figure 5.9: Three colour images for AGAL004.384+00.079 and AGAL333.121–00.432 in the left and right panels, respectively. All images are made with 4.6, 5.8 and 8.0 μm emission represented by blue, green and red respectively. See Figure 5.3 for more details.

clump, triggering star formation and water masers along its boundary. However, in the majority of cases the HII region seems to originate from within the clump, where it acts as more of an internal factor. Figure 5.4 shows an example of an external HII region, whereas Figure 5.9 shows two examples of an internal HII region. Overall, the HII regions do not act as external environments for the LO sample, and we do not find any other astrophysical features that could act as an external environment other than HII regions. We therefore conclude that searching for masers at high offsets do not provide good examples of external environments affecting internal SF activity.

We also know that these HII regions are large, which is why they can sustain masers at such large offsets. Large HII regions are known to sweep up more mass than they ionise, which leads to cloud disruption (McKee and Ostriker, 2007; Williams and McKee, 1997). In fact, many of these HII regions may act as blister HII regions (Zuckerman, 1973), which form at the edge of the clump and lead to the eventual destruction of the GMC. This implies that masers with large offsets that are associated with a PDR may be situated in a clump that is on the verge of self destruction.

Localised clumps are found to be more heavily associated with BM clumps in the LO sample, suggesting that localised clumps are more likely to arise in BM clumps. We speculate that this is a consequence of BM clumps being more evolved than WMO or MMO clumps, which is a result we have already concluded in Chapter 4. The later evolution of the clump means that it has had more time to agglomerate material in multiple locations and form more complex structures. We can also say that these localised clumps are not likely to produce masers, since we would expect to see a significant difference in maser offsets between BM and WMO / MMO clumps, which we do not (see Chapter 4).

We also find four “Unknown Association” sources. This is where the masers are likely confirmed to be associated with the clumps, but the physical processes driving their existence are unknown to us with the mid-IR wavelengths we have used. They seem to have a large overlap with edge clumps (3 of the 4 unknown associations are at the edge of a clump), which suggests there may be a physical process occurring only at the edge of the source that radiates enough energy to pump these masers.

All of these unknown associations at the edges are water masers, which opens the idea that there may be outflows from stars that are not visible at the mid-IR, which shock these masers. AGAL341.126-00.347 identifies a methanol maser and water maser that has no clear mid-IR counterpart, which may be attributed to very young and massive protostellar objects that do not emit at these wavelengths.

Overall the LO sample was partially successful, since we now know the nature of these large offset masers to be unresolved substructures of ATLASGAL clumps that we label “localised clumps”. This highlights the need for higher resolution and more sensitive sub mm surveys so we can eliminate these pseudo high offset masers. It may also be useful to repeat a similar search for future surveys in order to confirm or deny the “Unknown Associations” with masers on the edge of clumps to be significant. However, this search was unsuccessful in terms of identifying external features that may be driving SF.

5.6 Summary

We have identified 20 clumps where the masers within the clump appear to be significantly offset from the peak sub mm emission from ATLASGAL (Urquhart et al., 2018). We have looked at multi-wavelength images in the mid and far-IR to ascertain the nature of these unusual masers, and to determine whether this search yielded useful results and could be repeated.

We find that the LO sample was successful at identifying common features that may be driving these significantly offset masers. The majority of these masers are a result of either; 1) HII regions shocking 22.235 GHz H₂O masers along their boundary 2) Localised clumps that have enough material to encourage SF from which young protostellar objects will generate masers. Since these HII regions are also large, we expect that they are at a closer stage to causing cloud disruption and the eventual destruction of a GMC (McKee and Ostriker, 2007; Williams and McKee, 1997).

However, we find that the LO sample is unsuccessful at identifying external environments driving SF. The only observed external environments were the fronts of HII regions sweeping across the clump and triggering star formation at the centre of the clump, whilst also shocking 22.235 GHz H₂O masers at locations far away from the centre of the clump. However, this only occurred for 1 out of the 10 clumps classified as containing a PDR that is likely triggering a maser.

The LO sample has identified some interesting sources. In particular, we find the “unknown association” clumps to perhaps be the most interesting of all sources, because they contain significantly offset masers with seemingly no mid-IR counterpart. They also seem to largely occur in edge clumps, which suggests that a rare, physical process energetic enough to pump water masers may exist at the edge of clumps. However, our sample size may be too small to confirm this.

Overall, we find that searching for masers with significantly high offsets from the sub mm peak could reveal more of these unknown associations that we observe at the edge of clumps and is therefore useful for this purpose. It may also be used to search for masers that are being shocked by a PDR and blister HII regions

([Zuckerman, 1973](#)), since we identify this as a common feature throughout the LO sample. However, we suggest that it not be used to search for external environments impacting SF, since the cause for the majority of these unusual masers are primarily from internal processes.

Chapter 6

Identifying Interesting Sources - Water Maser Spots / Groups

6.1 Introduction

In the previous chapter, the criterion used to determine interesting clumps was by large maser offsets. This was done to investigate the possibility that this would identify clumps that were being externally affected by shocks from ionisation fronts or compression waves. However, there were not many examples of external factors outside of large HII regions that could be attributed to significantly affecting the star formation in the centre of the clump.

In the same way that we selected clumps based on their large maser offsets in the previous chapter, we can also select sources with an unusually high quantity of WMSs. This builds on the results of Chapter 4, where it was shown that the quantity of WMSs is positively correlated with the clump's luminosity and L/M ratio, therefore we will effectively be searching for brighter and more evolved clumps. These brighter clumps should also denote more active clumps, since there will be more embedded and more powerful protostellar objects. As a side note, we do not perform this analysis with methanol masers, since their groups have not been resolved into individual maser spots, therefore there are too few data points to say

anything concrete about them.

We will also select clumps that host WMGs with an unusually large quantity of WMSs. This should give us an indication of the localised star formation activity. For example, if a WMG hosts a significant number of spots compared to any other that we observe, it is likely to have an intense and concentrated level of star forming activity around that region, perhaps pertaining to tight groups of protostellar objects or indicating the presence of a powerful embedded object.

We will then create composite images for the 4.6, 5.8 & 8.0 μm as well as 8.0, 22 & 70 μm wavelengths and present our findings on the final sample. Afterwards, we conclude if this method of searching for these abundant WMS sources yields us clumps with more intense star formation, and if the search identifies any common astrophysical features in these clumps.

6.2 Data Reduction

6.2.1 Total number of spots

The following sample is not distance limited because the distances for quite a few of the clumps in this sample are uncertain. These uncertain distances are either because the clumps lie within 3 degrees of the galactic centre or they lie within 290 and 300 degrees for the galactic longitude in ATLASGAL (Urquhart et al., 2018). This means that there may be a possible distance bias in our results.

The total number of spots per clump is the first parameter to be investigated. This was found by counting all of the water maser spots of every WMG per clump. 3σ limits were applied to the whole sample of ATLASGAL clumps that have at least one 22.235 GHz H_2O maser. The 3σ limit was calculated to be 17.59 water maser spots, this was calculated by plotting a histogram of the total water maser spots per clump for all clumps, and then fitting a Gaussian to the resulting plot (see Figure 6.1). This data was initially fitted to a Poisson distribution, however this ended up not providing a good fit to the data, so we elected to use the Gaussian distribution.

Applying the criterion identified 13 clumps that we will investigate in more detail (see Table 6.1 for clump details).

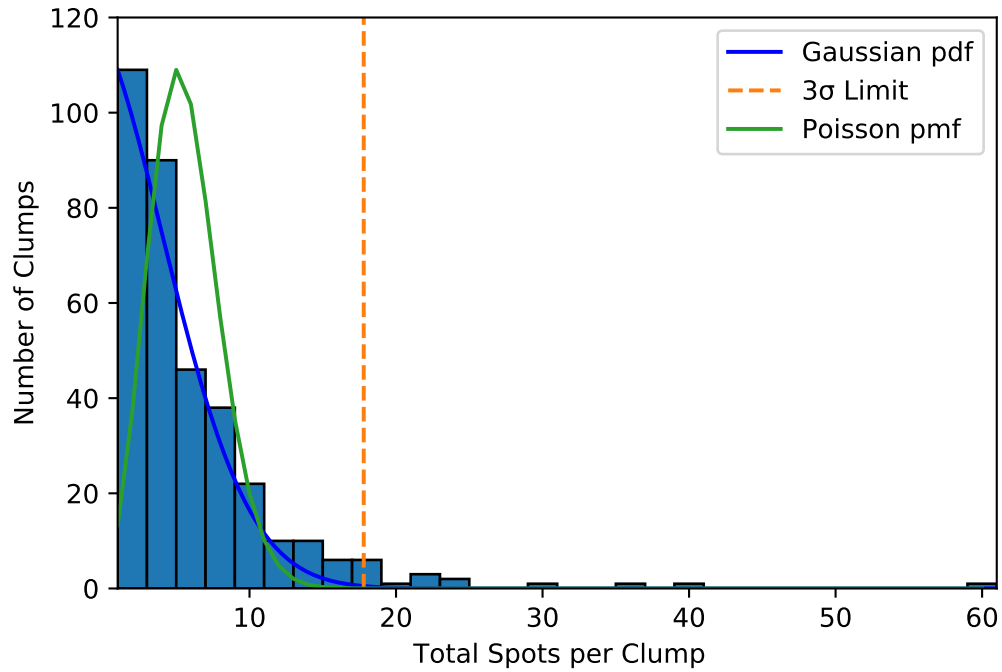


Figure 6.1: A histogram showing the total number of water maser spots per clump for all clumps containing at least one water maser in the ATLASGAL survey. A Gaussian pdf has been fitted to the plot, as well as a vertical line indicating the 3σ limit. We also show the Poisson distribution to demonstrate it does not fit our data well.

Table 6.1: A list of clumps that have 18 or more total water maser spots.

Clump Name	Number of WMGs	Total Number of Spots
AGAL000.678-00.027	1	61
AGAL007.471+00.059	2	21
AGAL012.208-00.102	2	18
AGAL024.789+00.082	2	22
AGAL291.579-00.432	2	19
AGAL301.136-00.226	2	18
AGAL305.357+00.202	2	24
AGAL318.779-00.137	1	21
AGAL330.954-00.182	1	35
AGAL331.512-00.102	1	40
AGAL336.994-00.027	3	18
AGAL345.699-00.091	1	23
AGAL357.968-00.162	1	30

6.2.2 Spots Per Group

The other criterion by which clumps are defined as interesting, are those that contain WMGs with a significant quantity of WMSs. Using Figure 6.2, the 3σ limit can be calculated, which is revealed to be 15.88 water maser spots per group. This means that any clump hosting a WMG containing 16 or more spots would be flagged as interesting and included in our analysis. The resulting clumps containing these WMGs can be seen in Table 6.2.

This results in a list of 11 WMGs in 11 unique clumps. As expected, the clumps identified in Table 6.2 do have quite a large overlap with the clumps identified in Table 6.1. 8 of the clumps in Table 6.2 were already in Table 6.1. The clumps that are unique to this table have an individual WMG with a large number of spots, but not large enough to have a significant number of spots in the whole clump. These were AGAL305.799-00.244, AGAL310.879+00.004 and AGAL311.642-00.381. All

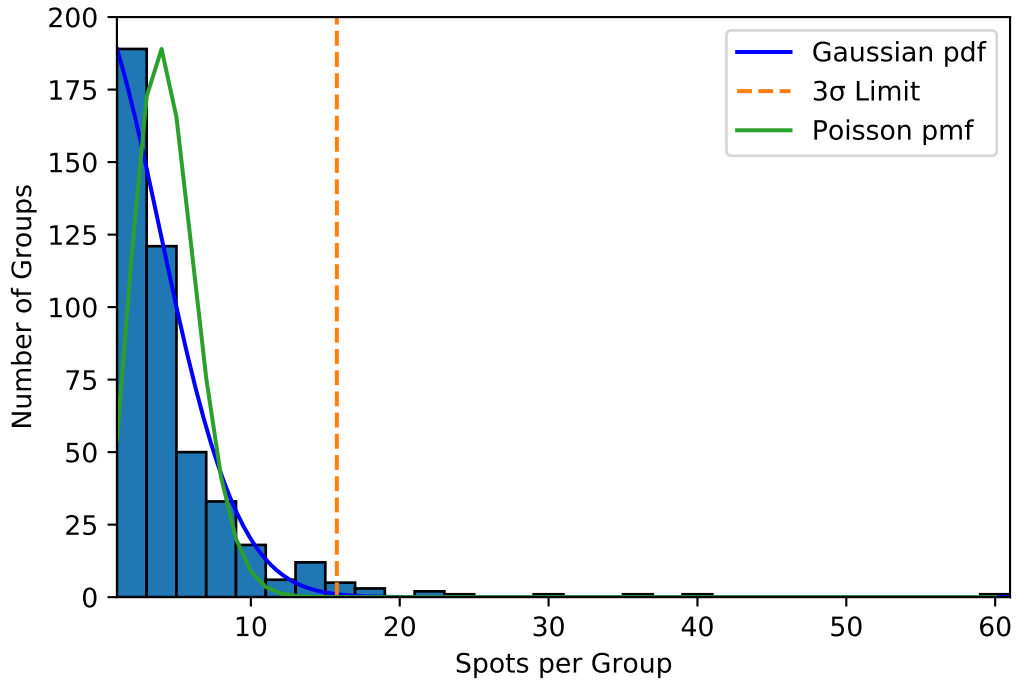


Figure 6.2: A histogram showing the number of water maser spots per group for all water maser groups in the HOPS survey that have an ATLASGAL association. A Gaussian pdf has been fitted to the plot, as well as a vertical line indicating the 3σ limit. We also show the Poisson distribution to demonstrate it does not fit our data well.

of these clumps have one WMG that contains 16 or 17 spots, which are the only conditions that would make a clump unique to Table 6.2.

Table 6.2: All WMGs that have 16 or more spots. The * clumps are those that are unique to this table.

Clump Name	Group Name	Number of Spots per Group	Number of WMGs per Clump
AGAL000.678-00.027	G000.677-0.028	61	1
AGAL012.208-00.102	G012.209-0.102	17	2
AGAL305.357+00.202	G305.359+0.200	21	2
AGAL305.799-00.244 *	G305.799-0.245	17	1
AGAL310.879+00.004 *	G310.879+0.006	16	1
AGAL311.642-00.381 *	G311.643-0.380	17	1
AGAL318.779-00.137	G318.779-0.136	21	1
AGAL330.954-00.182	G330.954-0.182	35	1
AGAL331.512-00.102	G331.512-0.102	40	1
AGAL345.699-00.091	G345.698-0.090	23	1
AGAL357.968-00.162	G357.967-0.163	30	1

In total, the two criteria have provided us with 16 unique clumps that either have a significant number of WMSs, or host a WMG that contains a significant number of WMSs.

6.2.3 Velocity Checks

We will now perform velocity checks on the data, as we did in Chapter 5. We will refer the reader to Section 5.2 for a discussion on the importance of velocity checks, but in this section we will skip straight to the methodology.

We can check if a water maser is associated with its host clump if its velocity lies within a particular range of the clump velocity. The difference between these two velocities is called the velocity offset of the maser. The range for water masers has already been determined in Section 5.2, and was calculated to be 17.1 km/s using 3σ limits. If the velocity offset of a water maser lies above this value, it will be

deemed unassociated and omitted from our analysis. We decide that a group should be discarded from our search if none of their WMSs fall into this range. A clump will then be discarded if the omission of an unassociated WMG reduces the total number of spots below the 18 spot threshold.

In Table 6.3 we calculate the average of the velocities of all WMSs and use this as the WMG velocity. This is only performed to give the reader an idea of the velocity offset between the WMSs and the clump, since we do not exclude WMGs based on this average velocity.

The velocities of clumps are not available within the inner 3 degrees of the galactic centre ($357^\circ \leq l \leq 3^\circ$), nor are they available at $290^\circ \leq l \leq 300^\circ$. This means that AGAL000.678-00.027, AGAL291.579-00.432, and AGAL357.968-00.162 cannot have velocity checks performed on them. Since there is no reason to assume these clumps would have had unassociated water masers they will remain in our analysis.

Table 6.3: A table showing all WMGs where none of their individual spots had a velocity within 17.1 km/s of the clump. The columns labelled v off, clump v and WMG v stand for velocity offset, clump velocity and water maser group velocity respectively.

Clump Name	Group Name	v off (km/s)	clump v (km/s)	WMG v (km/s)
AGAL024.789+00.082	G024.792+0.082	40.19	110.2	70.01
AGAL336.994-00.027	G336.993-0.026	54.60	-119.8	-174.40
AGAL336.994-00.027	G336.995-0.024	52.67	-119.8	-172.47

In summary, there were 3 WMGs flagged as unassociated with 2 unique clumps in Table 6.3.

Following the conditions for discarding a clump, both of the flagged clumps were discarded from our analysis. This now leaves a total of 14 clumps to be imaged, where we know the WMGs contained within them are more than likely associated, which makes our data more robust.

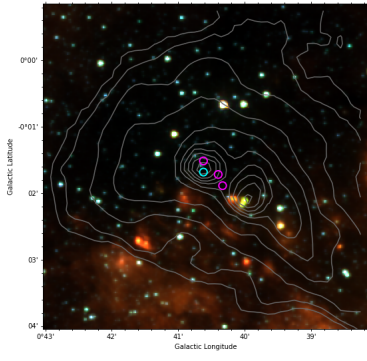
The remaining clumps in the sample will now be referred to as the “Many Water Maser” sample (MWM sample), where all of these clumps have a significant quantity of WMSs.

6.3 Multi-Wavelength Images

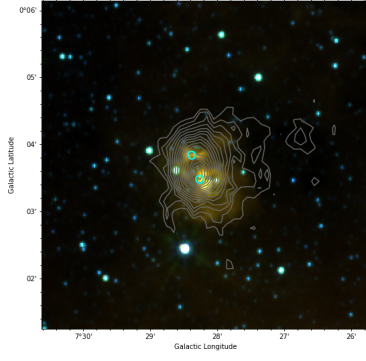
Now that we have defined our sample, we will provide multi-wavelength images for all of these clumps so that we can point out their particular features that may be driving the large number of WMSs that they host. We will use the same wavelengths to create these images as we did in Chapter 5. In this chapter, we provide the whole MWM sample of 4.6, 5.8 and 8.0 μm images in Figure 6.3.

After this, we will also lay out the physical parameters of the MWM sample (see Table 6.4). This includes the luminosity, mass and the L/M ratio. We do this because we expect these clumps to show higher luminosities and more active star forming centres as a result of the positive correlation between the quantity of WMSs and the luminosity of the clump identified in Chapter 4. If this hypothesis is true, then targeting unusual sources by their number of WMSs may be a viable method of targeting clumps with highly active star forming centres.

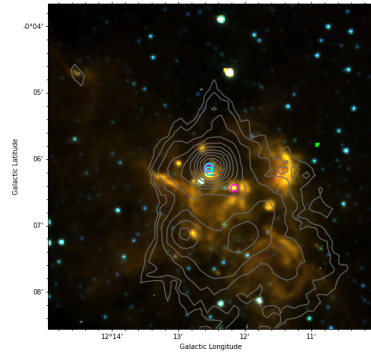
A final remark is that three of the clumps in the MWM sample do not have their physical parameters available to us as they are located in regions of space that ATLASGAL have not determined physical properties for ($357^\circ \leq l \leq 3^\circ$ or $290^\circ \leq l \leq 300^\circ$). Therefore, only the parameters of the remaining 11 have been presented in Table 6.4.



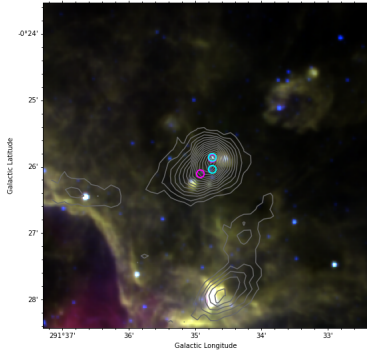
(a) AGAL000.678-00.027



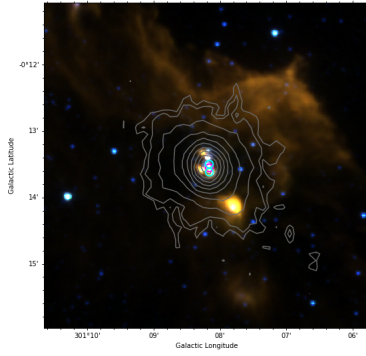
(b) AGAL007.471+00.059



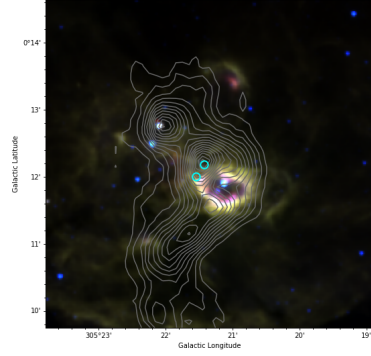
(c) AGAL012.208-00.102



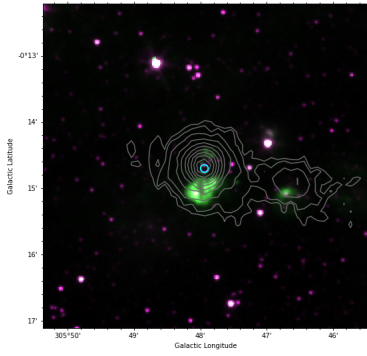
(d) AGAL291.579-00.432



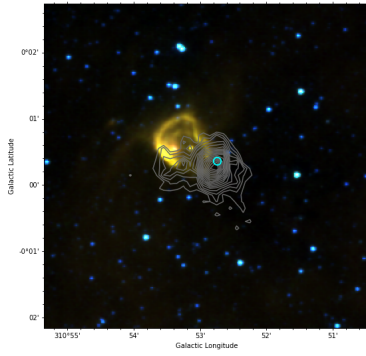
(e) AGAL301.136-00.226



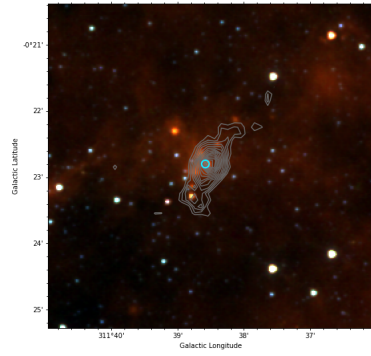
(f) AGAL305.357+00.202



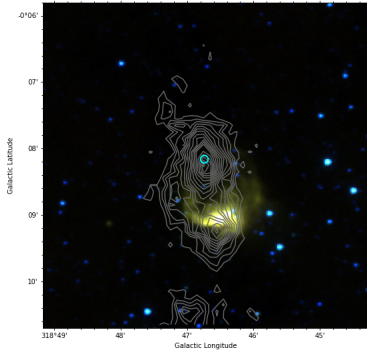
(g) AGAL305.799-00.244



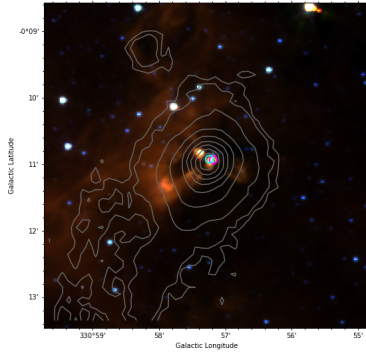
(h) AGAL310.879+00.004



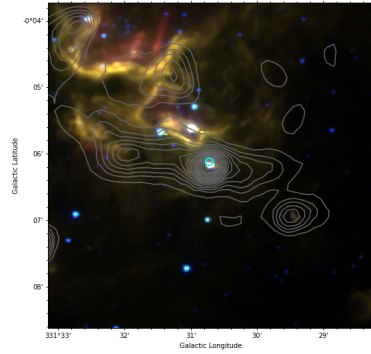
(i) AGAL311.642-00.381



(j) AGAL318.779-00.137



(k) AGAL330.954-00.182



(l) AGAL331.512-00.102

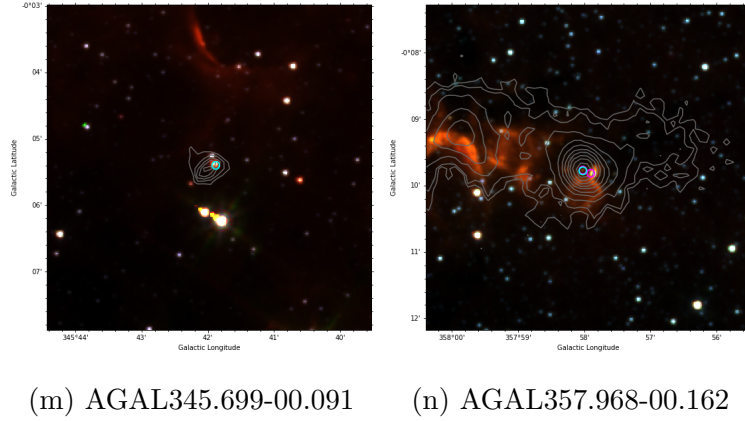


Figure 6.3: All 4.6, 5.8, 8.0 micron images mapped in blue, green and red respectively for every clump that was identified in the MWM sample. See Figure 5.3 for more details.

Table 6.4: Luminosity, Mass and L/M ratio values for all MWM clumps that had their parameters calculated by ATLASGAL.

Clump Name	Luminosity / L_{\odot}	Mass / M_{\odot}	L/M Ratio
AGAL007.471+00.059	922	24.4	29.1
AGAL012.208-00.102	1834	46.5	35.6
AGAL301.136-00.226	11600	58.9	38.1
AGAL305.357+00.202	16100	78.5	99.6
AGAL305.799-00.244	2875	28.5	162
AGAL310.879+00.004	261	17.4	15.8
AGAL311.642-00.381	756	8.31	145
AGAL318.779-00.137	372	51.9	4.04
AGAL330.954-00.182	21100	103	20.0
AGAL331.512-00.102	8095	52.5	128
AGAL345.699-00.091	194	2.92	50.8

6.4 Discussion

The MWM sample has revealed 14 clumps that have a significant number of WMSs contained within their 870 μm contours. These 14 clumps were comprised of 8 BM clumps and 6 WMO clumps, which contained a total of 19 individual WMGs.

From the MWM sample, we can see that a common feature between these clumps is the presence of a HII region, where we identify 9 out of the 14 clumps ($\sim 64\%$) that have their masers associated with the PDR of a HII region (see Figures 6.3c, 6.3h, 6.3l). In all cases, there is clearly strong feedback from the embedded HII region that is driving shocks into their natal clump. These shocks will then generate water masers (Walsh et al., 2014). The presence of a HII region signifies a high-mass star forming region, which would pertain to clusters of protostars with numerous outflows that can also produce water masers (Walsh et al., 2014).

We also observe that the MWM clumps have higher average luminosities, L/M ratios and masses than the average clump from the ATLASGAL database. The mean values of the physical parameters for the ATLASGAL sample were $646 \pm 62 L_{\odot}$, $29 \pm 0.5 M_{\odot}$ and $7.6 \pm 0.5 L_{\odot}/M_{\odot}$, whereas the mean values for the MWM sample were $5830 \pm 2120 L_{\odot}$, $43 \pm 8.8 M_{\odot}$ and $66 \pm 16.3 L_{\odot}/M_{\odot}$. Despite the small sample size for the MWM sample, the errors in the luminosity and L/M ratio show no overlap between the two samples. They also have comparable luminosities and L/M ratios to BM clumps, which are $4650 \pm 1040 L_{\odot}$ and $41 \pm 6.2 L_{\odot}/M_{\odot}$, respectively (refer back to Table 4.3). This tells us that clumps with more WMSs do, in general, represent more luminous and more evolved star forming regions, which supports our initial hypothesis. We speculate this is due to more luminous protostellar objects radiating more energy to their surroundings. This increased quantity in energy would then shock more water molecules in the ambient material surrounding the star, hence it is statistically more likely that a greater number of water molecules would begin to mase. Additionally, more luminous protostars also tend to be more evolved because they have accreted more material over a longer period of time (Molinari et al., 2008). This explains why we also see more WMSs associated with more evolved objects.

The majority of the WMGs in this sample are associated with HII regions, however the clump “AGAL000.678-00.027” has no association with HII regions. This clump is particularly interesting because it has a WMG that contains more spots than any other clump in the entire ATLASGAL sample (61 spots). This WMG appears to be driven by a large cluster of MSF, since it is surrounded by three methanol masers (Breen et al., 2013) (see Figure 6.3a). This shows that a large congregation of MYSOs could produce a more powerful centre than the ionising fronts from HII regions, but since this is only evident in one clump it can be considered to be a rare occurrence. We find that no research has been conducted on this clump after analysing the literature.

In summary, the MWM sample has provided us with clumps that have higher luminosities and L/M ratios than the sample from ATLASGAL. It has also determined that HII regions are a common feature of clumps with many WMSs, which tells us that they are crucial in aiding the formation of the most active SF regions. Since two of the main goals of this chapter were answered with the MWM sample, we conclude that this method of searching for clumps was successful. Additionally, we suggest that this method should be repeated for future samples, since our end sample size consisted of a relatively low 14 sources. These future searches will be able to confirm the association of HII regions, intense SF and the quantity of WMSs more concretely.

6.5 Summary

This chapter looked to select interesting clumps / WMGs from the ATLASGAL database. Clumps / WMGs were deemed interesting if they contained a significantly large quantity of water maser spots. All sources identified in this manner were labelled the “Many Water Maser” sample (MWM sample). This criteria was applied with the goal of identifying active, luminous and evolved clumps, since in Chapter 4 it was found that the quantity of WMSs was positively correlated with the luminosity and L/M ratio of the clump. We then produced multi-wavelength images for the MWM sample and classified them in order to deduce if there were any particular

astrophysical processes that are common between them.

We find that 9 out of the 14 clumps in the MWM sample ($\sim 64\%$) were identified to contain a water maser associated with the PDR of a HII region. This suggests that HII regions are a key process in forming the most active of star forming centres of molecular clumps, particularly their photoionisation shocks that can cause multiple dense cores to collapse and form clusters of stars (Elmegreen and Lada, 1977).

Additionally, the average luminosity and L/M ratio of the MWM sample is higher than the ATLASGAL sample and comparable to BM clumps, which supports our hypothesis that more luminous and evolved clumps results in more WMSs. We suspect that more WMSs are associated with more luminous objects since these objects will transfer more energy into their surroundings, which increases the likelihood that water molecules will be provided with a pumping mechanism and population inversion needed for masing. The HII regions that are common in this sample also signify that these masers are located in MSF regions. These clumps are therefore likely to host evolving protoclusters, which will lead to more YSOs that in turn will produce multiple outflows that can generate more water masers (Walsh et al., 2014).

Overall, we conclude that this method of searching for interesting clumps is a success. This is because the MWM samples suggests that clumps with more WMSs show different physical parameters compared to the rest of the ATLASGAL sample. It also shows that we are far more likely to detect HII regions in these clumps, which implies that they are a primary cause of the increased luminosities that we observe. Ultimately, we do end up with a very small sample size of clumps, so our results cannot be considered conclusive. We argue that this method should be repeated with future surveys for targeted searches of clumps with intense SF, and so that we can confirm the results of this paper.

Chapter 7

Summary and Conclusions

The main aim of this thesis was to see if more insight could be drawn from the maser properties than just their association statistics. This led us to investigate the positions of masers within their clumps and the number of masers present in order to gain information about the star formation in their associated clumps. In the following paragraphs we will provide a brief summary of our results, discussing their implications and outline further work.

We have investigated various types of maser associated clumps to see if there was any discernible difference between their physical properties. We found that maser associated clumps exhibited significantly different physical properties to the general population of ATLASGAL clumps. They generally have higher luminosities and are more evolved, which agrees with the results of [Billington et al. \(2020\)](#). It was then found that clumps hosting both 22.235 GHz H₂O masers and Class II 6.7 GHz methanol masers had significantly higher L/M ratios, luminosities and masses than clumps associated with only a single emission line of water or methanol masers. The high L/M ratios indicate that these clumps with both masers appear to be more evolved than single maser association clumps. The higher masses and luminosities would also suggest that these clumps are forming larger clusters and more high-mass stars. The larger clusters would result in more protostars and more outflows, which would account for the higher abundance of water masers. These large clusters

are also more likely to form MYSOs, which are the only objects that can generate Class II 6.7 GHz methanol masers (Breen et al., 2013). Clumps with single maser associations are a reliable sign of star formation, but clumps with both methanol and water masers show more intense star formation, and massive, evolved clusters. We also compared our results to the “straw man” model developed by Ellingsen et al. (2007), which predicted that masers appear in sequence, where the Class I methanol masers appear first, then Class II methanol masers followed by water masers and lastly OH masers. Billington et al. (2020) have found that the water and Class II methanol masers actually have a much larger overlap in their lifetimes than predicted by the “straw man” model. Our results also disagree with the “straw man” model, since we find that clumps (and by extension star forming regions) with both methanol and water masers are significantly more evolved than the appearance of just one maser, which implies that the current model is too simple. Olmi et al. (2014) also finds that combining OH and methanol lines results in finding more luminous and massive clumps. Going forward, we suggest that other combinations of maser species should be tested to help develop a more detailed model that can better predict these evolutionary states.

We used Gaussian statistics to determine an offset criterion to identify masers that were significantly offset from the centre of their clumps, which was defined by the peak sub mm emission from ATLASGAL. Applying this criterion identified 20 clumps for further investigation. These were imaged with the use of IR emission from the GLIMPSE, WISE and Hi-Gal surveys (Werner et al., 2004; Wright et al., 2010; Molinari et al., 2016) to help identify the pumping source of the masers. The majority of these large offset masers were found to be associated with either large HII regions or unresolved sub-structures in individual ATLASGAL clumps that were offset from the brightest sub mm peak, indicating multiple sites of star formation being present in these clumps. The clumps from ATLASGAL are more structured and the star formation is more distributed than expected. Much of the complexity has been missed from previous studies that have only looked at association statistics.

We identify a number of clumps hosting masers towards their edges that do not have

a sub mm or IR counterpart. These masers have been confirmed to be positionally and kinematically coincident with their associated clump. These may result from external conditions, but the lack of any mid-IR emission or dust feature coincident with these masers means their nature remains a mystery. Future work from molecular line surveys may be an effective way to check if these masers are a result of external shocks, kinematic signatures or density enhancements that are not seen at the mid-IR. Either way, further analysis is required to grasp an understanding of the physical processes driving these masers.

Finally, we attempted to identify and image sources that host a significantly large quantity of water maser spots, with the goal of pinpointing more luminous and active star forming regions. We also investigated water maser groups that contain a significant quantity of spots, as this would indicate more concentrated star forming activity. We again, examined the MIR images to investigate the nature and environment giving rise to these masers. We determined that these clumps were significantly more evolved and luminous than the average ATLASGAL clump. The luminosities and L/M ratios were found to be similar to BM clumps, which implies that they also contain evolved and intense star formation. Therefore, searching for clumps containing a large quantity of water masers is also an effective method for looking at more extreme examples of star formation.

We also find that 64% of the sources contained masers that were clearly associated with a PDR of a HII region. This suggests that HII regions are quite important in generating the intense star formation that we observe in this sample. However, our sample size for these clumps was low (14), so a further analysis of these types of clumps will give us a more concrete view on the physical processes that generate intense star forming regions and the many masers that result from them.

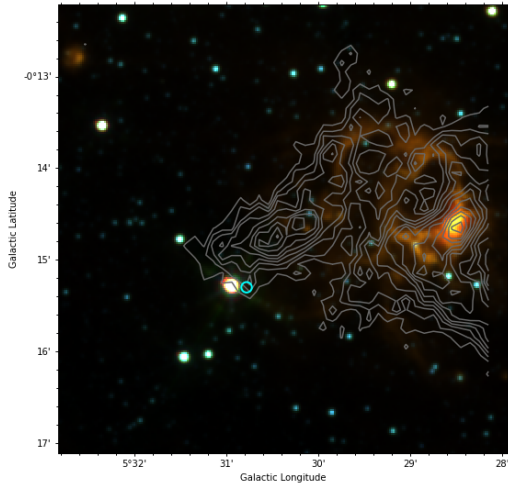
The result presented in this work have been useful in the context of maser properties and massive star formation. We have managed to prove that the positions and physical parameters of masers can be used to great effect to determine the nature of the star forming environment being investigated. This opens up the possibility of targeted searches for clumps with specific properties by using masers, which will

be a useful tool in improving our understanding of massive star formation going forward.

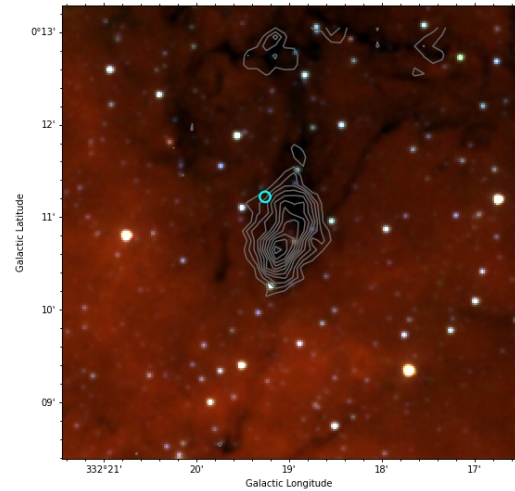
Appendix A

Multi-Wavelength Images - Large Offset Sample

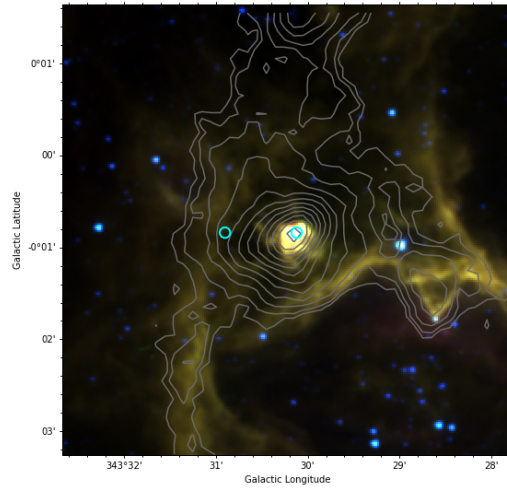
A.1 WMO Clumps - 4.6,5.8,8.0



(a) AGAL005.509-00.246



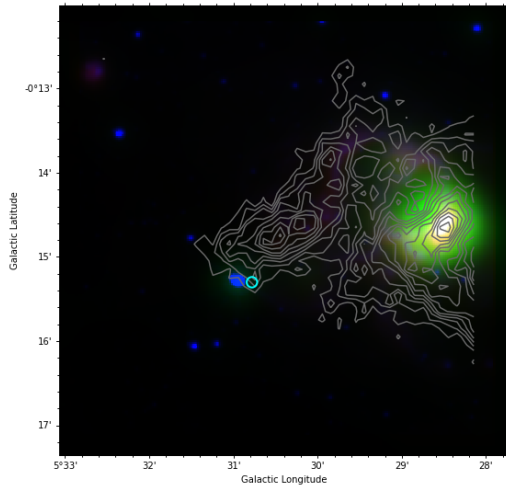
(b) AGAL332.317+00.177



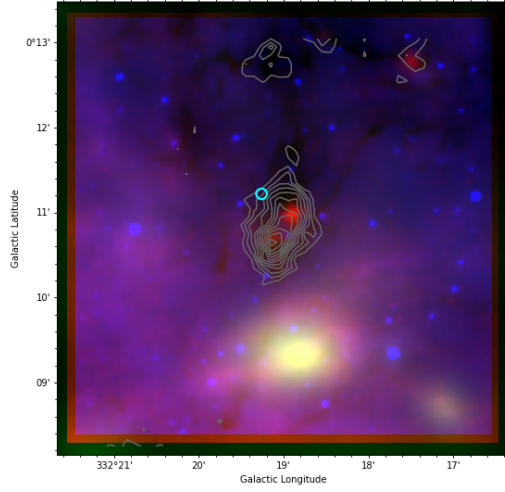
(c) AGAL343.502-00.014

Figure A.1: 4.6,5.8 and 8.0 micron images mapped out in blue, green and red filters respectively for all WMO clumps in the LO sample. See Figure 5.3 for more details.

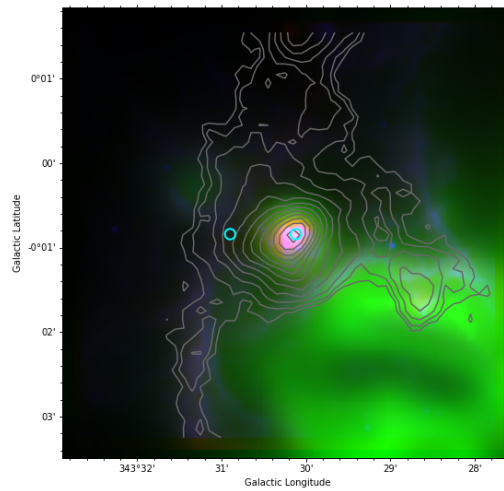
A.2 WMO Clumps - 8.0,22,70



(a) AGAL005.509-00.246



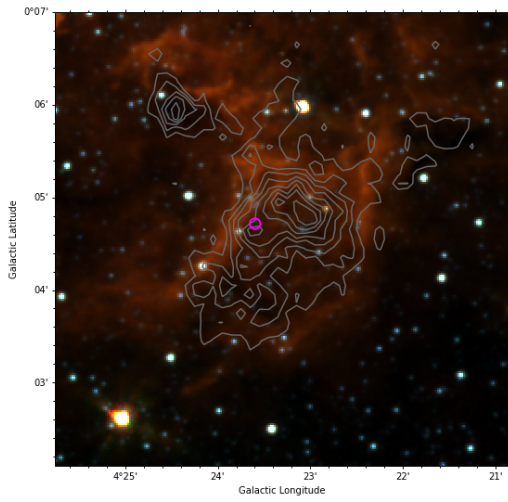
(b) AGAL332.317+00.177



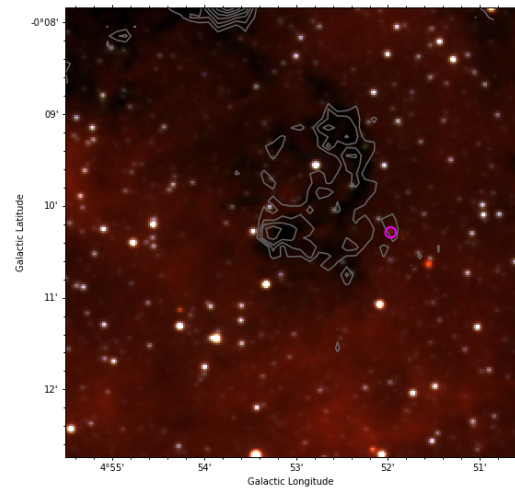
(c) AGAL343.502-00.014

Figure A.2: 8.0, 22 and 70 micron images mapped out in blue, green and red filters respectively for all WMO clumps in the LO sample. See Figure 5.3 for more details.

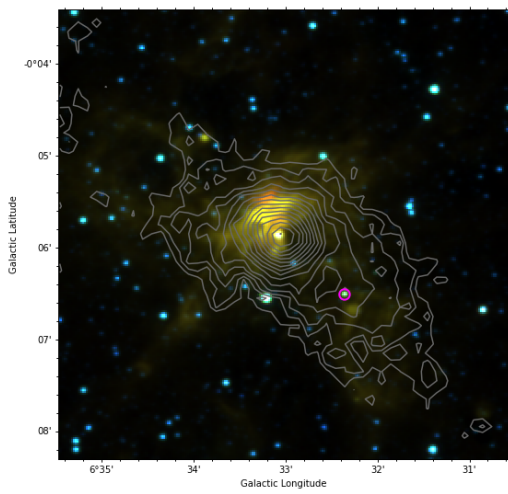
A.3 MMO Clumps - 4.6,5.8,8.0



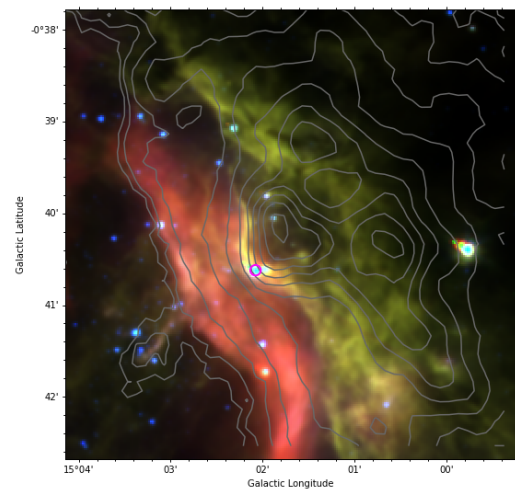
(a) AGAL004.384+00.079



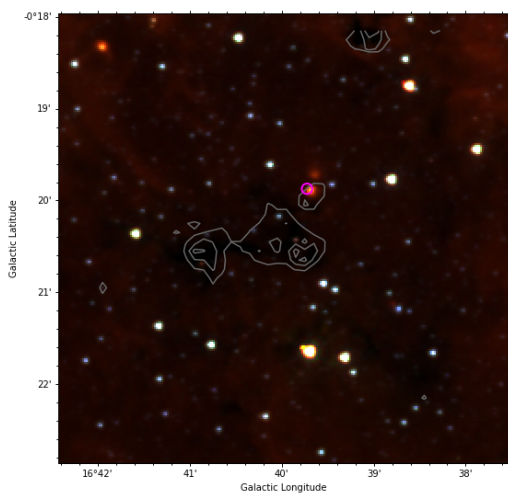
(b) AGAL004.887-00.171



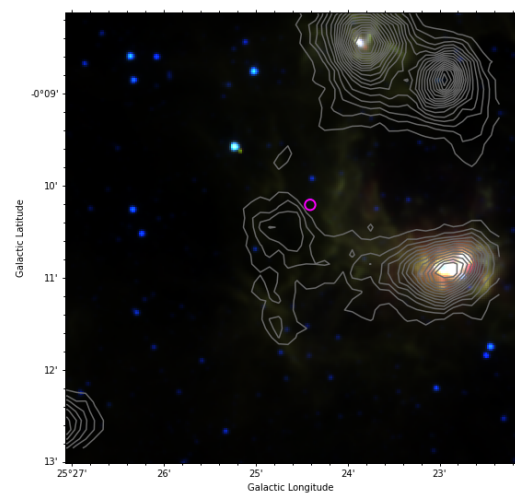
(c) AGAL006.551-00.097



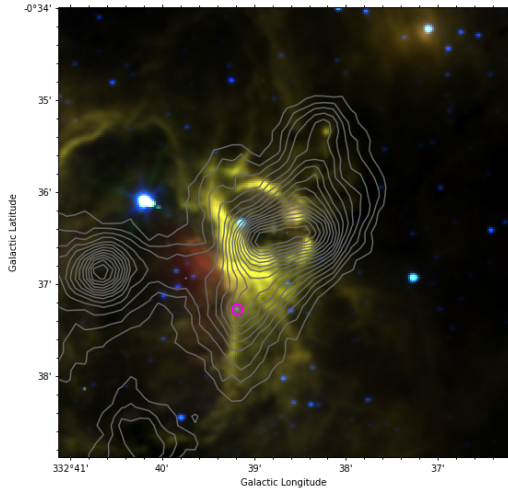
(d) AGAL015.029-00.669



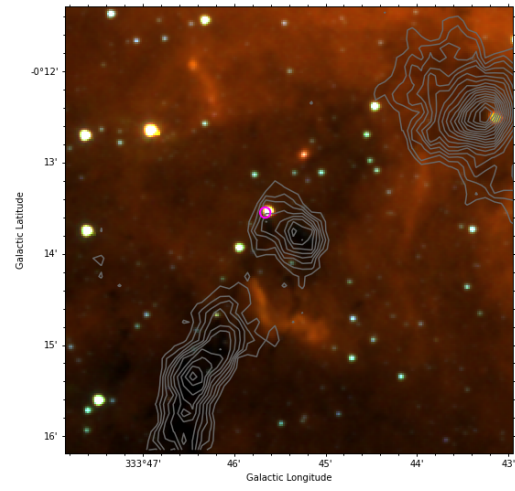
(e) AGAL016.662-00.342



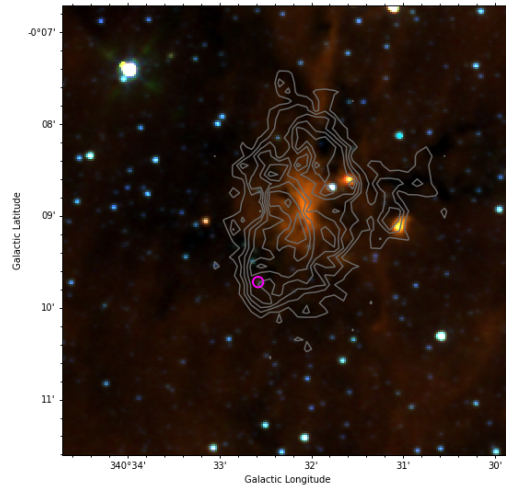
(f) AGAL025.412-00.174



(g) AGAL332.647-00.609



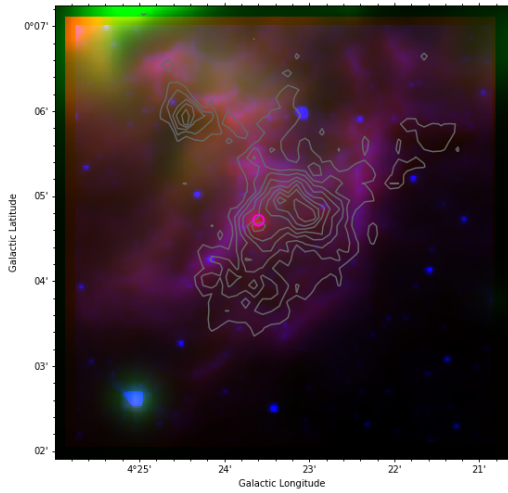
(h) AGAL333.754-00.229



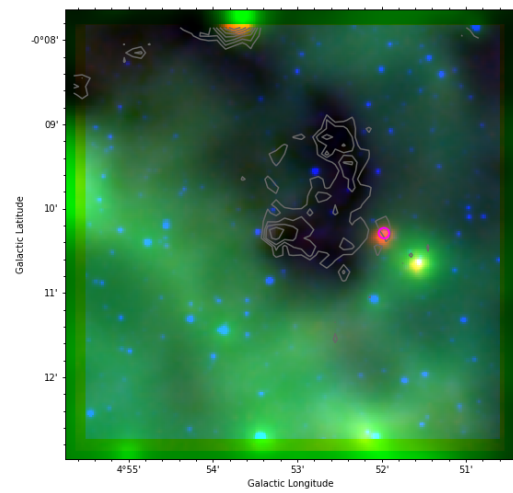
(i) AGAL340.536-00.152

Figure A.3: 4.6,5.8 and 8.0 micron images mapped out in blue, green and red filters respectively for all MMO clumps from the LO sample. See Figure 5.3 for more details.

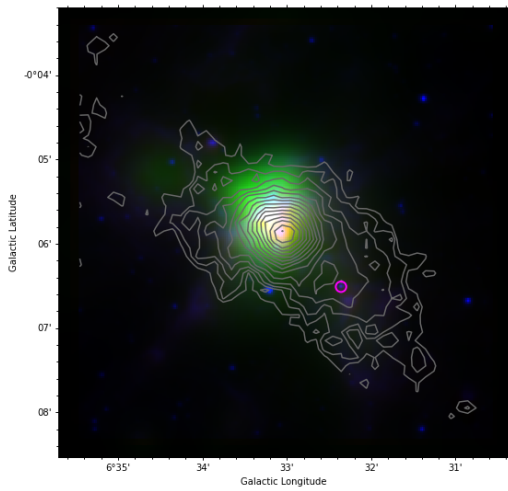
A.4 MMO Clumps - 8.0,22,70



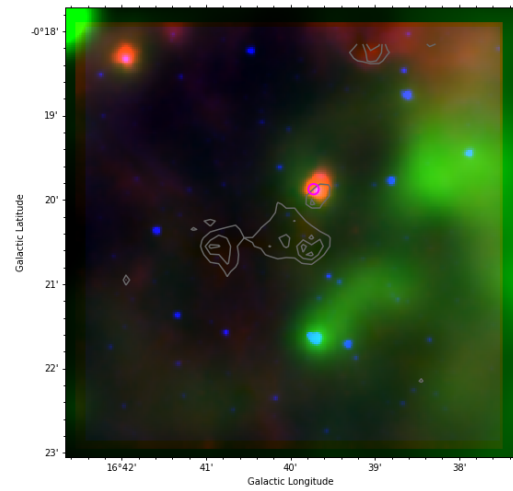
(a) AGAL004.384+00.079



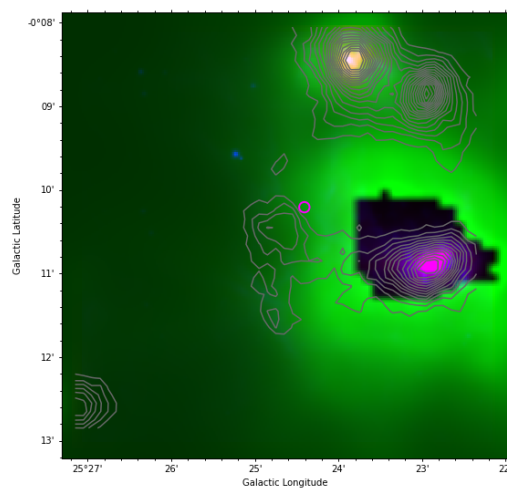
(b) AGAL004.887-00.171



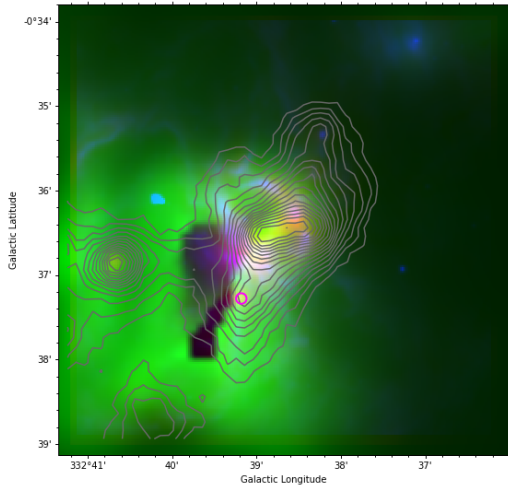
(c) AGAL006.551-00.097



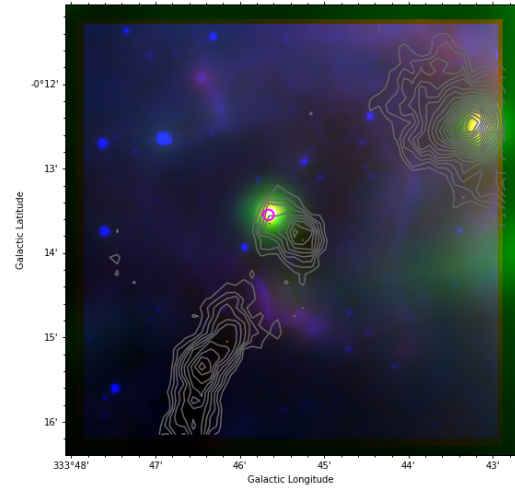
(d) AGAL016.662-00.342



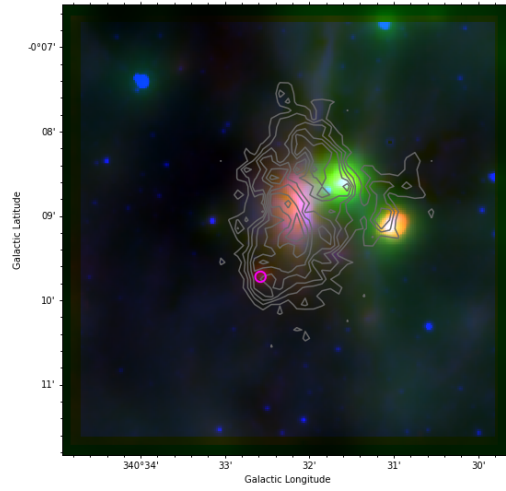
(e) AGAL025.412-00.174



(f) AGAL332.647-00.609



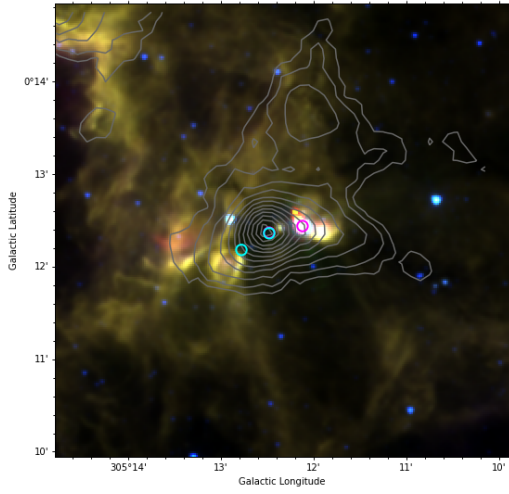
(g) AGAL333.754-00.229



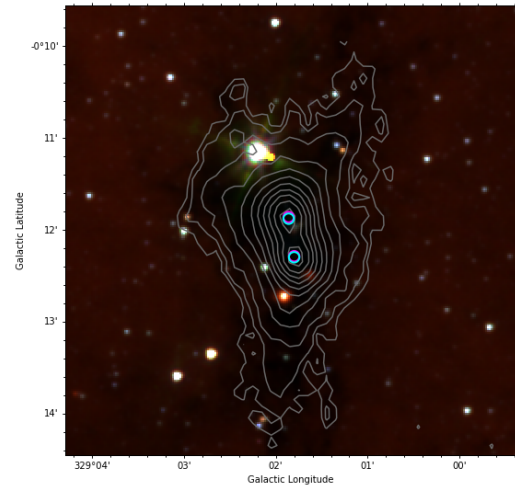
(h) AGAL340.536-00.152

Figure A.4: 8.0,22 and 70 micron images mapped out in blue, green and red filters respectively for all MMO clumps from the LO sample. See Figure 5.3 for more details.

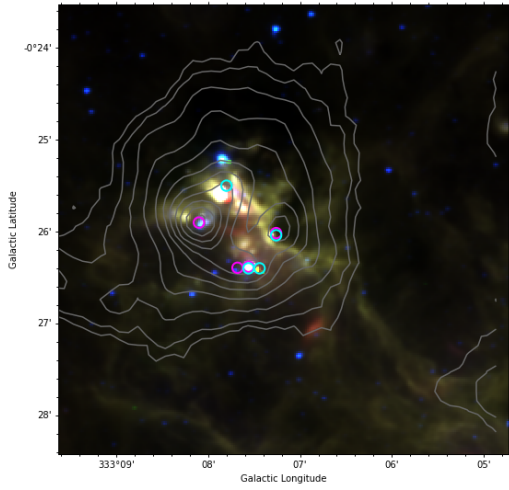
A.5 BM Clumps - 4.6,5.8,8.0



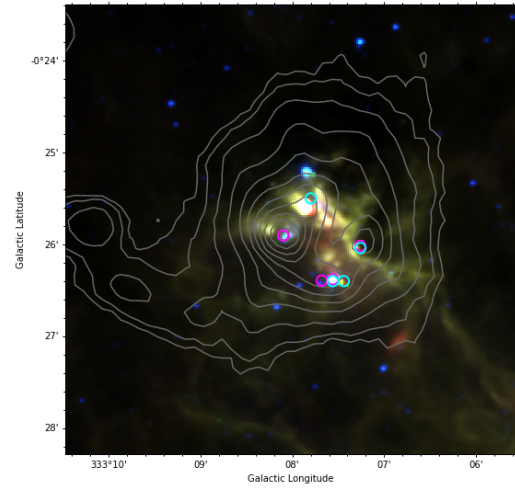
(a) AGAL305.209+00.206



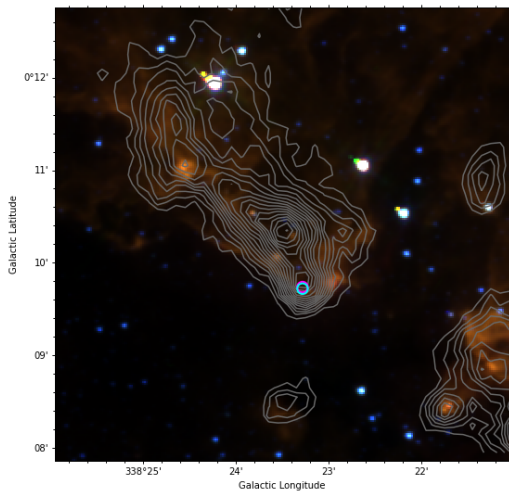
(b) AGAL329.029-00.206



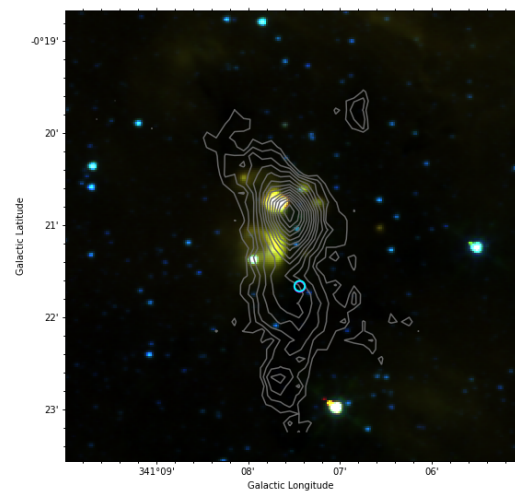
(c) AGAL333.121-00.432



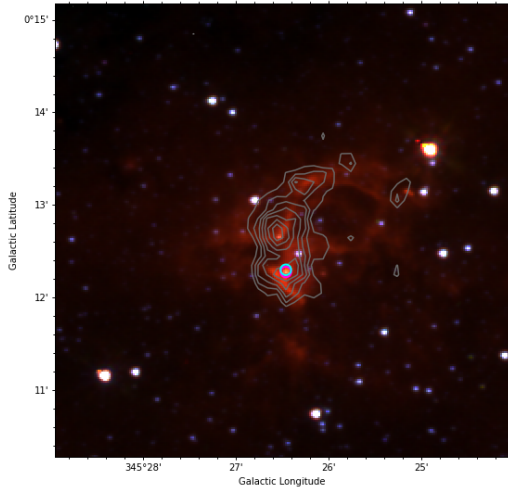
(d) AGAL333.134-00.431



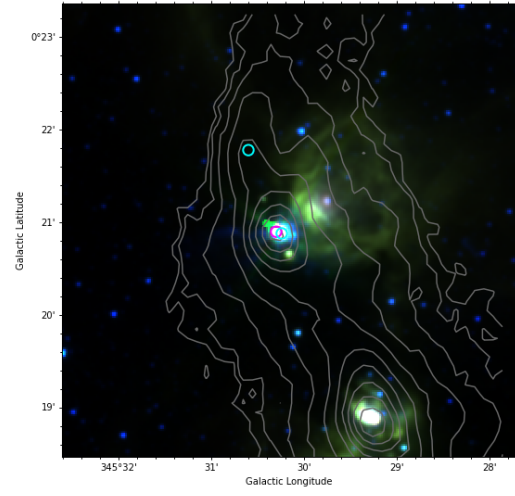
(e) AGAL338.391+00.172



(f) AGAL341.126-00.347



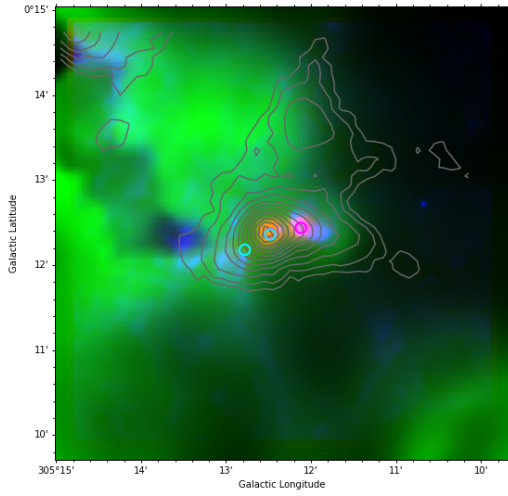
(g) AGAL345.443+00.212



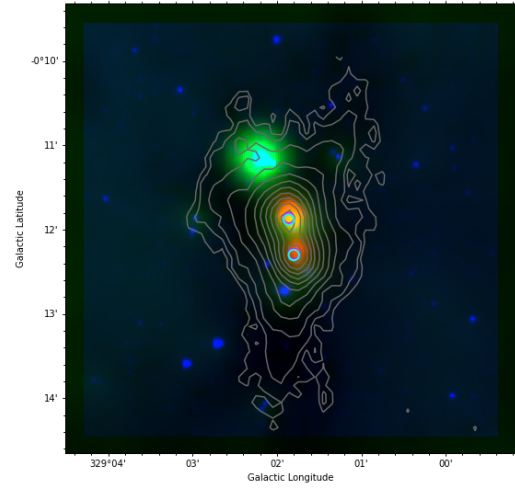
(h) AGAL345.504+00.347

Figure A.5: 4.6,5.8 and 8.0 micron images mapped out in blue, green and red filters respectively for all BM clumps in the LO sample. See Figure 5.3 for more details.

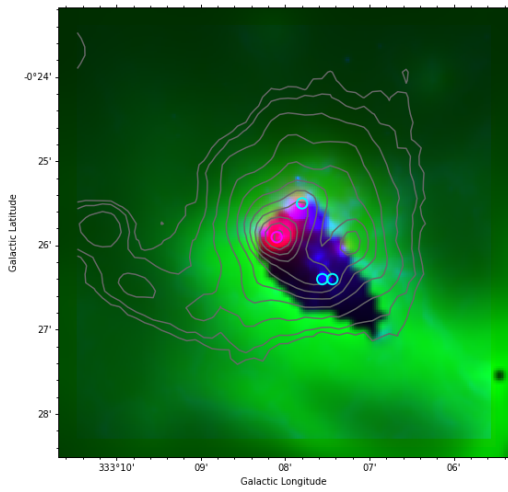
A.6 BM Clumps - 8.0,22,70



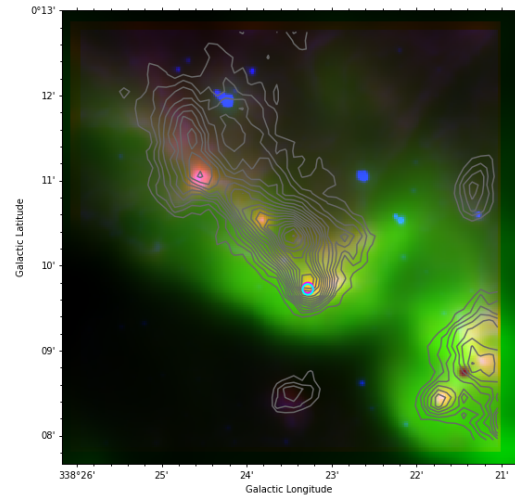
(a) AGAL305.209+00.206



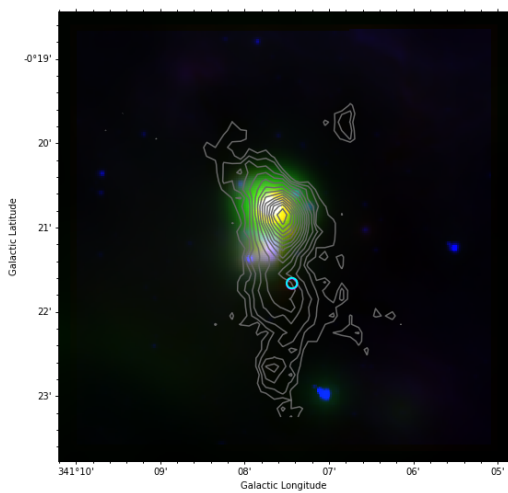
(b) AGAL329.029-00.206



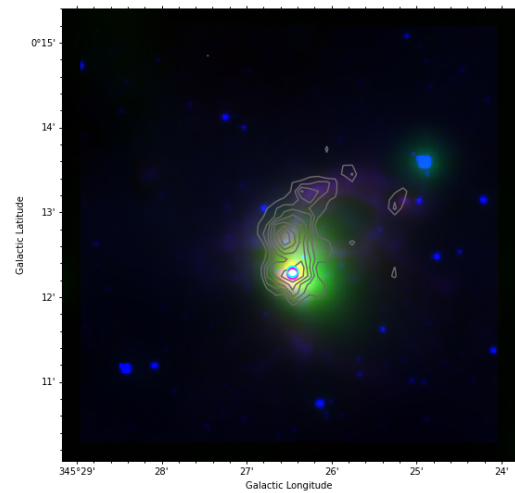
(c) AGAL333.134-00.431



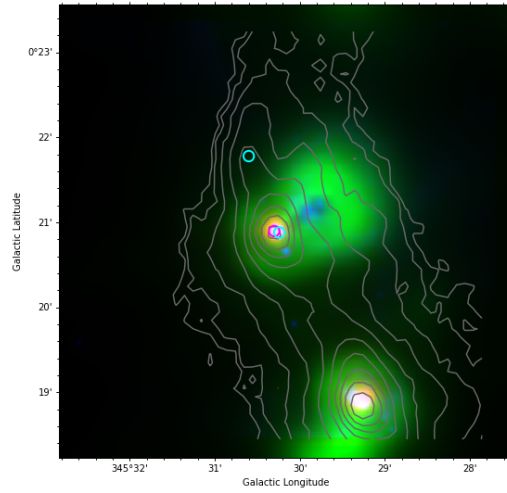
(d) AGAL338.391+00.172



(e) AGAL341.126-00.347



(f) AGAL345.443+00.212



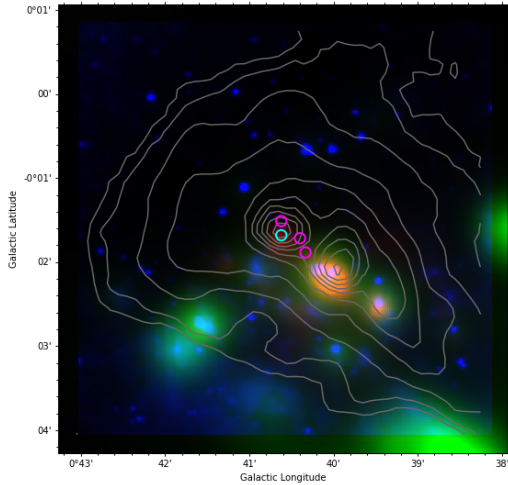
(g) AGAL345.504+00.347

Figure A.6: 8.0,22 and 70 micron images mapped out in blue, green and red filters respectively for all BM clumps in the LO sample. See Figure 5.3 for more details.

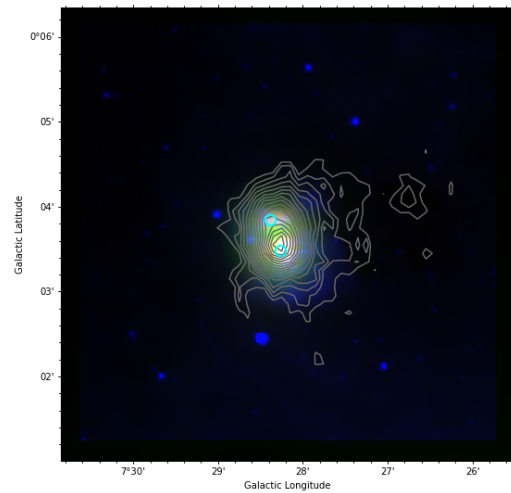
Appendix B

Multi-Wavelength Images - Many Water Masers Sample

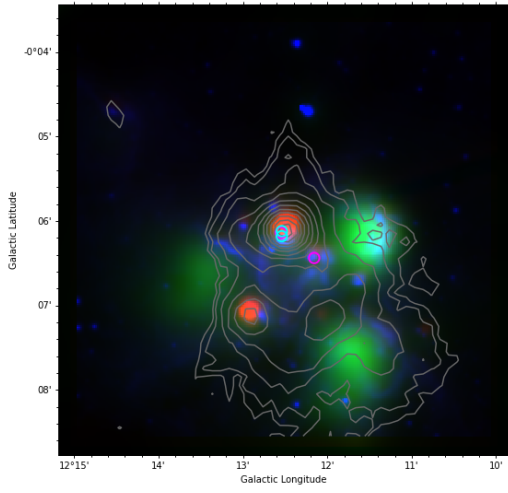
B.1 Clumps - 8.0,22,70 μm



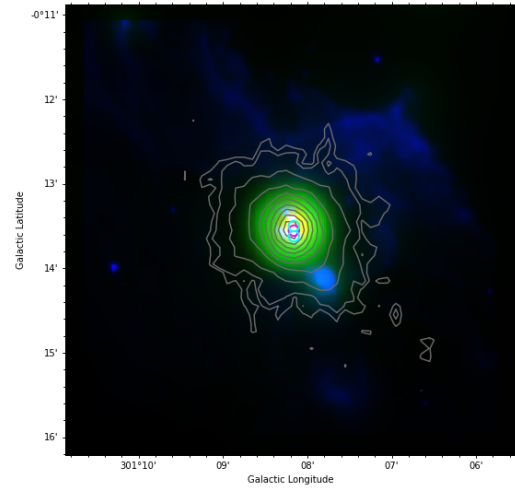
(a) AGAL000.678-00.027



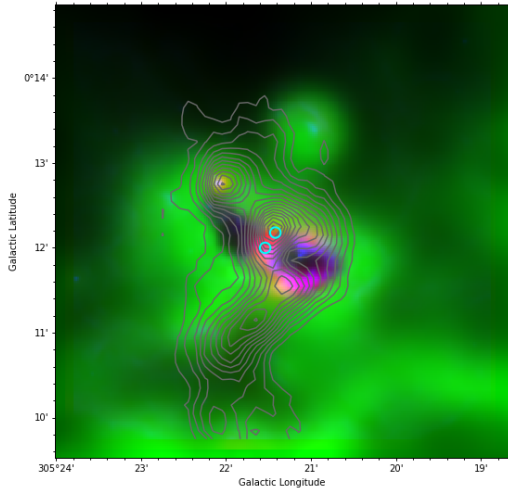
(b) AGAL007.471+00.059



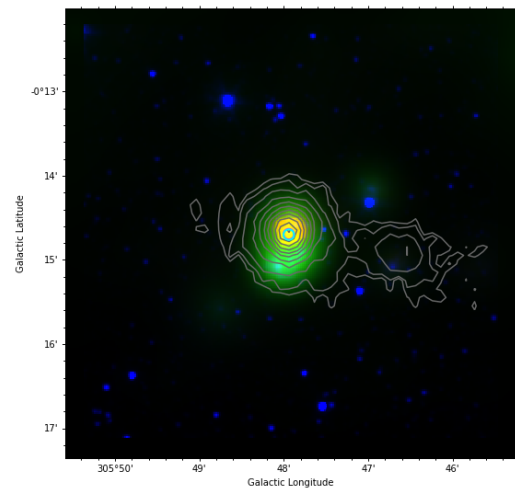
(c) AGAL012.208-00.102



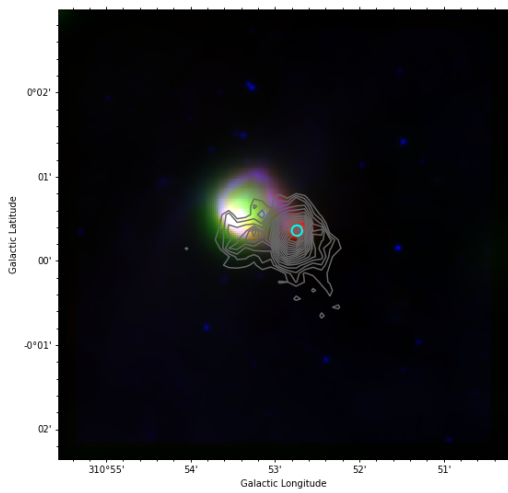
(d) AGAL301.136-00.226



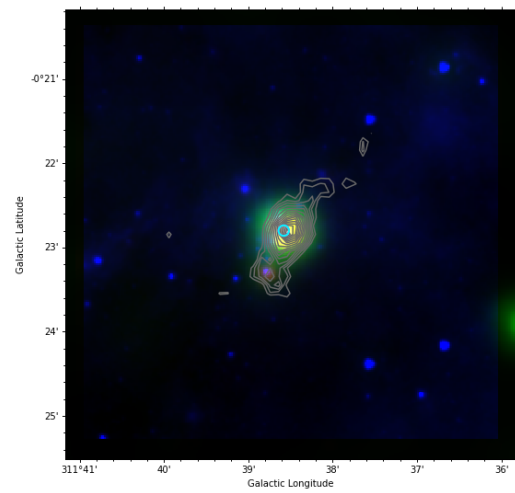
(e) AGAL305.357+00.202



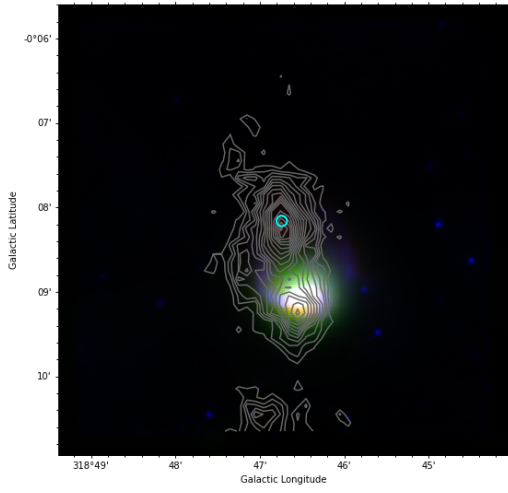
(f) AGAL305.799-00.244



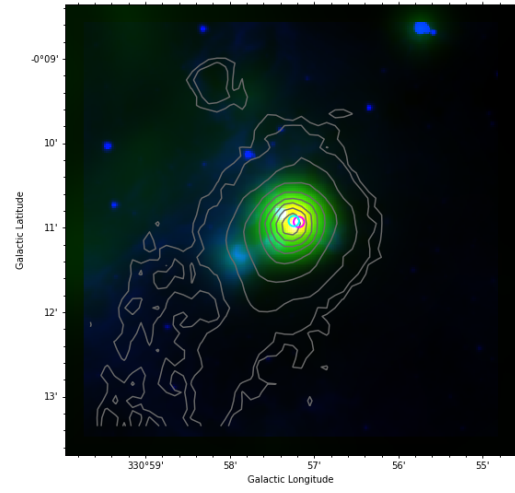
(g) AGAL310.879+00.004



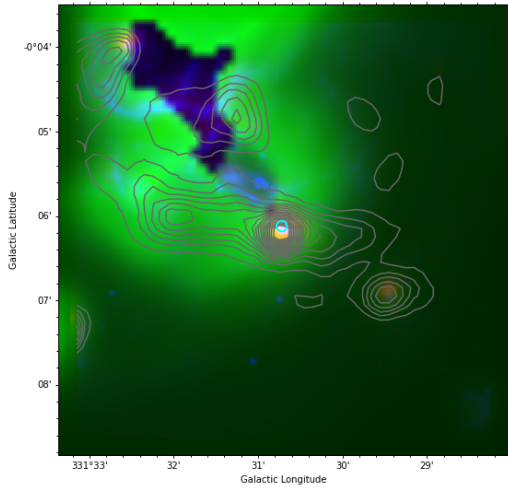
(h) AGAL311.642-00.381



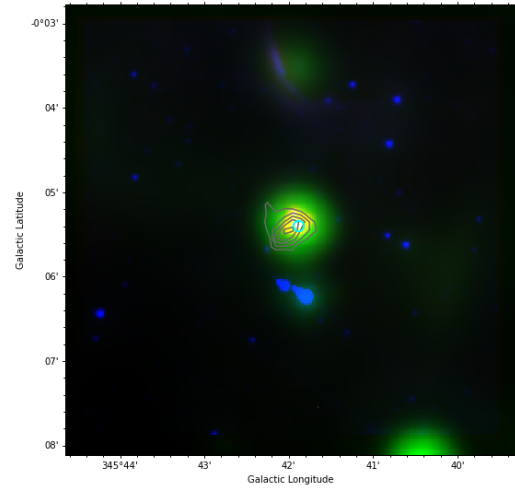
(i) AGAL318.779-00.137



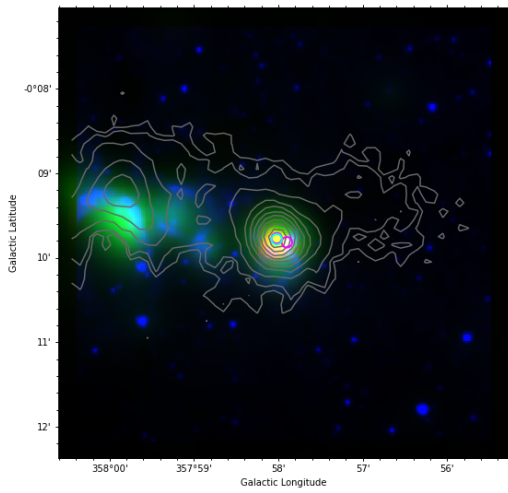
(j) AGAL330.954-00.182



(k) AGAL331.512-00.102



(l) AGAL345.699-00.091



(m) AGAL357.968-00.162

Figure B.1: All 8.0, 22, 70 micron images mapped in blue, green and red respectively for every clump in the MWM sample. See Figure 5.3 for more details. Some of the clumps had no available 22 micron emission, and so are not shown. All 4.6, 5.8 and 8.0 micron images for the MWM sample are available in Figure 6.3.

Bibliography

- Alton, P. B., Trehwella, M., Davies, J. I., Evans, R., Bianchi, S., Gear, W., Thronson, H., Valentijn, E., and Witt, A. (1998). Resolved 200 μ M images of nearby galaxies - evidence for an extended distribution of cold dust. *aap*, 335:807–822.
- André, P. (2011). *Spectral Classification of Embedded Stars*, pages 1549–1553. Springer Berlin Heidelberg, Berlin, Heidelberg.
- Andre, P., Ward-Thompson, D., and Barsony, M. (1993). Submillimeter Continuum Observations of rho Ophiuchi A: The Candidate Protostar VLA 1623 and Prestellar Clumps. *apj*, 406:122.
- Ballesteros-Paredes, J., Klessen, R. S., Mac Low, M. M., and Vazquez-Semadeni, E. (2007). Molecular Cloud Turbulence and Star Formation. In Reipurth, B., Jewitt, D., and Keil, K., editors, *Protostars and Planets V*, page 63.
- Bertin, E. and Arnouts, S. (1996). SExtractor: Software for source extraction. *aaps*, 117:393–404.
- Beuther, H., Schilke, P., Sridharan, T. K., Menten, K. M., Walmsley, C. M., and Wyrowski, F. (2002). Massive molecular outflows. *aap*, 383:892–904.
- Billington, S. J., Urquhart, J. S., König, C., Beuther, H., Breen, S. L., Menten, K. M., Campbell-White, J., Ellingsen, S. P., Thompson, M. A., Moore, T. J. T., Eden, D. J., Kim, W. J., and Leurini, S. (2020). ATLASGAL - relationship between dense star-forming clumps and interstellar masers. *MNRAS*, 499(2):2744–2759.
- Billington, S. J., Urquhart, J. S., König, C., Moore, T. J. T., Eden, D. J., Breen,

- S. L., Kim, W. J., Thompson, M. A., Ellingsen, S. P., Menten, K. M., Wyrowski, F., and Leurini, S. (2019). ATLASGAL - physical parameters of dust clumps associated with 6.7 GHz methanol masers. *MNRAS*, 490(2):2779–2798.
- Bonnell, I. A. (2005). *Competitive Accretion and the IMF*, volume 327, page 425. SUPA.
- Bonnell, I. A., Bate, M. R., and Zinnecker, H. (1998). On the formation of massive stars. *mnras*, 298(1):93–102.
- Breen, S. L., Ellingsen, S. P., Caswell, J. L., Green, J. A., Voronkov, M. A., Fuller, G. A., Quinn, L. J., and Avison, A. (2012). 12.2-GHz methanol maser MMB follow-up catalogue - I. Longitude range 330° to 10°. *mnras*, 421(2):1703–1735.
- Breen, S. L., Ellingsen, S. P., Contreras, Y., Green, J. A., Caswell, J. L., Stevens, J. B., Dawson, J. R., and Voronkov, M. A. (2013). Confirmation of the exclusive association between 6.7-GHz methanol masers and high-mass star formation regions. *mnras*, 435(1):524–530.
- Breen, S. L., Ellingsen, S. P., Johnston-Hollitt, M., Wotherspoon, S., Bains, I., Burton, M. G., Cunningham, M., Lo, N., Senkbeil, C. E., and Wong, T. (2007). A search for 22-GHz water masers within the giant molecular cloud associated with RCW 106. *mnras*, 377(2):491–506.
- Breen, S. L., Fuller, G. A., Caswell, J. L., Green, J. A., Avison, A., Ellingsen, S. P., Gray, M. D., Pestalozzi, M., Quinn, L. J., Richards, A. M. S., Thompson, M. A., and Voronkov, M. A. (2015). The 6-GHz methanol multibeam maser catalogue - V. Galactic longitudes 20°-60°. *mnras*, 450(4):4109–4136.
- Caswell, J., Fuller, G., Green, J., Avison, A., Breen, S., Ellingsen, S., Gray, M., Pestalozzi, M., Quinn, L., Thompson, M., and Voronkov, M. (2011). The 6-ghz methanol multibeam maser catalogue - iii. galactic longitudes 330° to 345°. *Royal Astronomical Society. Monthly Notices*, 417(3):1964–1995.
- Caswell, J. L., Fuller, G. A., Green, J. A., Avison, A., Breen, S. L., Brooks, K. J., Burton, M. G., Chrysostomou, A., Cox, J., Diamond, P. J., and et al. (2010). The

- 6-ghz methanol multibeam maser catalogue - i. galactic centre region, longitudes 345° to 6°. *Monthly Notices of the Royal Astronomical Society*, 404(2):1029–1060.
- Caswell, J. L., Haynes, R. F., and Goss, W. M. (1980). Survey of OH Masers at 1665 and 1667 MHz. I. Galactic longitudes 326deg to 340deg. *Australian Journal of Physics*, 33:639–669.
- Cernicharo, J., Thum, C., Hein, H., John, D., Garcia, P., and Mattioco, F. (1990). Detection of 183 GHz water vapour maser emission from interstellar and circumstellar sources. *aap*, 231:L15–L18.
- Churchwell, E., Babler, B. L., Meade, M. R., Whitney, B. A., Benjamin, R., Indebetouw, R., Cyganowski, C., Robitaille, T. P., Povich, M., Watson, C., and Bracker, S. (2009). The Spitzer/GLIMPSE Surveys: A New View of the Milky Way. *pas*, 121(877):213.
- Claussen, M. J., Wilking, B. A., Benson, P. J., Wootten, A., Myers, P. C., and Terebey, S. (1996). A Monthly Survey of Water Masers Associated with Low-Mass Stars. *apjs*, 106:111.
- Colom, P., Bockelée-Morvan, D., Crovisier, J., and Gérard, E. (2002). Maser emissions from comets. In Migennes, V. and Reid, M. J., editors, *Cosmic Masers: From Proto-Stars to Black Holes*, volume 206, page 443.
- Condon, J. J., Cotton, W. D., Greisen, E. W., Yin, Q. F., Perley, R. A., Taylor, G. B., and Broderick, J. J. (1998). The NRAO VLA Sky Survey. *aj*, 115(5):1693–1716.
- Contreras, Y., Schuller, F., Urquhart, J. S., Csengeri, T., Wyrowski, F., Beuther, H., Bontemps, S., Bronfman, L., Henning, T., Menten, K. M., Schilke, P., Walmsley, C. M., Wienen, M., Tackenberg, J., and Linz, H. (2013). ATLASGAL - compact source catalogue: 330° \leq ℓ \leq 21°. *aap*, 549:A45.
- Cragg, D. M., Johns, K. P., Godfrey, P. D., and Brown, R. D. (1992). Pumping the interstellar methanol masers. *mnr*, 259(1):203–208.

- Cragg, D. M., Sobolev, A. M., and Godfrey, P. D. (2005). Models of class II methanol masers based on improved molecular data. *mnras*, 360(2):533–545.
- Dame, T. M., Ungerechts, H., Cohen, R. S., de Geus, E. J., Grenier, I. A., May, J., Murphy, D. C., Nyman, L. A., and Thaddeus, P. (1987). A Composite CO Survey of the Entire Milky Way. *apj*, 322:706.
- Draine, B. T., Dale, D. A., Bendo, G., Gordon, K. D., Smith, J. D. T., Armus, L., Engelbracht, C. W., Helou, G., Kennicutt, R. C., J., Li, A., Roussel, H., Walter, F., Calzetti, D., Moustakas, J., Murphy, E. J., Rieke, G. H., Bot, C., Hollenbach, D. J., Sheth, K., and Teplitz, H. I. (2007). Dust Masses, PAH Abundances, and Starlight Intensities in the SINGS Galaxy Sample. *apj*, 663(2):866–894.
- Ellingsen, S. P. (2006). Methanol Masers: Reliable Tracers of the Early Stages of High-Mass Star Formation. *apj*, 638(1):241–261.
- Ellingsen, S. P., von Bibra, M. L., McCulloch, P. M., Norris, R. P., Deshpande, A. A., and Phillips, C. J. (1996). A survey of the Galactic plane for 6.7-GHz methanol masers - I. $l=325$ deg- 335 deg $b=-0.^{\circ}53-0.^{\circ}53$. *mnras*, 280(2):378–396.
- Ellingsen, S. P., Voronkov, M. A., Cragg, D. M., Sobolev, A. M., Breen, S. L., and Godfrey, P. D. (2007). Investigating high-mass star formation through maser surveys. In Chapman, J. M. and Baan, W. A., editors, *Astrophysical Masers and their Environments*, volume 242, pages 213–217.
- Elmegreen, B. G. and Lada, C. J. (1977). Sequential formation of subgroups in OB associations. *apj*, 214:725–741.
- Fazio, G. G., Hora, J. L., Allen, L. E., Ashby, M. L. N., Barmby, P., Deutsch, L. K., Huang, J. S., Kleiner, S., Marengo, M., Megeath, S. T., Melnick, G. J., Pahre, M. A., Patten, B. M., Polizotti, J., Smith, H. A., Taylor, R. S., Wang, Z., Willner, S. P., Hoffmann, W. F., Pipher, J. L., Forrest, W. J., McMurty, C. W., McCreight, C. R., McKelvey, M. E., McMurray, R. E., Koch, D. G., Moseley, S. H., Arendt, R. G., Mentzell, J. E., Marx, C. T., Losch, P., Mayman, P., Eichhorn, W., Krebs, D., Jhabvala, M., Gezari, D. Y., Fixsen, D. J., Flores, J., Shakoorzadeh, K., Jungo, R., Hakun, C., Workman, L., Karpati, G., Kichak, R., Whitley, R., Mann,

- S., Tollestrup, E. V., Eisenhardt, P., Stern, D., Gorjian, V., Bhattacharya, B., Carey, S., Nelson, B. O., Glaccum, W. J., Lacy, M., Lowrance, P. J., Laine, S., Reach, W. T., Stauffer, J. A., Surace, J. A., Wilson, G., Wright, E. L., Hoffman, A., Domingo, G., and Cohen, M. (2004). The Infrared Array Camera (IRAC) for the Spitzer Space Telescope. *apjs*, 154(1):10–17.
- Fontani, F., Cesaroni, R., and Furuya, R. S. (2010). Class I and Class II methanol masers in high-mass star-forming regions. *aap*, 517:A56.
- Fujishiro, K., Tokuda, K., Tachihara, K., Takashima, T., Fukui, Y., Zahorecz, S., Saigo, K., Matsumoto, T., Tomida, K., Machida, M. N., ichiro Inutsuka, S., André, P., Kawamura, A., and Onishi, T. (2020). A low-velocity bipolar outflow from a deeply embedded object in taurus revealed by the atacama compact array. *The Astrophysical Journal*, 899(1):L10.
- Gray, M. (1999). Astrophysical masers. *Philosophical Transactions of the Royal Society of London Series A*, 357(1763):3277.
- Green, J. A., Breen, S. L., Fuller, G. A., McClure-Griffiths, N. M., Ellingsen, S. P., Voronkov, M. A., Avison, A., Brooks, K., Burton, M. G., Chrysostomou, A., Cox, J., Diamond, P. J., Gray, M. D., Hoare, M. G., Masheder, M. R. W., Pestalozzi, M., Phillips, C., Quinn, L. J., Richards, A. M. S., Thompson, M. A., Walsh, A. J., Ward-Thompson, D., Wong-McSweeney, D., and Yates, J. A. (2017). The 6-GHz multibeam maser survey - II. Statistical analysis and Galactic distribution of 6668-MHz methanol masers. *mnras*, 469(2):1383–1402.
- Green, J. A., Caswell, J. L., Fuller, G. A., Avison, A., Breen, S. L., Ellingsen, S. P., Gray, M. D., Pestalozzi, M., Quinn, L., Thompson, M. A., and et al. (2010). The 6-ghz methanol multibeam maser catalogue - ii. galactic longitudes 6° to 20°. *Monthly Notices of the Royal Astronomical Society*, 409(3):913–935.
- Green, J. A., Caswell, J. L., Fuller, G. A., Avison, A., Breen, S. L., Ellingsen, S. P., Gray, M. D., Pestalozzi, M., Quinn, L., Thompson, M. A., and et al. (2012). The 6-ghz methanol multibeam maser catalogue - iv. galactic longitudes 186°-330°

including the orion-monoceros region. *Monthly Notices of the Royal Astronomical Society*, 420(4):3108–3125.

Griffin, M. J., Abergel, A., Abreu, A., Ade, P. A. R., André, P., Augueres, J. L., Babbedge, T., Bae, Y., Baillie, T., Baluteau, J. P., Barlow, M. J., Bendo, G., Benielli, D., Bock, J. J., Bonhomme, P., Brisbin, D., Brockley-Blatt, C., Caldwell, M., Cara, C., Castro-Rodriguez, N., Cerulli, R., Chanical, P., Chen, S., Clark, E., Clements, D. L., Clerc, L., Coker, J., Communal, D., Conversi, L., Cox, P., Crumb, D., Cunningham, C., Daly, F., Davis, G. R., de Antoni, P., Delderfield, J., Devin, N., di Giorgio, A., Didschuns, I., Dohlen, K., Donati, M., Dowell, A., Dowell, C. D., Duband, L., Dumaye, L., Emery, R. J., Ferlet, M., Ferrand, D., Fontignie, J., Fox, M., Franceschini, A., Frerking, M., Fulton, T., Garcia, J., Gastaud, R., Gear, W. K., Glenn, J., Goizel, A., Griffin, D. K., Grundy, T., Guest, S., Guillemet, L., Hargrave, P. C., Harwit, M., Hastings, P., Hatziminaoglou, E., Herman, M., Hinde, B., Hristov, V., Huang, M., Imhof, P., Isaak, K. J., Israelsson, U., Ivison, R. J., Jennings, D., Kiernan, B., King, K. J., Lange, A. E., Latter, W., Laurent, G., Laurent, P., Leeks, S. J., Lellouch, E., Levenson, L., Li, B., Li, J., Lilienthal, J., Lim, T., Liu, S. J., Lu, N., Madden, S., Mainetti, G., Marliani, P., McKay, D., Mercier, K., Molinari, S., Morris, H., Moseley, H., Mulder, J., Mur, M., Naylor, D. A., Nguyen, H., O'Halloran, B., Oliver, S., Olofsson, G., Olofsson, H. G., Orfei, R., Page, M. J., Pain, I., Panuzzo, P., Papageorgiou, A., Parks, G., Parr-Burman, P., Pearce, A., Pearson, C., Pérez-Fournon, I., Pinsard, F., Pisano, G., Podosek, J., Pohlen, M., Polehampton, E. T., Poulliquen, D., Rigopoulou, D., Rizzo, D., Roseboom, I. G., Roussel, H., Rowan-Robinson, M., Rownd, B., Saraceno, P., Sauvage, M., Savage, R., Savini, G., Sawyer, E., Scharmberg, C., Schmitt, D., Schneider, N., Schulz, B., Schwartz, A., Shafer, R., Shupe, D. L., Sibthorpe, B., Sidher, S., Smith, A., Smith, A. J., Smith, D., Spencer, L., Stobie, B., Sudiwala, R., Sukhatme, K., Surace, C., Stevens, J. A., Swinyard, B. M., Trichas, M., Tourette, T., Triou, H., Tseng, S., Tucker, C., Turner, A., Vaccari, M., Valtchanov, I., Vigroux, L., Virique, E., Voellmer, G., Walker, H., Ward, R., Waskett, T., Weilert, M., Wesson, R., White, G. J., Whitehouse, N., Wilson, C. D., Winter, B., Woodcraft, A. L., Wright, G. S., Xu, C. K., Zavagno, A.,

- Zemcov, M., Zhang, L., and Zonca, E. (2010). The Herschel-SPIRE instrument and its in-flight performance. *aap*, 518:L3.
- Hennebelle, P. and Falgarone, E. (2012). Turbulent molecular clouds. *aapr*, 20:55.
- Herrnstein, J. R., Moran, J. M., Greenhill, L. J., Diamond, P. J., Inoue, M., Nakai, N., Miyoshi, M., Henkel, C., and Riess, A. (1999). A geometric distance to the galaxy NGC4258 from orbital motions in a nuclear gas disk. *nat*, 400(6744):539–541.
- Heyer, M. H. and Terebey, S. (1998). The Anatomy of the Perseus Spiral Arm: ^{12}CO and IRAS Imaging Observations of the W3-W4-W5 Cloud Complex. *apj*, 502(1):265–277.
- Hocuk, S. and Spaans, M. (2010). The thermodynamics of molecular cloud fragmentation - star formation under non-milky way conditions. *A&A*, 510:A110.
- Hoffman, I. M., Goss, W. M., and Palmer, P. (2007). The formaldehyde masers in sgr b2: Very long baseline array and very large array observations. *The Astrophysical Journal*, 654(2):971–977.
- Hollenbach, D. J. and Tielens, A. G. G. M. (1999). Photodissociation regions in the interstellar medium of galaxies. *Reviews of Modern Physics*, 71(1):173–230.
- Joy, A. H. (1945). T Tauri Variable Stars. *apj*, 102:168.
- Kennicutt, R. C. (2005). The role of massive stars in astrophysics. In Cesaroni, R., Felli, M., Churchwell, E., and Walmsley, M., editors, *Massive Star Birth: A Crossroads of Astrophysics*, volume 227, pages 3–11.
- Lada, C. J. (1987). Star formation: from OB associations to protostars. In Peimbert, M. and Jugaku, J., editors, *Star Forming Regions*, volume 115, page 1.
- Lada, C. J. and Lada, E. A. (2003). Embedded Clusters in Molecular Clouds. *araa*, 41:57–115.
- Lumsden, S. L., Hoare, M. G., Urquhart, J. S., Oudmaijer, R. D., Davies, B., Mottram, J. C., Cooper, H. D. B., and Moore, T. J. T. (2013). The Red MSX

- Source Survey: The Massive Young Stellar Population of Our Galaxy. *apjs*, 208(1):11.
- McKee, C. F. and Ostriker, E. C. (2007). Theory of Star Formation. *araa*, 45(1):565–687.
- Meaburn, J., López, J. A., Boumis, P., Lloyd, M., and Redman, M. P. (2009). A high-speed bipolar outflow from the archetypical pulsating star mira a. *Astronomy & Astrophysics*, 500(2):827–831.
- Menten, K. M. (1997). Masers as chemical probes of star-forming regions. *IAU Symposium*, 178:163–172.
- Menten, K. M. and Melnick, G. J. (1991). 321 GHz Submillimeter Water Masers around Evolved Stars. *apj*, 377:647.
- Menten, K. M., Melnick, G. J., Phillips, T. G., and Neufeld, D. A. (1990). A New Submillimeter Water Maser Transition at 325 GHz. *apjl*, 363:L27.
- Menten, K. M., Lundgren, A., Belloche, A., Thorwirth, S., and Reid, M. J. (2008). A multi-transition submillimeter water maser study of evolved stars. detection of a new line near 475 ghz. *A&A*, 477(1):185–192.
- Mestel, L. and Spitzer, L., J. (1956). Star formation in magnetic dust clouds. *MNRAS*, 116:503.
- Molinari, S., Pezzuto, S., Cesaroni, R., Brand, J., Faustini, F., and Testi, L. (2008). The evolution of the spectral energy distribution in massive young stellar objects. *aap*, 481(2):345–365.
- Molinari, S., Schisano, E., Elia, D., Pestalozzi, M., Traficante, A., Pezzuto, S., Swinyard, B. M., Noriega-Crespo, A., Bally, J., Moore, T. J. T., Plume, R., Zavagno, A., di Giorgio A. M., Liu, S. J., Pilbratt, G. L., Mottram, J. C., Russeil, D., Piazza, L., Veneziani, M., Benedettini, M., Calzoletti, L., Faustini, F., Natoli, P., Piacentini, F., Merello, M., Palmese, A., Del Grande, R., Polychroni, D., Rygl, K. L. J., Polenta, G., Barlow, M. J., Bernard, J. P., Martin, P. G., Testi, L., Ali, B., Andre, P., Beltran, M. T., Billot, N., Carey, S., Cesaroni, R., Compiegne,

- M., Eden, D., Fukui, Y., Garcia-Lario, P., Hoare, M. G., Huang, M., Joncas, G., Lim, T. L., Lord, S. D., Martinavarro-Armengol, S., Motte, F., Paladini, R., Paradis, D., Peretto, N., Robitaille, T., Schilke, P., Schneider, N., Schulz, B., Sibthorpe, B., Strafella, F., Thompson, M. A., Umana, G., Ward-Thompson, D., and Wyrowski, F. (2016). VizieR Online Data Catalog: Hi-GAL. inner Milky Way: $+68 \geq l \geq 70$ (Molinari+, 2016). *VizieR Online Data Catalog*, pages J/A+A/591/A149.
- Moore, T. J. T., Plume, R., Thompson, M. A., Parsons, H., Urquhart, J. S., Eden, D. J., Dempsey, J. T., Morgan, L. K., Thomas, H. S., Buckle, J., Brunt, C. M., Butner, H., Carretero, D., Chrysostomou, A., deVilliers, H. M., Fich, M., Hoare, M. G., Manser, G., Mottram, J. C., Natario, C., Olguin, F., Peretto, N., Polychroni, D., Redman, R. O., Rigby, A. J., Salji, C., Summers, L. J., Berry, D., Currie, M. J., Jenness, T., Pestalozzi, M., Traficante, A., Bastien, P., diFrancesco, J., Davis, C. J., Evans, A., Friberg, P., Fuller, G. A., Gibb, A. G., Gibson, S., Hill, T., Johnstone, D., Joncas, G., Longmore, S. N., Lumsden, S. L., Martin, P. G., Nguyen Lu'o'ng, Q., Pineda, J. E., Purcell, C., Richer, J. S., Schieven, G. H., Shipman, R., Spaans, M., Taylor, A. R., Viti, S., Weferling, B., White, G. J., and Zhu, M. (2015). The JCMT Plane Survey: early results from the $\ell = 30^\circ$ field. *MNRAS*, 453(4):4264–4277.
- Motte, F., Bontemps, S., Schilke, P., Schneider, N., Menten, K. M., and Brogière, D. (2007). The earliest phases of high-mass star formation: a 3 square degree millimeter continuum mapping of Cygnus X. *aap*, 476(3):1243–1260.
- Olmi, L., Araya, E. D., Hofner, P., Molinari, S., Morales Ortiz, J., Moscadelli, L., and Pestalozzi, M. (2014). Discovery of weak 6.7 GHz CH₃OH masers in a sample of high-mass Hi-GAL sources. *aap*, 566:A18.
- Omukai, K. and Nishi, R. (1998). Formation of Primordial Protostars. *apj*, 508(1):141–150.
- Ostriker, E. C. and Kim, W. T. (2004). Origins of Giant Molecular Clouds. In Clemens, D., Shah, R., and Brainerd, T., editors, *Milky Way Surveys: The Struc-*

ture and Evolution of our Galaxy, volume 317 of *Astronomical Society of the Pacific Conference Series*, page 248.

Pandian, J. D., Goldsmith, P. F., and Deshpande, A. A. (2007). The Arcibo Methanol Maser Galactic Plane Survey. In Chapman, J. M. and Baan, W. A., editors, *Astrophysical Masers and their Environments*, volume 242, pages 208–212.

Pilbratt, G. L., Riedinger, J. R., Passvogel, T., Crone, G., Doyle, D., Gageur, U., Heras, A. M., Jewell, C., Metcalfe, L., Ott, S., and et al. (2010). Herschel space observatory. *Astronomy and Astrophysics*, 518:L1.

Poglitsch, A., Waelkens, C., Bauer, O. H., Cepa, J., Feuchtgruber, H., Henning, T., van Hoof, C., Kerschbaum, F., Krause, O., Renotte, E., Rodriguez, L., Saraceno, P., and Vandenbussche, B. (2008). The Photodetector Array Camera and Spectrometer (PACS) for the Herschel Space Observatory. In Oschmann, Jacobus M., J., de Graauw, M. W. M., and MacEwen, H. A., editors, *Space Telescopes and Instrumentation 2008: Optical, Infrared, and Millimeter*, volume 7010 of *Society of Photo-Optical Instrumentation Engineers (SPIE) Conference Series*, page 701005.

Schuller, F., Menten, K. M., Contreras, Y., Wyrowski, F., Schilke, P., Bronfman, L., Henning, T., Walmsley, C. M., Beuther, H., Bontemps, S., Cesaroni, R., Deharveng, L., Garay, G., Herpin, F., Lefloch, B., Linz, H., Mardones, D., Minier, V., Molinari, S., Motte, F., Nyman, L. Å., Reveret, V., Risacher, C., Russeil, D., Schneider, N., Testi, L., Troost, T., Vasyunina, T., Wienen, M., Zavagno, A., Kovacs, A., Kreysa, E., Siringo, G., and Weiß, A. (2009). ATLASGAL - The APEX telescope large area survey of the galaxy at 870 μm . *aap*, 504(2):415–427.

Sobolev, A. M., Cragg, D. M., Ellingsen, S. P., Gaylard, M. J., Goedhart, S., Henkel, C., Kirsanova, M. S., Ostrovskii, A. B., Pankratova, N. V., Shelemei, O. V., van der Walt, D. J., Vasyunina, T. S., and Voronkov, M. A. (2007). How do methanol masers manage to appear in the youngest star vicinities and isolated molecular clumps? In Chapman, J. M. and Baan, W. A., editors, *Astrophysical Masers and*

their Environments, volume 242, pages 81–88.

- Solomon, P. M., Sanders, D. B., and Rivolo, A. R. (1985). The Massachusetts Stony Brook galactic plane CO survey - Disk and spiral arm molecular cloud populations. *apjl*, 292:L19–L24.
- Stark, A. A. (1984). Kinematics of molecular clouds.I. Velocity dispersion in the solar neighborhood.. *apj*, 281:624–633.
- Szymczak, M., Kus, A. J., Hrynek, G., Kępa, A., and Pazderski, E. (2002). 6.7 GHz methanol masers at sites of star formation. A blind survey of the Galactic plane between $20^\circ \leq l \leq 40^\circ$ and $b \leq 0.52$. *aap*, 392:277–286.
- Tan, J. C., Beltrán, M. T., Caselli, P., Fontani, F., Fuente, A., Krumholz, M. R., McKee, C. F., and Stolte, A. (2014). Massive star formation. *Protostars and Planets VI*.
- Tarter, T. C. and Welch, W. J. (1986). A Cloud Collision Model for Water Maser Excitation. *apj*, 305:467.
- Thompson, M. A., Hatchell, J., Walsh, A. J., MacDonald, G. H., and Millar, T. J. (2006). A SCUBA imaging survey of ultracompact HII regions. The environments of massive star formation. *aap*, 453(3):1003–1026.
- Titmarsh, A. M., Ellingsen, S. P., Breen, S. L., Caswell, J. L., and Voronkov, M. A. (2014). A search for water masers associated with class II methanol masers - I. Longitude range 6° - 20° . *MNRAS*, 443(4):2923–2939.
- Urquhart, J. S., Csengeri, T., Wyrowski, F., Schuller, F., Bontemps, S., Bronfman, L., Menten, K. M., Walmsley, C. M., Contreras, Y., Beuther, H., Wienen, M., and Linz, H. (2014a). ATLASGAL - Complete compact source catalogue: $280^\circ \leq l \leq 60^\circ$. *aap*, 568:A41.
- Urquhart, J. S., König, C., Giannetti, A., Leurini, S., Moore, T. J. T., Eden, D. J., Pillai, T., Thompson, M. A., Braiding, C., Burton, M. G., Csengeri, T., Dempsey, J. T., Figura, C., Froebrich, D., Menten, K. M., Schuller, F., Smith, M. D., and

- Wyrowski, F. (2018). ATLASGAL - properties of a complete sample of Galactic clumps. *mnras*, 473(1):1059–1102.
- Urquhart, J. S., Moore, T. J. T., Csengeri, T., Wyrowski, F., Schuller, F., Hoare, M. G., Lumsden, S. L., Mottram, J. C., Thompson, M. A., Menten, K. M., Walmsley, C. M., Bronfman, L., Pfalzner, S., König, C., and Wienen, M. (2014b). ATLASGAL - towards a complete sample of massive star forming clumps. *mnras*, 443(2):1555–1586.
- Urquhart, J. S., Wells, M. R. A., Pillai, T., Leurini, S., Giannetti, A., Moore, T. J. T., Thompson, M. A., Figura, C., Colombo, D., Yang, A. Y., König, C., Wyrowski, F., Menten, K. M., Rigby, A. J., Eden, D. J., and Ragan, S. E. (2022). ATLASGAL - evolutionary trends in high-mass star formation. *mnras*, 510(3):3389–3407.
- Walsh, A. J., Breen, S. L., Britton, T., Brooks, K. J., Burton, M. G., Cunningham, M. R., Green, J. A., Harvey-Smith, L., Hindson, L., Hoare, M. G., Indermuehle, B., Jones, P. A., Lo, N., Longmore, S. N., Lowe, V., Phillips, C. J., Purcell, C. R., Thompson, M. A., Urquhart, J. S., Voronkov, M. A., White, G. L., and Whiting, M. (2011). HOPS: The H₂O Southern Galactic Plane Survey. In Röllig, M., Simon, R., Ossenkopf, V., and Stutzki, J., editors, *EAS Publications Series*, volume 52 of *EAS Publications Series*, pages 135–138.
- Walsh, A. J., Purcell, C. R., Longmore, S. N., Breen, S. L., Green, J. A., Harvey-Smith, L., Jordan, C. H., and Macpherson, C. (2014). Accurate water maser positions from HOPS. *mnras*, 442(3):2240–2252.
- Wardle, M. and McDonnell, K. (2012). Oh masers and supernova remnants. *Proceedings of the International Astronomical Union*, 8(S287):441–448.
- Weaver, H., Williams, D. R. W., Dieter, N. H., and Lum, W. T. (1965). Observations of a Strong Unidentified Microwave Line and of Emission from the OH Molecule. *nat*, 208(5005):29–31.
- Werner, M. W., Roellig, T. L., Low, F. J., Rieke, G. H., Rieke, M., Hoffmann, W. F., Young, E., Houck, J. R., Brandl, B., Fazio, G. G., and et al. (2004). The

- spitzer space telescope mission. *The Astrophysical Journal Supplement Series*, 154(1):1–9.
- Williams, J. P. and McKee, C. F. (1997). The Galactic Distribution of OB Associations in Molecular Clouds. *apj*, 476(1):166–183.
- Woodall, J. M. and Gray, M. D. (2007). A search for 22-GHz H₂O masers in supernova remnants. *mnras*, 378(1):L20–L23.
- Wright, E. L., Eisenhardt, P. R. M., Mainzer, A. K., Ressler, M. E., Cutri, R. M., Jarrett, T., Kirkpatrick, J. D., Padgett, D., McMillan, R. S., Skrutskie, M., and et al. (2010). The wide-field infrared survey explorer (wise): Mission description and initial on-orbit performance. *The Astronomical Journal*, 140(6):1868–1881.
- Zinnecker, H. and Yorke, H. W. (2007). Toward Understanding Massive Star Formation. *araa*, 45(1):481–563.
- Zuckerman, B. (1973). A Model of the Orion Nebula. *apj*, 183:863–870.